LONG TERM OPTICAL AND X-RAY MONITORING OF BLACK HOLE CANDIDATES IN EXTRAGALACTIC GLOBULAR CLUSTERS

By

Kristen C. Dage

A DISSERTATION

Submitted to
Michigan State University
in partial fulfillment of the requirements
for the degree of

Astrophysics and Astronomy—Doctor of Philosophy

2020

ABSTRACT

LONG TERM OPTICAL AND X-RAY MONITORING OF BLACK HOLE CANDIDATES IN EXTRAGALACTIC GLOBULAR CLUSTERS

By

Kristen C. Dage

The question of whether globular clusters (GCs) host black holes (BHs) has been a long-standing question in astronomy. Because of the dynamics of the crowded globular cluster environment, they should be extremely efficient at forming black hole-black hole binaries (BBHs), such as those detected merging by LIGO. LIGO is detecting many more (and more massive!) BBHs than was ever expected, and a first step to understanding the formation of these binaries is to understand BHs in GCs. However, very few ways exist to study BHs in GCs observationally, and there is only one effective method to study BH candidates in extragalactic GCs: by studying ultraluminous X-ray sources (ULXs) that are associated with GCs. Because their X-ray luminosities far exceed the Eddington limit for a stellar mass BH, ULXs in GCs are good BH candidates. However, they are very rare, with only a few per galaxy (with only 10 currently known sources among 3 galaxies).

In this thesis, we study a total of 9 ULX sources that are associated with globular clusters in both X-ray and optical. One of these, RZ2109, shows extreme variability across more than 15 years of monitoring in X-ray, with changes of almost an order of magnitude on the order of days. Typically any variability in flux is expected to be correlated with a change in the spectral properties of the source (i.e. some physical change in the system), however, the shape of the X-ray spectrum of RZ2109 remains the same across all observations. X-ray and optical studies of all 9 GC ULXs indicate a potential correlation between the X-ray spectrum and presence of optical emission beyond the cluster continuum–one of the few X-ray-optical correlations known for astronomical objects. Lastly, we present long-term monitoring in optical of RZ2109 shows a broad [OIII] emission line which declines long-term over almost ten years, and then re-brightens.

"Life is a space voyage, and not a short one, either, but one that'll last for billions of years." (Kurt Vonnegut)

In loving memory of John Howkins and Gary Dage

ACKNOWLEDGMENTS

I want to thank my advisor, Steve Zepf, who is the bee's knees, and my wonderful collaborators: Arash Bahramian, Arunav Kundu, Mark Peacock, and Tom Maccarone. Thank you for sharing this journey with me, and for being wonderful researchers and friends. I've enjoyed all of our discussions and the different perspectives you bring.

I want to thank the people who inspired me to become a better scientist and researcher, especially (Dr.!) Lara Backer, for being an inspiration, to my grandfather John Howkins for always asking really annoying questions and making me want to ask questions too, to my dad, Gary, for being the embodiment of an innovator, inventor, and engineer and encouraging my curiosity in the world. To my mom, Enid, for making math fun (even though we swore up and down we didn't really like it that much).

I want to thank the people who taught me: especially Dave Stoddard and Art Wiggins for being the first people to introduce me to the joy of physics. Thanks to Frances Smith, Ruth Favro, Mike LaChance, Jacqueline Vansant, Thaddeus Radzilowski, Dorothy McLear, and Rick Simek, as well as Jim Hetrick, Nick Licata, Don Bord, Jeff Prentis, Ed Brown and Leslie Reynolds. And special thanks to Will Clarkson for giving me my first chance to do astronomy, and to Jay Strader and Laura Chomiuk for welcoming me into their herd.

Lastly, I want to thank everyone who has been there for me, Rufus, Nadia Khalyleh, Jamilah Alhashidi, Kit, Gerald, Beth and Lara Backer, Dylan Heberle, Joshua Torres, Amal, Yasmeen and Amna Khalyleh, and all the new friends I've made along the way: Sara Ayoub, Jessica Maldonado, Philipp Grete & Petja Ivanova, Laura Shishkovsky, Teresa Panurach, Megan Davis, Shannon Schmoll, Chelsea Harris, Huei Sears, Chris Britt, Benoit Cote, Ryan Urquhart, Erica Thygesen, Carl Fields, Brandon Barker, and especially Kim Crosslan.

TABLE OF CONTENTS

LIST OF TABLES

LIST OF FIGURES

KEY TO ABBREVIATIONS

- BBH - Black Hole Black Hole Binary
- BH - Black Hole
- GC - Globular Cluster
- IMBH - Intermediate Mass Black Hole
- LIGO - Laser Interferometer Gravitational-Wave Observatory
- LMXB - Low Mass X-Ray Binary
- NS - Neutron Star
- TDE - Tidal Disruption Event
- UCXB - Ultracompact X-ray Binary
- ULX - Ultraluminous X-Ray Source

Chapter 1

Introduction

One of the long-standing questions in astronomy is "Do globular clusters host black holes?" This question has been under debate since 1969 (Spitzer, 1969). As some of the densest and oldest places in the universe, globular clusters (GCs) can probe unique condition for black hole (BH) formation and the creation of exotic binaries. Currently, the only method to probe the number of black holes in extragalactic globular clusters (see Section 1.3.1 for more detail) is by searching for ultraluminous X-ray sources (ULXs) which are coincident with the globular clusters of other galaxies.

Ultraluminous X-ray sources are an exotic class of objects which are much brighter in the X-ray than what is physically expected for a stellar mass compact object, as they typically exceed the Eddington limit, which predicts luminosity limits based on the object's mass (See Section 1.2.1 for more detail). The observed luminosities are produced by accretion onto a compact object, although the exact physical processes behind the high luminosities are still not well understood.

Younger populations of ULXs have been well studied in the star-forming regions of spiral galaxies, which may be due to accretion onto highly magnetized neutron stars (NSs) or BHs. However, ULXs also exist in older populations: globular clusters associated with elliptical galaxies. Studying this class of ULXs in GCs has implications both for properties of ULXs as a whole, as well as for understanding the question regarding the number of black holes in globular clusters. Because these sources are so rare, understanding their accretion processes and signatures can provide clues to their formation histories, which in turn may one day explain why these sources are so rare. Therefore, a brief overview of accretion processes in X-ray binaries is required before delving deeper into the subject.

1.1 Overview of Accretion Processes in X-Ray Binaries

X-ray binaries are a class of binary systems which emit X-ray radiation. The binary contains two objects: a compact object (i.e. a neutron star or black hole), which feeds off of the companion star (the "donor") and accretes material off the star. The angular momentum in the accreted plasma is conserved and thus forms an accretion disk around the compact object[1].

Figure 1.1 shows a classic representation of such a system. If the donor star gets close enough to the compact object, it will fill its Roche lobe[2] and become pear shaped, with the material exiting through the L_1 Lagrangian point and forming the accretion disk around the compact object.

Viscous stress that is thought to originate in magentorotational instability (Balbus & Hawley, 1998) causes matter to lose angular momentum and fall in towards the surface of the compact object. This releases gravitational potential energy, $(\frac{GM\dot{M}}{R})$ [3]. The compact object implies that the radius will be very small, which implies the disk temperature is high, thereby producing X-rays. Because the compact object is so massive, the emission is highly energetic and luminous.

---

[1] Some high-mass X-ray binaries do not always have accretion disks, they can be fed solely by winds emanating from a massive donor star, which do not produce a stable accretion disk.

[2] Roche lobe: a teardrop shaped region that represents the smallest equipotential surface that can exist around a binary system. See `http://astronomy.swin.edu.au/cosmos/R/Roche-lobe` for more.

[3] Where G is the gravitational constant, R is the distance between the two objects, M is the mass of the accretor, and $\dot{M}$ is the mass transfer rate.

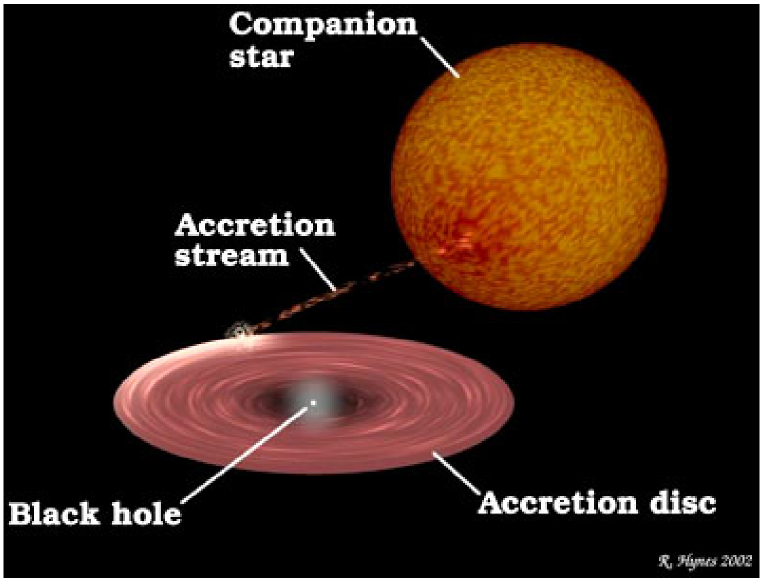

Figure 1.1: Artist's representation of an X-ray binary. Because the compact object (in this case a black hole) is so much more massive than the companion star, it accretes material from the star, which forms an accretion disk around the central object. Image from Rob Hynes.

The observed X-ray emission from X-ray binaries can have several separate sources within the accretion disk. The accretion disk itself emits in X-rays at lower photon energies (Shakura & Sunyaev, 1973; Hanawa, 1989). This emission is thermal, multi-color blackbody emission (i.e. blackbody models with multiple temperatures superimposed) and influenced by the geometry of the disk. Non-thermal X-ray emission can also be observed in higher X-ray energies, and is produced by inverse Comptonization (Titarchuk, 1994).

X-ray reprocessing can also occur in the accretion disk. The emitted X-rays can interact with clumpy material in the disk, or hit the outer edges (which for some geometries will puff up with respect to the inner disk). The X-rays will be absorbed, and then re-emitted at a lower energy (UV or optical).

1.2 Ultraluminous X-Ray Sources

ULXs are defined as non-nuclear point sources (i.e. not the active galactic nucleus in the given galaxy) which have X-ray luminosities exceeding the Eddington limit for a 10 $M_\odot$ black hole, with values of 10^{39} erg/s or above. Because most X-ray binaries do not typically reach these high luminosities, ULX sources are likely to be indicators of either higher mass black holes, or a lower mass compact object (either neutron star or lower mass black hole) accreting in a non-standard physical regime.

1.2.1 The Eddington Limit

The Eddington Limit was derived by Sir Arthur Eddington as a way to determine the maximum luminosity produced by a radiating body under certain conditions[4]. This maximum luminosity occurs when the gravitational force is equal to the radiation pressure:

$$P_{\text{rad}} < F_{\text{grav}}. \tag{1.1}$$

We have implicitly assumed that the radiation is spherically symmetric, and that the central mass is exerting force on a gas comprised of free protons and electrons. The radiation pressure is Φ_E/c, where Φ_E is the energy flux transferred to a free electron: $\frac{\sigma_T L}{4\pi R^2}$. Here, L is the source luminosity, R is the radius, and σ_T represents the cross-section for Thomson scattering. Thus, we find:

$$\frac{\sigma_T L}{4c\pi R^2} \leq \frac{GMm_p}{R^2}. \tag{1.2}$$

---

[4] See `http://www-ppl.s.chiba-u.jp/lecture/radiation/node2.html` for more details on the derivation.

Upon simplifying the equation and evaluating the constants, we find the Eddington limit:

$$L_{\text{Edd}} = 1.2 \times 10^{38} \frac{M}{M_\odot} \text{erg/s}. \tag{1.3}$$

Since the Eddington limit depends on the mass of the central object, a luminosity of 10^{39} erg/s must be generated in a very physically different way depending on the mass of the accretor. For a neutron star, which are typically less massive than 2 $M_\odot$, this luminosity is well above its Eddington limit. In this case, either the source is accreting in a physically different regime than other NS XRBs, or the geometry of the system does not fit the assumptions used to derive the Eddington limit (see Section 1.2.3).

For black holes around $10M_\odot$, luminosities on this order of magnitudes are around or only slightly above their Eddington limits. By contrast, intermediate mass black holes (a few hundred to thousands of stellar masses, i.e. smaller than the super massive BHs that reside at the center of galaxies but larger than anything produced by the deaths of single stars) would be accreting in the sub-Eddington regime, while producing luminosities near or above 10^{39} erg/s because of their very high mass. By studying the observational signatures of ULXs, we can begin to disentangle the nature of the compact object.

1.2.2 The Ultraluminous State

For X-ray binaries accreting at normal rates (i.e. sub-Eddington), they are typically classified into two states, the so-called high/soft state, or the low/hard state. The first state happens when the thermal component (disk) dominates; the source is brighter, but has many more lower (softer) photons. In the low/hard state, the X-ray spectrum is mainly a steep power-law component, while the luminosity is relatively lower with a smaller contribution from the disk. For quiescent black holes, and ones in the low/hard state, the power output is dominated by the associated radio jet (Gallo et al., 2003).

However, work by Gladstone et al. 2009 showed that ULXs belonged to an entirely different accretion regime. Gladstone systematically fit a number of the highest quality spectra of ULXs in star-forming regions, and found that the spectra could be well modeled by a disk plus a Comptonized corona. One physical interpretation of this, assuming the accretor is a lower mass BH or NS is that a super-Eddington accretion flow is present along with the accretion disk.

Follow-up work by Sutton et al. 2013 determined that ULXs fell into three classes: soft ultraluminous and hard ultraluminous regimes, and a broadened disk model. These classes are based on which model the sources are best fit by, i.e. a disk model, a power-law model, or a combination of both. The subsequent discovery of pulsating ULXs by Bachetti et al. 2013 makes the physical interpretation of these classes of models difficult, as the compact object could have a wide range of masses, and the spectral shape does not differentiate a neutron star from an intermediate mass black hole.

1.2.3 Neutron Star ULXs

Given their low mass, neutron stars were thought to be unlikely accretors in ULX binaries. However, all of that changed when pulsations were detected in the ULX source M82 X-2 (Bachetti et al., 2014). Because coherent pulsations require a surface, a black hole accretor is out of the question, as they are by nature without any type of surface and unable to produce pulsations. Since then, pulsations have been observed in other systems: NGC 5907 ULX, NGC 7793 P13, NGC 300 ULX-1 (Greene et al., 2019, and references therein). Another NS ULX has been identified via a cyclotron resonance feature (Brightman et al., 2018).

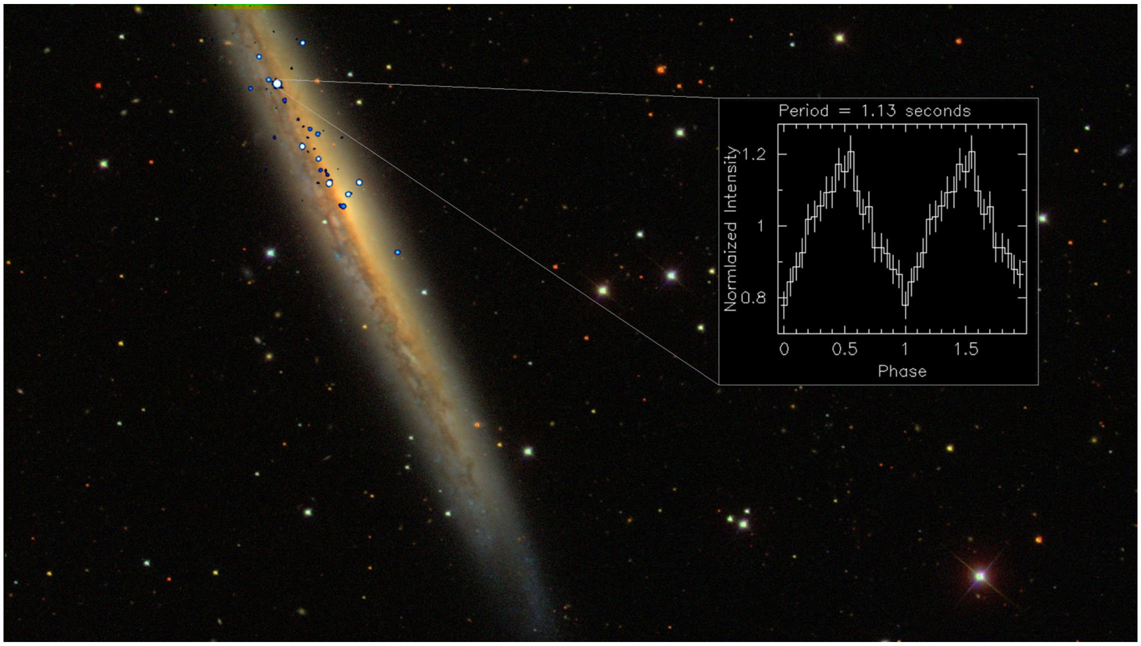

Figure 1.2: Credit: Optical image of M82, with the X-ray point sources overlaid on the galaxy, and a cut out of the observed X-ray pulses connected to M82-X2. ESA/XMM-Newton; NASA/Chandra and SDSS

The physical mechanisms to explain why the lower mass neutron star accretors can reach luminosities on the order of 10^{40} erg/s are currently under debate. Geometric beaming is one possibility (King et al., 2017), but is not a satisfactory explanation for the high luminosity origins of all ULX sources; for example, sources with nebular optical emission lines have a relatively low inferred beaming factor (Binder et al., 2018). However, the presence of a high magnetic field could also provide another source of pressure to draw extra material off the donor star and overcome radiation pressure (Brightman et al., 2018).

In either case, it is worth noting that all of the detected NS ULXs, and indeed the well studied population of ULXs, are found in star forming regions of spiral galaxies and seem to have massive and hydrogen rich companions. NS ULXs, then, not only seem to be associated with a high magnetic field to drive their high accretion rates, but also a massive donor star. Both of these phenomena go hand-in-hand with a young environment, as massive donor stars have short lifespans, and high magnetic fields decay over timescales of millions of years. This motivates the question as to whether these ULXs in star-forming regions of galaxies are powered by the same physical mechanisms as the ULXs with lower mass, metal poor donors which reside in globular clusters associated in elliptical galaxies.

1.3 Globular Clusters

Globular clusters are made up of ten thousands to millions of stars packed in a dense environment of tens to hundreds of parsecs across (e.g. Fig 1.3). Because of this, the environment is very dynamic−the cross section for interaction is high and binaries can form easily; in fact, X-ray binaries tend to be over-represented in globular clusters (Clark, 1975; Pooley et al., 2003). Clusters represent an older population of stars, and can produce many black holes as byproducts of the deaths of the initially present shorter-lived stars. This makes globular clusters an attractive environment for forming binaries of a black hole with a second black hole (BBHs). In fact, the more massive objects in a binary will preferentially exchange their companion for a more massive object, leading to the formation of up to two generations of BBHs, where one of the black holes from the first BBH is swapped out for a second black hole passing by (Rodriguez et al., 2019). The formation of BBHs is currently of significant interest, as a total of ten BBHs have now been observed by LIGO [5], and these mergers are more common than was expected (Abadie et al., 2010). However, we must first consider the nature of black holes in globular clusters.

---

[5] `https://www.ligo.caltech.edu/page/four-new-detections-o1-o2-catalog`

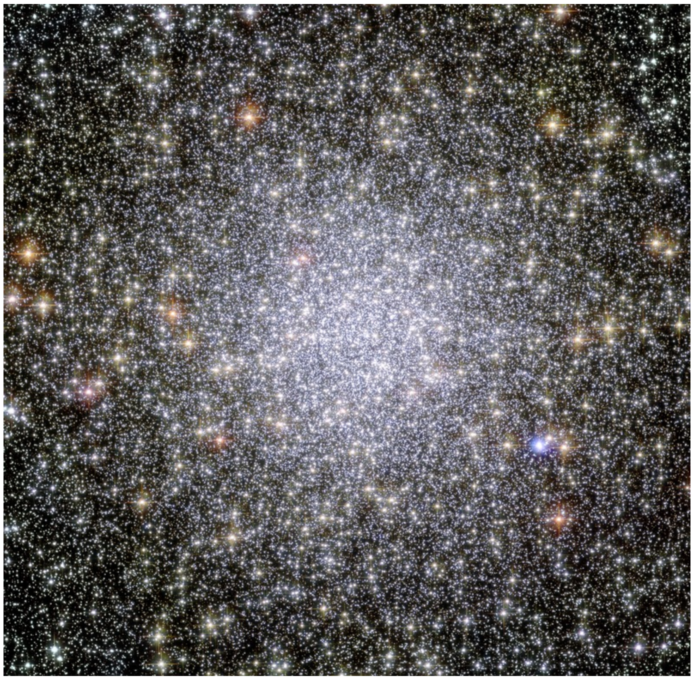

Figure 1.3: Optical image of globular cluster 47 Tucanae. Image credit: NASA, ESA, and the Hubble Heritage (STScI/AURA)-ESA/Hubble Collaboration Acknowledgment: J. Mack (STScI) and G. Piotto (University of Padova, Italy).

1.3.1 Black Holes in Globular Clusters?

The exact number of black holes in globular clusters is currently an open question, and it has been under debate for quite some time if globular cluster should even retain black holes. The more massive objects in the clusters are expected to fall towards the cluster center, and then be ejected by the dynamical influences of the other binaries (Spitzer, 1969; Kulkarni et al., 1993). More recent numerical and observational work has shown that this may not be the case (Morscher et al., 2013; Shishkovsky et al., 2018; Giesers et al., 2018, 2019). Actually, black holes may possibly drive the cluster formation and evolution, and the nature and number of black holes certainly should influence the cluster structure (Giersz et al., 2019). Observational studies of BHs in GCs has a large impact both on understanding cluster evolution, as well as giving clues to the conditions that BBHs form in.

Observing black holes is difficult, and it is even more difficult to search for them in globular clusters. Globular cluster black hole candidates in our own Galaxy are few and far between, with only a handful of candidates (Strader et al., 2012a; Chomiuk et al., 2013; Bahramian et al., 2017; Shishkovsky et al., 2018), and two confirmed (Giesers et al., 2018, 2019). There are two methods to search for black holes in galactic globular clusters. The first method studies black holes in quiescence, as there is a correlation between radio luminosity from the jet, and X-ray luminosity (Plotkin et al., 2012), which can allow BHs to be separated from other X-ray emitting binaries such as NSs. The second method relies on having an extensive spectroscopic survey of the clusters, and using the radial velocities to dynamically measure the black hole mass (Giesers et al., 2018). Both of these techniques will only work with Galactic globular clusters, as they require the clusters to be resolved, and the ability to detect X-ray faint sources. However, the Milky Way is home to less than 200 globular clusters, whereas the number of known globular clusters outside our own Galaxy is over hundreds of thousands. The best way to probe the much larger extragalactic population of globular clusters for black hole candidates is by searching for ULXs.

1.3.2 ULXs in Globular Clusters

Because the X-ray luminosity of ULX sources exceeds the Eddington limit for a 10 solar mass black hole, these sources are good black hole candidates. However, not all ULXs are black holes! As previously discussed in Section 1.2.3, some ULXs in star-forming regions of galaxies were found to have pulsations, implying that the compact object is a neutron star (Bachetti et al., 2013).

For ULXs in globular clusters, a neutron star accretor is highly unlikely. While NSs are common in GCs, the conditions observed for the entire known samples of NS ULXs cannot be met in the cluster. For example,there are a number of major differences between the globular cluster environments and the star-forming regions: both due to physical differences in the binaries, and the formation and evolution history of the systems. Physically, the best explanation for high accretion rates onto neutron stars involves extremely strong magnetic fields. However, the highest magnetic field measured in any globular cluster X-ray binary is several orders of magnitude lower than what is necessary to drive super Eddington accretion onto a neutron star. Furthermore, the donor stars of ULXs in star-forming regions tend to be massive and hydrogen rich (Pintore et al., 2018). However, globular clusters are older populations which no longer host massive stars, and the donor stars of these binary systems must be lower mass and metal poor. The vast difference between these potential donor stars must therefore also be reflected in accretion mechanisms at high transfer rates for low mass X-ray binaries and high mass X-ray binaries. Lastly, the formation and evolution mechanisms are entirely different. The binary components of ULXs in star-forming regions of galaxies evolve together. The dynamic processes and interactions inside of the globular cluster environment form binaries by a completely different method. The crowded cluster environment has a much larger interaction rate, and the higher mass bodies preferentially exchange their binary companions for more massive objects (Rabolli, 1990; Hut et al., 1992). Therefore, many binary systems in a globular cluster are unlikely to remain with its original binary companion for long, and can exchange out multiple companions throughout its evolution (Heggie, 1975; Hut & Bahcall, 1983).

1.3.3 RZ2109

RZ2109 was the first discovered black hole candidate in a globular cluster (Maccarone et al., 2007). It is a highly variable and ultra luminous X-ray source that is physically associated with a spectroscopically confirmed globular cluster in NGC 4472. Because extragalactic globular clusters are unresolved in X-ray, variability is key in determining whether the high X-ray luminosity is due to a single source, or confusion from multiple X-ray binaries hosted in the cluster, as the light from multiple sources would not vary. RZ2109s extreme variability points to the X-ray emission being produced by a single, super Eddington binary, and the compact object being a black hole.

Optical spectroscopy of RZ2109 revealed a broad and luminous [OIII] emission line, with no significant hydrogen emission beyond the cluster continuum (Zepf et al., 2007; Steele et al., 2014). To date, this is the only observed [OIII] line in a GC which is broadened by thousands of kilometers per second. The high oxygen to hydrogen ratio implies that the donor star in the system is a white dwarf (a so-called "ultracompact X-ray binary"), making RZ2109 the only candidate ultracompact X-ray binary in an extragalactic globular cluster.

HST/STIS measurements show that the [OIII] emission line is spatially resolved (Peacock et al., 2012b). This implies that the emission is due to a large oxygen nebula flooding the cluster (on the scale of parsecs). RZ2109's uniqueness in multiple wavelengths has exciting implications for the nature of black hole sources in globular clusters.

1.4 Implications of This Work

The question of whether globular clusters host black holes, and if so, how many and what masses, has been a long-standing question in astronomy. Currently, two BHs in a GC have been dynamically measured, and $\sim$ 15 candidates have been identified. Because of the dynamics of the crowded GC environment, they should be extremely efficient at forming BBH binaries, such as those detected merging by LIGO. LIGO is detecting many more BBH binaries than was ever expected, and a first step to understanding the formation of these binaries is to understand BHs in GCs. However, very few ways exist to study BHs in GCs observationally, and there is only one effective method to study BH candidates in extragalactic GCs: ULXs in GCs, which is the focus of this thesis.

Therefore, this work not only has multiple implications for both ULXs as a whole and globular clusters, but also the history behind the progenitors of the LIGO BBHs. Studying globular cluster ULX sources can not only shed light on the nature of black holes in globular clusters, but can also define a new class of ULXs in a very old and dynamic environment. Their nature and numbers has implications for understanding the progenitors of the LIGO sources, the question of black holes in globular clusters, even the formation and evolution of the clusters themselves, in addition to extending the knowledge of ULXs as a whole.

Major results of publications in this work include a potential correlation between X-ray behavior and presence of optical emission for globular cluster ULXs, and new discoveries about the variable nature of RZ2109.

1.5 Outline

Chapter two consists of the peer reviewed article written by Dage et al (2018) which is published in the Astrophysical Journal. It covers long-term monitoring (almost 20 years) in X-ray of RZ2109. The data shows significant variability, with the source dropping in luminosity by almost an order of magnitude over the course of only two days. Curiously, the shape of the X-ray spectrum remains the same. This is an unusual find, as typically any variability in flux is expected to be correlated with a change in the spectral properties of the source (i.e. some physical change in the system). The persistence of spectral parameters, along with the rapid variability, make RZ2109 stand out from the rest of the ULX population.

Chapter three consists of the peer reviewed article written by Dage et al (2019) which is published in the Monthly Notices of The Royal Astronomical Society. We compare RZ2109 to the larger sample of GC ULXs, by expanding our sample and analyzing X-ray data of eight more globular cluster ULX sources in NGC 4472, NGC 4649 and NGC 1399. The sources are either best fit by power-law models, or by softer multi-component blackbody disk models.

In the case of the softer (disk) models, the fits were bimodal: either the sources are better fit by a higher disk temperature or (like RZ2109) had a lower disk temperature with the spectral parameter constant while varying in luminosity. There is a likely correlation between the disk temperature and whether or not the source has optical emission, as the optical spectra of the low kT sources show optical emission, and a number of the higher kT sources have no emission beyond the cluster continuum

Chapter four consists of the peer reviewd article written by Dage et al (2019) which is published in the Monthly Notices of The Royal Astronomical Society. We find that the optical emission of RZ2109 spends almost ten years in a long-term decline, before re-brightening. Because the oxygen is likely being ionized by the X-ray emission, one expects a correlation, albeit over longer timescales (due to the nebula size). We compare the optical emission to the highly variable X-ray emission, and discuss what implication these observations have for the size scale of the nebula.

Chapter 2

X-ray variability from the ultraluminous black hole candidate X-ray binary in the globular cluster RZ 2109

2.1 Introduction

Determining whether or not globular clusters host black holes, and if so how many and what masses has been the subject of both longstanding interest and current theoretical work (e.g. Spitzer 1969 to Chatterjee et al. 2017). This interest has grown dramatically with the detection of merging black holes by LIGO (Abbott et al., 2016a), as black hole mergers in globular clusters are one of the leading possibilities for the origin of the LIGO sources (e.g, Abbott et al., 2016b; Rodriguez et al., 2016). There is little question black holes are present early in the life of a globular clusters - hundreds to thousands of stellar mass black holes are expected to be produced in typical globular clusters as the result of standard stellar evolution (e.g., Ivanova et al., 2010). Early work suggested that dynamical interactions among the black holes may eject many or almost all of them (e.g. Kulkarni et al. 1993, Sigurdsson & Hernquist 1993). However, recent simulations have found that this process is not as efficient as earlier expectations and current models generally predict the retention of a significant number of black holes in globular clusters (e.g. Morscher et al. 2015, Heggie & Giersz 2014, Sippel & Hurley 2013).

From an observational perspective, some of the first and strongest evidence for the presence of black holes in globular clusters has come from X-ray and optical studies of extragalactic globular clusters. One way to find black hole candidates in globular clusters is to identify globular cluster X-ray sources with luminosities in excess of the Eddington limit for an accreting neutron star, which may be indicative of a more massive black hole primary. No such source is found in Galactic globular clusters. However, over the very large sample of extragalactic globular clusters a number of such sources have now been identified in Chandra observations of early-type galaxies in the local universe. Because extragalactic globular clusters are unresolved in the X-rays, short term variability in these ultraluminous X-ray sources (ULXs) is critical for eliminating the possibility that the high X-ray luminosity arises from the superposition of multiple accreting neutron stars (e.g., Kalogera et al., 2004). A handful of such high L_X, variable sources are now known, starting with RZ2109 (Maccarone et al., 2007), making these among the best candidates for accreting black holes in globular clusters (e.g. Roberts et al. (2012), Maccarone et al. (2011), Irwin et al. (2010) and references therein).

Additional information about these ultraluminous sources can help constrain the nature of the accreting system. For example the source in RZ2109 has strong [OIII]4959,5007 emission with a velocity width of several thousand km/s and absolutely no hydrogen observed in emission (Zepf et al., 2008). The strong presence of [OIII]5007 and absence of Hβ is indicative of accretion from a very O-rich and H-poor donor, for which a CO white dwarf seems most likely (Steele et al., 2014). The broad velocity and high luminosity of the outflow is also consistent with outflows from sources accreting around their Eddington limit, based on both empirical and theoretical work (Zepf et al., 2008, and references therein) Moreover, the [OIII]5007 can not be strongly beamed. Therefore, the lack of similar [OIII] emission in objects without high L_X places valuable limits on any beaming of the X-rays in the RZ2109 source.

It is also interesting to compare the ULXs discovered in globular clusters with the more widely known ULXs in star forming galaxies (see Kaaret et al. (2017) for a review of the latter). While sharing the property of high X-ray luminosity, there are many differences between these populations. The donor stars in the star forming ULX systems are typically high mass stars, while such stars are long dead in globular clusters, and the donor stars in globular cluster systems are either white dwarfs (as in RZ2109, Steele et al., 2014) or other lower mass stars. Moreover, for a ULX in a star forming galaxy the accreting compact object will have been recently formed, and in the case of a neutron star may have an extremely high magnetic field. In contrast, globular clusters have populations of compact objects that formed long ago which can make close binary systems through dynamical interactions within the globular cluster (Ivanova et al., 2010).

These underlying physical differences may be matched to observational differences between the star forming and globular cluster ULXs. One of the most striking results in the study of ULXs in star forming galaxies is that at least some of the ULXs have accretors that are neutron stars rather than black holes and are thus accreting at many times their formal Eddington limit (e.g. Bachetti et al. 2014, Fürst et al. 2016, Israel et al. 2017b, Israel et al. 2017a). Models to account for these generally involve some combination of extremely large magnetic fields and beaming (review by Kaaret et al. (2017) and references therein). Because most of these models predict that pulses will not be observed at all times and depend on various geometries, it is possible that many ULXs in star forming galaxies are neutron star accretors (King et al. 2017, Middleton & King 2017).

The likely absence of both extreme magnetic fields and substantial beaming differentiates globular cluster ULX sources like RZ2109 from some star forming ULXs and supports identifying the RZ2109 accretor as a black hole (Peacock et al., 2012b). However, studies of ULXs in star forming galaxies provide an extensive set of phenomenological and theoretical work on super-Eddington accretion onto compact objects and its observational manifestations to which observations of RZ2109 can be compared (e.g. Poutanen et al. 2007, Gladstone et al. 2009, Sutton et al. 2013, Middleton et al. 2015). Broadly speaking these papers relate accretion rate relative to Eddington and viewing angle to observed properties such as X-ray spectrum, luminosity, and possible variability based on various assumptions about the underlying astrophysics (see review by Kaaret et al., 2017).

The goal of this paper is to analyze the now large number of X-ray observations of RZ2109 over 16 years, with the aim of constraining the nature of this likely accreting black hole system. RZ2109 is a very well-studied system, with extensive optical spectroscopy (Steele et al. (2014), **?**, Zepf et al. (2008) and references therein), and several extant X-ray studies utilizing Chandra and XMM-Newton. Here we report multiple new Chandra and XMM-Newton observations, and combine these with archival data to study the variability of the X-ray emission from RZ2109 over a broad range of time scales. The paper is arranged so that the observations are presented in Section 3.2, the results from the analysis of these observation in Section 3.3, and the conclusions in Section 3.4.

2.2 Data and analysis

RZ2109 has been observed numerous times by *XMM-Newton* and *Chandra* observatories over the last 16 years. We reduced and analyzed all of these observations as tabulated in Table 2.1. The background flare filtered (see further in text for details) *XMM-Newton* net count rates were obtained by filtering the energy in the range 0.3-10 keV in the spectral extraction. We then loaded the spectra into XSPEC, and obtained the net count rates (with no model) by using the show rate command. The *Chandra* source count rates were calculated using funtools [1] to list the counts in the source and background areas based on an image filtered in the 0.3-10 keV range. We then background subtracted the average source counts and divided by the observation length.

Table 2.1: *Chandra* and background flare filtered *XMM-Newton* observations, background subtracted average source count rates and raw source counts in 0.3-10 keV.

ObsID	Date	Exposure (ks)	Avg. Rate count/s	Src. Counts
322 [2]	2000-03-19	10	4.3×10^{-3}	48
321	2000-06-12	40	8.7×10^{-3}	398
8095	2008-02-23	5	1.1×10^{-2}	60
11274	2010-02-27	40	2.1×10^{-4}	19
12978	2010-11-20	20	9.6×10^{-4}	19
12889	2011-02-14	140	2.4×10^{-3}	425
12888	2011-02-21	160	1.0×10^{-3}	230
16260	2014-08-04	25	3.1×10^{-3}	79
16261	2015-02-24	25	9.0×10^{-5}	3
16262	2016-04-30	25	5.6×10^{-4}	16
0112550601[3]	2002-06-05	11	2.3×10^{-2}	282
0200130101	2004-01-01	72	4.5×10^{-3}	465
0761630101	2016-01-05	44	2.1×10^{-2}	1147
0761630201	2016-01-07	35	4.3×10^{-4}	29
0761630301	2016-01-09	65	3.9×10^{-4}	217

---

[1] https://github.com/ericmandel/funtools

2.2.1 Observations

The *Chandra* observations include both three new datasets we obtained in 2014, 2015, and 2016, and archival data going back to 2000. We used CIAO version 4.9 [4] (Fruscione et al., 2006) for analysis of all *Chandra* data. For most on-axis observations, we manually extracted the spectrum from the source and background regions using `specextract`. For off-axis observations we used ACIS-EXTRACT [5] (Broos et al., 2012) to extract the source regions (Broos et al., 2012). Specifically, in observations 12888 and 12889, the source is located on ACIS chip 8 and thus far off-axis. Additionally in observation 12888, it is located on the edge of this chip and is affected by dithering and edge effects. Given these issues and low signal-to-noise ratio of the detection in these observations, we used ACIS-EXTRACT to extract the spectra. Source extraction regions constructed by ACIS-EXTRACT are polygons approximating *Chandra*-ACIS point spread function based on MARX (Davis et al., 2012) simulations[6]. ACIS-EXTRACT also applies PSF corrections to ancillary response files (ARF) and exposure and background scaling corrections to the spectrum to take into account edge effects.

RZ2109 was also observed with *XMM-Newton* in 2002, 2004, 2008[7], and three times in 2016 (see Table 2.1). We used SAS 16.1.0[8] to extract the spectra from the MOS1, MOS2 and pn detections.

We set FLAG== 0 to screen conservatively [9], and originally extracted single and double

---

[4] http://cxc.harvard.edu/ciao/

[5] http://www2.astro.psu.edu/xray/docs/TARA/ae_users_guide.html

[6] We note that MARX 5.0, 5.1, and 5.2 simulate PSF of off-axis sources inaccurately (see https://github.com/Chandra-MARX/marx/pull/21). We have used MARX 5.3.2 for this work, which has addressed this issue.

[7] Observation 0510011501 did not have enough information left post-background flare filtering and thus is not used in this analysis.

[8] https://www.cosmos.esa.int/web/xmm-newton/sas

[9] https://heasarc.gsfc.nasa.gov/docs/xmm/hera_guide/node33.html

events (pattern <= 4) as recommended for *XMM* pn, however, in observations heavily impacted with flares (0200130101, 0761630201, and 0761630301), we only extracted single events (pattern == 0). For MOS1 and MOS2, we select (pattern<=12). The data was filtered for high background flares by only selecting times at which the background was constant. Those times were determined by examining the background light curve from the PPS. We ignored any counts below 0.2 keV. To account for differences among the three detectors when fitting, a constant factor was added to the best fit models; the value for pn was frozen at 1.0, while the values for MOS1 and MOS2 were free.

We used XSPEC version 12.9.1[10] (Arnaud, 1996) to analyze the X-ray spectra of both new and archival *Chandra* and *XMM-Newton* observations. All XSPEC analysis used the abundance of elements from Wilms et al. (2000).

We used the *F-test* function to compare the χ^2 statistics of a single disk component model with an absorption term to a two component model (disk component added to a powerlaw model pegged from 0.5-8 keV, also with absorption) for the three *Chandra* observations with the highest counts (321, 12888, and 12889). The probability that the improved fit statistics of the two component model is due to chance is respectively: 0.002, 0.006, 1.4e-05. Similarly, the *F-test* probabilities of a single powerlaw model with absorption compared to the absorbed two component model are: 0.047, 0.047 and 0.001. Therefore, we fit a multicolor disk (MCD) model (`diskbb`) added to a power law `pegpwrlw`, and multiplied by the absorption component to all observations. We note for completeness that if a power law is fit as a single-component model to the *Chandra* data, its index is in the range from 3.2 to 4.3, while the *XMM-Newton* data typically have a single-component powerlaw index around 3.0. In all our fits, we include an absorption term, `tbabs`, fixed to a foreground hydrogen

---

[10] https://heasarc.gsfc.nasa.gov/xanadu/xspec/

column density of $N_H = 1.6 \times 10^{20}$ cm^{-2} [11]. We found no evidence for a second absorption column; we fit the highest count *Chandra* data with a second absorption parameter and found that in each case, the best fit value was consistent with zero.

For the bulk of the observations χ^2 was used as the fitting statistic. Spectra with more than 100 source counts were binned in groups of 20; spectra with fewer counts than that were binned with 1 count per bin and fit with c-stats (Cash, 1979).

To estimate the unabsorbed fluxes in the 0.5-8keV range we used XSPEC's multiplicative model `cflux` [12] with the best fit spectral model. After adding in the cflux component and refitting, we then used the error command in XSPEC on the flux parameter and obtained upper and lower bounds on the fluxes of each observation to the 90% confidence interval. All parameter errors were also obtained in this manner.

While all of our fitting is carried out in the 0.5-8keV range appropriate for *Chandra* data, many X-ray results are given in the 0.2-10 keV range. Therefore to compare to other work, we calculate the 0.2-10 keV fluxes and luminosities based on our spectral fits to the data from 0.5-8 keV, also using `cflux`.

Tables 2.2, 2.3, 2.4, and 2.5 show best fit parameters, fit statistics and the fitted flux for *Chandra* and *XMM-Newton* observations respectively. The fluxes and fit parameters are also plotted in Figure 2.1.

Two *Chandra* observations have extremely low average source counts. Maccarone et al. (2010b) have previously found 19 source count rates with a background of 10.8 counts for obsID 11274, which, despite being highly off-axis, is significant at the 95% confidence level (Gehrels, 1986). In obsID 16261, we detect three counts in the source region, which - consid-

---

[11] http://cxc.harvard.edu/toolkit/colden.jsp

[12] https://heasarc.gsfc.nasa.gov/xanadu/xspec/manual/XSmodelCflux.html

Table 2.2: *Chandra* Fit Parameters for XSPEC best fit model `tbabs*(diskbb+pegpwrlw)`. Hydrogen column density (N_H) frozen to 1.6 $\times 10^{20}$ cm^{-2}.

Date	T_{in} (keV)	Disk Norm[13]	Γ	Powerlaw Flux (erg cm^2 s $^{-1}$)	χ^2_ν/d.o.f. [14]
2000-03-19	$0.11\ ^{+0.04}_{-0.03}$	$107\ ^{+670}_{-90}$	$1.3\ ^{+1.2}_{-1.1}$	$3.0(^{+2.5}_{-1.4})\times10^{-14}$	N/A [15]
2000-06-12	0.12 ± 0.02	68^{+85}_{-34}	1.7 ± 0.5	$3.8(\pm0.8)\times10^{-14}$	3.14/16
2008-02-23	$0.13\ ^{+0.03}_{-0.02}$	60^{+164}_{-42}	$0.5\ ^{+1.4}_{-2.5}$	$2.2(^{+2.7}_{-1.8})\times10^{-14}$	N/A [16]
2010-02-27 [17]	—	—	(3.5) [18]	$9.2\ (^{+10.0}_{-6.2})\ \times10^{-16}$	—
2010-11-20	$0.13\ ^{+0.08}_{-0.04}$	$3.1^{+38.3}_{-2.9}$	$0.2^{+1.6}_{-2.1}$	$6.7\ (^{+10.0}_{-4.5})\ \times10^{-15}$	N/A [19]
2011-02-14	0.13 ± 0.02	$21\ ^{+36}_{-14}$	1.3 ± 0.6	$1.9\ (\pm0.4\ )\times10^{-14}$	1.19/16
2011-02-21	0.11 ± 0.03	$30\ ^{+135}_{-23}$	1.8 ± 0.6	$1.0\ (\pm0.2\ )\times10^{-14}$	1.69/7
2014-08-04	$0.12\ ^{+0.04}_{-0.03}$	$39\ ^{+233}_{-34}$	2.0 ± 0.7	$2.6(\pm0.8)\times10^{-14}$	N/A [20]
2015-02-24 [21]	—	—	(3.5)	$9.3(^{+27.7}_{-7.9})\times10^{-16}$	—
2016-04-30	0.09 ± 0.05	$242\ ^{2169}_{-239}$	$1.8^{+1.5}_{-1.6}$	$6.9(^{+5.0}_{-3.5})\times10^{-15}$	N/A [22]

Table 2.3: *Chandra* Fluxes (0.5-8 keV) for XSPEC best fit model `tbabs*(diskbb+pegpwrlw)`.

Date	Unabsorbed Flux (erg cm^2 s^{-1})
2000-03-19	$5.7(^{+2.4}_{-1.6})\ \times10^{-14}$
2000-06-12	$7.0\ (\pm0.9)\ \times10^{-14}$
2008-02-23	$4.5(^{+1.2}_{-1.0})\times10^{-14}$
2010-02-27	$9.2(^{+10.0}_{-6.2})\ \times10^{-16}$
2010-11-20	$9.6(^{+8.8}_{-4.6})\times\ 10^{-15}$
2011-02-14	$03.6(\pm0.4)\times10^{-14}$
2011-02-21	$1.6(\pm0.3)\times10^{-14}$
2014-08-04	$2.8(^{+0.6}_{-0.5})\times10^{-14}$
2015-02-24	$9.3(^{+27.7}_{-7.9})\times10^{-16}$
2016-04-30	$2.0(^{+1.1}_{-0.8})\times10^{-14}$

Table 2.4: *XMM-Newton* Fit Parameters for XSPEC model `tbabs*(diskbb+pegpwrlw)`. Hydrogen column density (N_H) frozen to 1.6 $\times 10^{20}$ cm^{-2}.

Date	T_{in} (keV)	Disk Norm[24]	Γ	Powerlaw Flux	χ^2_ν/d.o.f. [25]
2002-06-05	$0.14\,^{+0.06}_{-0.02}$	18^{+25}_{-16}	$2.6\,^{+0.7}_{-3.9}$	$3.9\ (\pm\ 1.5)\times 10^{-14}$	1.73/16
2004-01-01	$0.17\ \pm 0.02$	$1.8\,^{+0.8}_{-0.5}$	$0.6\,^{+0.7}_{-0.9}$	$9.2(^{+3.7}_{-3.4})\times 10^{-15}$	2.31/45
2016-01-05	0.16 ± 0.01	$7.2\,^{+2.6}_{-1.8}$	$1.0\ \pm 0.4$	$2.7\ (\pm\ 0.5)\times 10^{-14}$	1.38/56
2016-01-07	Upper Limit Only	—-	—	—	—
2016-01-09	$0.15^{+0.15}_{-0.02}$	$0.2\,^{+1.4}_{-0.1}$	$1.4\,^{+1.4}_{-0.6}$	$\leq 7.0\times 10^{-15}$	0.59/6

Table 2.5: *Chandra* Fluxes (0.5-8 keV) for XSPEC best fit model `tbabs*(diskbb+pegpwrlw)`.

Date	CCF Constant pn/MOS1/MOS2	Unabsorbed Flux (erg cm^2 s^{-1})
2002-06-05	(1.0)/1.20/0.83	$6.3\ (^{+3.8}_{-1.0})\times 10^{-14}$
2004-01-01[26]	(1.0)/1.57/1.59	$1.7\ (\pm 0.4)\times 10^{-14}$
2016-01-05	(1.0)/0.85/1.08	$5.0\ (\pm 0.6)\ \times 10^{-14}$
2016-01-07	—	$8.9(^{+13.0}_{-8.2})\times 10^{-16}$
2016-01-09	N/A [27]	$2.3(^{+5.2}_{-2.2})\times 10^{-15}$

ering the expected scaled background of 1 count - is also significant at the 95% confidence level. To estimate a flux for both of these observations, we took the background subtracted count rates and used PIMMS [23] to fit with a powerlaw index of 3.5, which was the common best fit to the single powerlaw model of the other *Chandra* data. *XMM-Newton* observation 0761630201 had very few counts left post background flare filtering. This, in conjunction with a relatively high background ($\simeq$ 50%) meant that detailed spectral analysis was not possible. However, we were able to fit a single component disk model to the data and obtain a flux using `cflux`. This lends significant uncertainty to this flux estimate.

---

[23] http://cxc.harvard.edu/toolkit/pimms.jsp

2.3 Results

The overall goal of this paper is to monitor variations in the X-ray luminosity of RZ2109 over the time covered by all of the available data, ranging from 2000 to 2016. Figure 2.2 shows the luminosities in the 0.2-10 keV range, which were calculated using the fluxes from Section 3.2 and a distance of 16.1 Mpc (Macri et al., 1999). The luminosities are also listed in Table 2.6.

One of the main results apparent from Figure 2.2 and Table 2.6 is that RZ2109 varies significantly over all of the time scales observed, from days to years. During some observations RZ2109 is observed to have $L_X \sim 4 \times 10^{39}$ erg s^{-1}, while at other times it is observed to have $L_X \sim 2 - 3 \times 10^{38}$ erg s^{-1} or even fainter, along with various times at which RZ2109 is found to be between these luminosities. This variability is surprising because there is strong evidence in other ways that the source is a stellar mass black hole accreting material from a carbon-oxygen white dwarf at a very high rate, at or somewhat above its formal Eddington limit (e.g., Peacock et al., 2012a; Roberts et al., 2012). In such a case the source is expected to be persistent because accretion disks in high luminosity, short period ultracompacts like this are not expected to have ionization instabilities (e.g., Maccarone et al., 2010a). While there are beginning to be counter-examples to this argument (see Maccarone et al., 2010a), understanding such systems may give important clues to the formation and accretion processes in these globular cluster black hole sources. It is interesting to compare the variability of RZ2109 to that of other ultraluminous X-ray sources in extragalactic globular clusters. Of the six such sources published - Maccarone et al. (2007), Brassington et al. (2010); Shih et al. (2010); Irwin et al. (2010); Maccarone et al. (2011); Roberts et al. (2012), all vary, with at least three of them varying by more than an order of magnitude. There is a need to be careful about variability in this list, because variability is also one of the criteria to ensure that most of the X-ray flux comes from a single source and not multiple sources in the globular cluster, and variability is one of the criteria used in these papers. However, in these cases, the ultraluminous sources are typically the brightest X-ray sources among the globular cluster sources in each galaxy. So substantial and large variability appears to be the norm for ultraluminous X-ray sources in extragalactic globular clusters.

Given the luminosity variability observed in these sources, it is natural to test whether there is any corresponding spectral variability. A key feature of the variability RZ2109 found here is that there is often *no* evidence for corresponding changes in the X-ray spectra of RZ2109. The similarity of the X-ray spectra at different observed fluxes can be seen in Tables 2.2, 2.3, 2.4 and 2.5 and Figure 2.1. This result is different than that found in the original variability discovery for RZ2109 which showed that the decrease in flux seen within the 2002 *XMM-Newton* observation was driven by a decrease in the soft component that can be interpreted as a change in the column density of absorbing material along the line of sight (Maccarone et al. 2007, Shih et al. 2008). While this is still true for the flux change within the 2002 *XMM-Newton* observation, such a model can not explain most of the variability among the many observations shown here. Other ULX sources in extragalactic globular clusters show a range of behavior in the relationship between luminosity and spectral variability. Shih et al. (2010) find a ULX in an extragalactic globular cluster in NGC 1399 with more than a factor of ten decrease in luminosity and no evident change in spectral shape. On the other hand, a different extragalactic globular cluster ULX in NGC 4649 studied by Roberts et al. (2012) does exhibit spectral changes in some observations. The overall picture is that some spectral variability happens, but there are clear observations in multiple sources of little or no spectral variability even with order of magnitude luminosity changes.

It is also natural to ask whether there is any overall longterm trend of L_X with time for RZ2109. Unfortunately the data are not quite adequate for addressing this question specifically. It is intriguing that many of the fainter fluxes appear to be found at more recent times. However, there are observations in 2014 and 2016 in which $L_X \simeq 3 \times 10^{39}$ erg s^{-1}, and thus well within the ULX regime and not much different than observations in 2000 and 2002. Given the short term variability clearly evident in RZ2109, one way to get at the long-term changes in RZ2109 may be to study its [OIII]5007 emission which appears to be emitted over a region of light months to light years, and therefore samples the overall photoionizing flux averaged over those timescales (Peacock et al., 2012b). The physical origin of the variability RZ2109 has not yet been established. As noted above, the accretion disk is not expected to be subject to ionization instabilities, so a different mechanism must be operating.

One natural mechanism to produce changes in the accretion rate over time is to have small changes in the eccentricity of the orbit (e.g., Hut & Paczynski, 1984), perhaps due to the Kozai mechanism (Kozai, 1962), in which a lower mass third star in an outer orbit introduces eccentricity into the main two body system. For typical parameters for an RZ2109-like system and a mass of the third star of $0.5 M_\odot$, the Kozai timescale is roughly a decade. This therefore may account for any long term trend we may see in RZ2109, but not very short term variability. This is why it was attractive originally to try to explain RZ2109's variability with varying absorption, but such an explanation fails to account for the absence of spectral changes seen in many datasets since. Other possibilities for short-term variability are listed in the Maccarone et al. (2010a) study of similar variability of the Galactic ultracompact binary 4U 0513−40. These possibilities include tidal disc instabilities (e.g., Whitehurst, 1988; Osaki, 1995) and irradiation of the donor star leading to modulations of the accretion rate (e.g., Hameury et al., 1986). It is not yet clear whether these can account for variability observed in RZ2109.

The observed X-ray spectrum and variability of RZ2109 can also be compared to the well-known ULXs observed in star forming galaxies (Kaaret et al., 2017). Compared to most of these ULXs not in globular clusters, RZ2109 is significantly softer and much more variable. Within the field ULX population, there is a class of objects known as ultrasoft ULXs (ULSs) that are both softer and more variable than most ULXs (e.g., Earnshaw & Roberts, 2017; Urquhart & Soria, 2016). These papers also find that the variability in ULSs is primarily at higher X-ray energies, although there is an exception to this general characteristic (Feng et al., 2016). Thus RZ2109 differs from most field ULSs in that its variability is either mostly at low energies (e.g., Shih et al., 2008), or the luminosity varies equally at all energies, as shown above.

That the globular cluster ULXs are different than most ULXs in star forming galaxies is not surprising. Globular cluster ULXs are essentially low-mass X-ray binaries (LMXBs) and nearly all field ULXs are high mass X-ray binaries (HMXBs). The binaries that make the globular cluster ULXs are also likely to be formed by dynamical interactions within the globular cluster (Ivanova et al., 2010), unlike the binary stellar evolution that makes field ULXs. As a result, the accretor in globular cluster ULXs is likely to be much older and thus not have the large magnetic fields often proposed for field ULXs. Differences in the donor stars will also be significant in globular cluster ULXs compared to field ULXs. Globular cluster sources will have old, low-mass donors while star forming ULXs typically have young, higher mass donors. This leads to differences in the orbital parameters and the composition of the accreted material, among others, which then may have implications for the resulting observables in the ULXs.

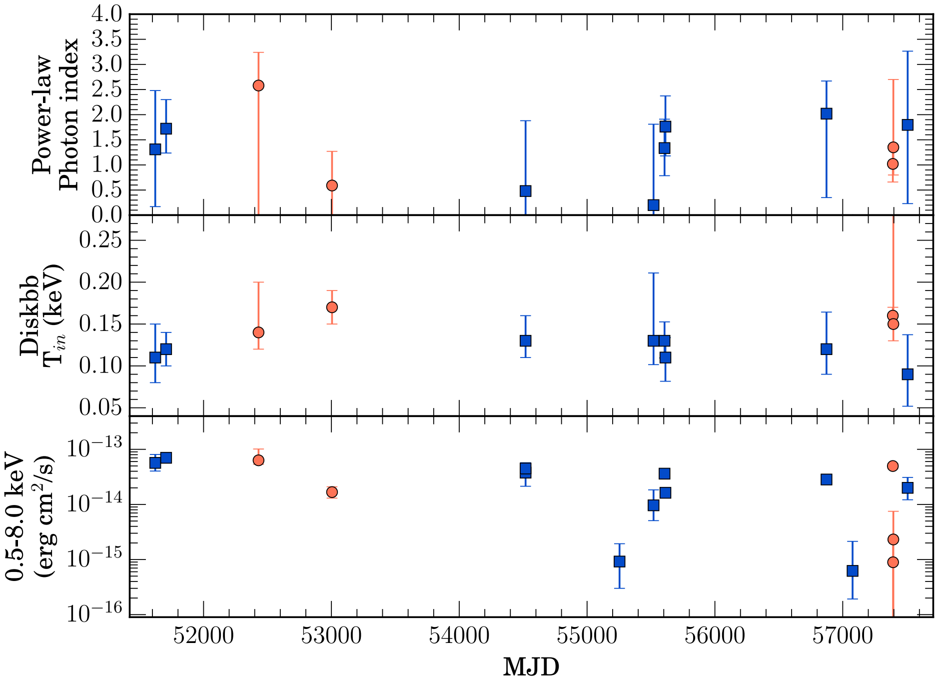

Figure 2.1: Top panel shows best fit powerlaw index for *Chandra* and *XMM* observations, middle panel shows disk temperature, lowest panel shows calculated unabsorbed model flux. *Chandra* data is represented by blue squares, and the *XMM-Newton* data by orange circles. All parameters and fluxes are in the 0.5-8 keV band.

2.4 Conclusions

We confirm long-term variability in the X-ray emission from the globular cluster black-hole candidate source XMMUJ122939.9+075333 in the extragalactic globular cluster RZ2109. The system shows strong luminosity variability over long and short time scales, dropping anywhere from as low as $L_X \simeq 7 \times 10^{37}$ erg s^{-1} to as high as $L_X \simeq 5 \times 10^{39}$ erg s^{-1}. The system also underwent significant changes in luminosity over very short time scales: observations four days apart from each other showed a drop in luminosity by almost a factor of five. Over 16 years of X-ray monitoring, the spectral shape remains extremely soft. The fitted *Chandra* and *XMM-Newton* spectra for the high count observations can be seen in Figures 2.3-3.5. While the fit quality is too low to make any statements in regards to

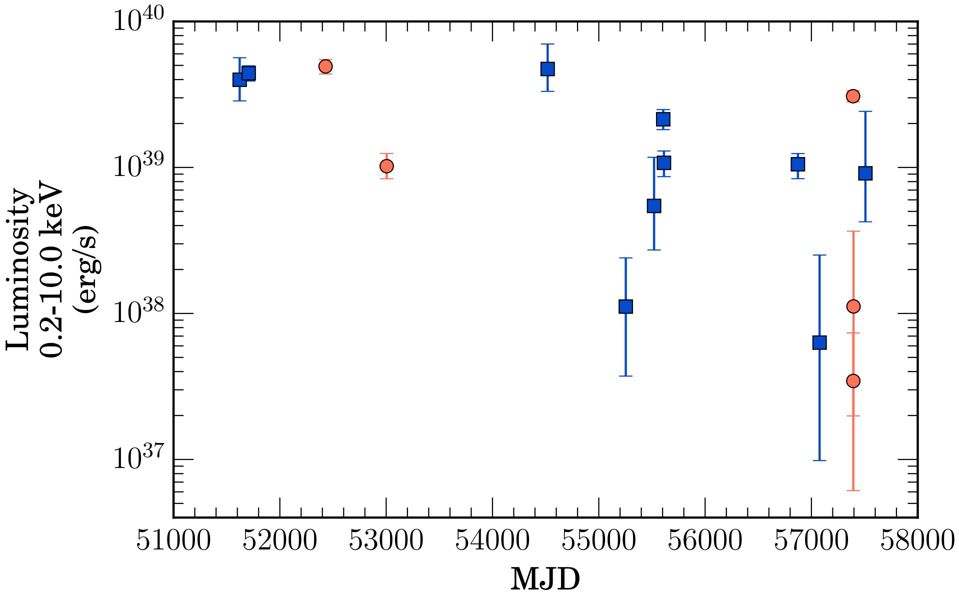

Figure 2.2: Luminosity variability of RZ2109 in energy band 0.2-10.0 keV. *Chandra* data is represented by blue squares, and the *XMM-Newton* data by orange circles.

spectral variability, it is remarkable how consistently soft the spectra are.

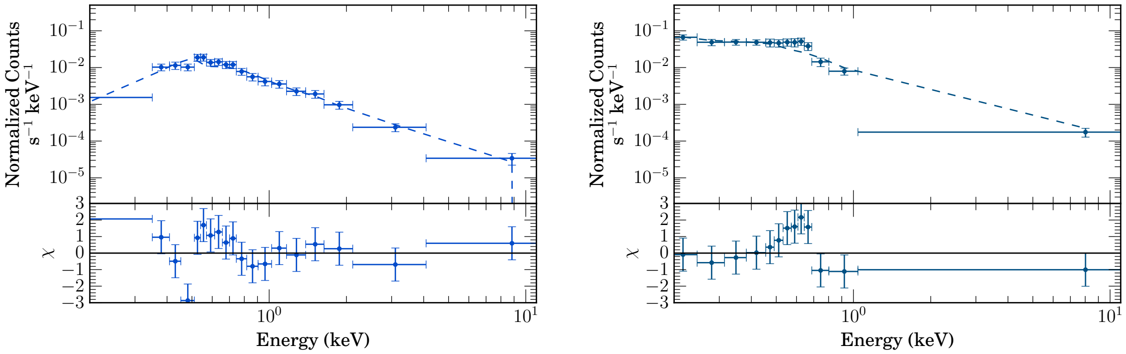

Figure 2.3: Left: Fitted spectrum with residuals of *Chandra* ObsID 321 (2000-06-12). Right: Fitted spectrum with residuals of *XMM-Newton* observation 0112550601 (2002-06-05, pn only).

Acknowledgements

KCD, SEZ, and MBP acknowledge support from Chandra grant GO4-15089A. SEZ and MBP also acknowledge support from the NASA ADAP grant NNX15AI71G. This research

Table 2.6: All luminosities in 0.2-10 keV.

Date	Luminosity (erg s^{-1})	Lower Bound (erg s^{-1})	Upper Bound (erg s^{-1})	Obs
2000-03-19	4.0×10^{39}	2.9×10^{39}	5.6×10^{39}	Chandra
2000-06-12	4.4×10^{39}	3.9×10^{39}	6.0×10^{39}	Chandra
2002-06-05	4.9×10^{39}	4.4×10^{39}	5.5×10^{39}	XMM
2004-01-01	1.0×10^{39}	8.4×10^{38}	1.3×10^{39}	XMM
2008-02-23	4.7×10^{39}	3.3×10^{39}	7.0×10^{39}	Chandra
2010-02-27	7.4×10^{37}	1.1×10^{38}	1.3×10^{38}	Chandra
2010-11-20	5.5×10^{38}	2.7×10^{38}	1.2×10^{39}	Chandra
2011-02-14	2.1×10^{39}	1.8×10^{39}	2.5×10^{39}	Chandra
2011-02-21	1.1×10^{39}	8.7×10^{38}	1.3×10^{39}	Chandra
2014-08-04	2.7×10^{39}	2.0×10^{39}	3.3×10^{39}	Chandra
2015-02-24	6.3×10^{37}	9.8×10^{36}	2.74×10^{38}	Chandra
2016-01-05	3.1×10^{39}	2.8×10^{39}	3.4×10^{39}	XMM
2016-01-07	5.2×10^{38}	4.9×10^{38}	5.6×10^{38}	XMM
2016-01-09	3.5×10^{37}	6.1×10^{36}	7.4×10^{37}	XMM
2016-04-30	1.2×10^{38}	2.0×10^{37}	3.7×10^{38}	Chandra

has made use of data obtained from the Chandra Data Archive and the Chandra Source Catalog, and is based on observations obtained with XMM-Newton, an ESA science mission with instruments and contributions directly funded by ESA Member States and NASA. We also acknowledge use of NASA's Astrophysics Data System and Arxiv.

Software The following softwares and packages were used for analysis: CIAO, software provided by the Chandra X-ray Center (CXC), HEASOFT obtained from the High Energy Astrophysics Science Archive Research Center (HEASARC), a service of the Astrophysics Science Division at NASA/GSFC and of the Smithsonian Astrophysical Observatory's High Energy Astrophysics Division, SAS, the XMM-Newton Science Analysis System, SAOImage DS9, developed by Smithsonian Astrophysical Observatory, NUMPY (Van Der Walt et al., 2011), MATPLOTLIB (Hunter, 2007) and ASTROPY (Astropy Collaboration et al., 2013).

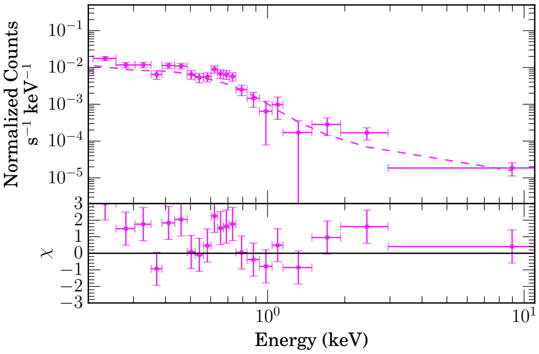

Figure 2.4: Fitted spectrum with residuals of *XMM-Newton* observation 0200130101 (2004-01-01, pn only).

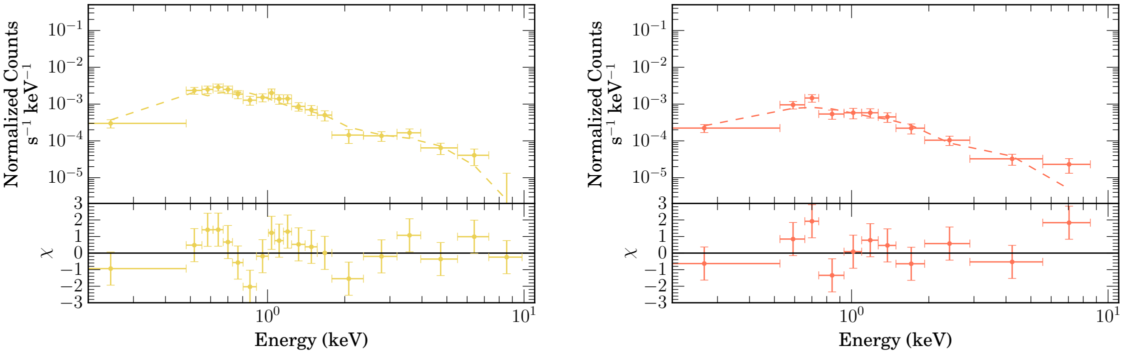

Figure 2.5: Left: Fitted spectrum with residuals of *Chandra* ObsID 12889 (2011-02-14). Right: Fitted spectrum with residuals of *Chandra* ObsID 12888 (2011-02-21).

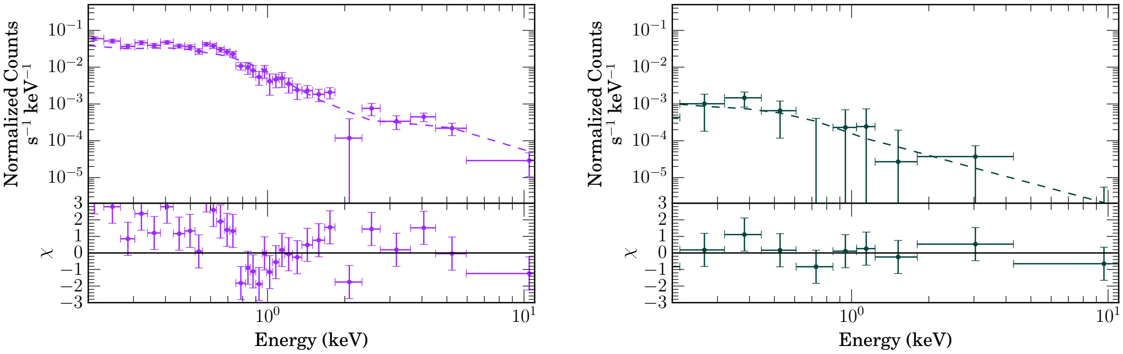

Figure 2.6: Left: Fitted spectrum with residuals of *XMM-Newton* observation 0761630101 (2016-01-05, pn only). Right: Fitted spectrum with residuals of *XMM-Newton* observation 0761630301 (2016-01-09, pn only).

Chapter 3

X-Ray Spectral Variability of Ultraluminous X-Ray Sources in Extragalactic Globular Clusters

3.1 Introduction

Ultraluminous X-ray sources (ULXs) are non-nuclear X-ray sources with luminosities significantly greater than the Eddington limit or a 10 solar mass black hole (BH). $L_X 10^{39}$ erg s^{-1} is often adopted as a general guideline for being well above this limit and therefore a ULX. This implies the accreting object in a ULX is either a black hole, or a neutron star (NS) with super-Eddington accretion and/or emission beamed along our line of sight. The most well studied ULX population is that in star forming galaxies (e.g. review by Kaaret et al. 2017). The ULXs with luminosities lower than 3 $\times 10^{39}$ erg s^{-1} are typically fit best by a singly peaked, broadened disk. The higher luminosity ULXs are fit by a two component disk and power law model, and are either "soft" or "hard", depending on the slope of the power law. The slope differentiates between $\sim$ Eddington and super-Eddington models (Gladstone et al., 2009; Sutton et al., 2013). These ULXs show strong luminosity variability that are often accompanied by significant changes in states/spectral shapes (Sutton et al., 2013; Bachetti et al., 2013; Walton et al., 2013; Feng et al., 2016). A third group of ULXs have also been identified, with luminosities below 3 $\times 10^{39}$ erg s^{-1} and soft blackbody dominated emission and are known as of "supersoft" ULXs (Urquhart & Soria, 2016).

Some optical counterparts have been identified for ULXs in star forming regions. These are primarily OB type giants or supergiants (Pintore et al., 2018, and references therein). High mass companion stars could provide an explanation for the high mass transfer rates which drive the high luminosities and account for their connection to star-forming regions (see Gladstone et al. 2009 and references therein).

Of the many sources confirmed as ULXs, a number of those associated with star forming galaxies have been found to have pulsations, implying that the compact object is a neutron star (e.g., Bachetti et al. 2014 to Pintore et al. 2018). Although ULXs in star forming galaxies have been studied extensively, ULXs also exist in a completely different environment: globular clusters (GCs). Since 2007, five globular cluster ULX sources have been studied in some depth: XMMUJ122939.7+075333 (RZ2109; Maccarone et al., 2007), CXOJ0338318-352604 (Irwin et al., 2010), CXOKMZJ033831.7−353058 (Shih et al., 2010), CXOU 1229410+0757442 (Maccarone et al., 2011), and CXOUJ1243469+113234 (Roberts et al., 2012). Some of these sources are proposed to have black hole primaries due to their highly variable ULX emission and other properties (Maccarone et al., 2007; Shih et al., 2010).

Interestingly, nebular emission is observed from some of these GC ULXs. Such emission is likely associated with the ULX, since it is extremely rare in globular clusters, which lack young stars and are known to have few planetary nebulae (Peacock et al., 2012b, and references therein). Their forbidden optical emission lines limit beaming to a factor of a few or less for some of these GC sources. While geometric beaming has been proposed as a mechanism for producing the super-Eddington X-ray emission from accreting neutron stars

(King et al., 2001), Peacock et al. (2012a) find that the optical emission from the GC ULX sources are too luminous to accommodate a large beaming factor and should be isotropically emitting. (See also Pakull & Mirioni (2002), and Binder et al. (2018) for a discussion of beaming in ULX sources.)

The presence of black holes in globular clusters, and if so, the properties the globular cluster black holes has been debated for many decades (see Spitzer 1969, Chatterjee et al. 2017, Park et al. 2017). While black holes are initially expected to form in globular clusters (Ivanova et al., 2010), early numerical simulations indicated that dynamical interactions within the globular cluster would cause the black holes to be ejected (Kulkarni et al., 1993; Sigurdsson & Hernquist, 1993). However, more recent work, (e.g., Morscher et al. 2013, 2015; Heggie & Giersz 2014; Sippel & Hurley 2013) show that the ejection time scales are much longer, and that stellar mass black holes remain well mixed in the cluster. In addition to this, globular clusters are prime environments for black hole mergers, and if black holes are retained in globular clusters, then globular clusters could be the progenitors of recent LIGO detections of merging black holes (see Abbott et al., 2016b; Rodriguez et al., 2016). Studying GC ULX sources could shed some light on the nature of black holes in globular clusters.

It is interesting to compare the ULX population in star forming regions to those in globular clusters, which are two very different environments. Firstly, the dense globular cluster environment is conducive to dynamical formation of binary systems, thus, GC ULXs are likely dynamically formed (Ivanova et al., 2010). The large interaction cross-section in this environment means that it is unlikely that the current binary partner of any compact object in a GC was a binary with the object when the stars initially formed and evolved. In contrast, ULX sources in star forming regions likely evolved from primordial binaries, and that the two objects in the binary evolved at the same time.

The donor stars in the two types of ULXs are also likely to be very different; due to the ages of globular clusters, 13 Gyr or so, the BHs and NSs were born from the massive stars in these GCs many Gyr ago. This very old age for these primordial BH and NS populations differs greatly from the young ages of the NSs and BHs formed from massive stars in currently star forming regions. For example, one such GC ULX source likely has a white dwarf as its donor star (Steele et al., 2014), but the ULXs in star-forming regions should have high mass donor stars, as mentioned previously.

One other difference between these ULX populations is that those in star forming regions have hydrogen emission present in their optical spectra (e.g., Fabrika et al., 2015), while at least three of the globular cluster ULXs have no hydrogen emission (Zepf et al., 2008; Irwin et al., 2010; Roberts et al., 2012). The most well studied GC ULX, RZ2109, also has very different X-ray behaviour from ULXs in star forming regions; it varies by more than an order of magnitude in X-ray luminosity between many different observations, but exhibits little or no variation in kT over those same observations (Shih et al., 2008; Dage et al., 2018).

Several studies have considered the nature of the GC ULX sources and their optical emission, although most of them tend to focus on the source RZ2109 (e.g., Zepf et al., 2008; Steele et al., 2011; Peacock et al., 2012a,b; Steele et al., 2014). There are also studies of the optical spectrum of the GC ULX CXOJ0338318-352604 in the galaxy NGC 1399 (Irwin et al., 2010). The emission lines of RZ2109 have been variously modelled as a $\sim 50 - 100$ $M_{\odot}$ mass black hole tidally disrupting a horizontal branch star (Clausen et al., 2012a) and as the ejecta from a R Corona Borealis star being photoionised by an unrelated X-ray source elsewhere in the cluster Maccarone & Warner (2011). The goal of this paper is to consider all known GC ULX sources to better understand their nature and constrain these models.

In this paper, we undertake an analysis of the eight known globular cluster ULXs with $L_X > 10^{39}$ erg s^{-1} to broaden our understanding of these sources. As noted above, three of these sources have been studied previously, while five are new to this paper. Section 3.2 discusses the *Chandra* observations and analysis, the results are presented in Section 3.3. The major results of the paper are discussed further in Section 3.4.

3.2 Data and Analysis

3.2.1 Globular Cluster ULX Sample

We consider low mass X-ray binaries (LMXBs) in the sample of seven local early-type galaxies as presented in Peacock et al. (2014). The galaxies studied are all within 20 Mpc and have deep Chandra observations of > 100 ksec. We select the targets that are located in GCs in these galaxies and that have X-ray luminosities greater than 10^{39} erg s^{-1}. The X-ray fluxes of the point sources in these galaxies are published by Paolillo et al. 2011 (NGC 1399), Brassington et al. 2008 (NGC 3379), Brassington et al. 2009 (NGC 4278), Joseph 2013 (NGC 4472), Li et al. 2010 (NGC 4594), Luo et al. 2013 (NGC 4649), and Sivakoff et al. 2008 (NGC 4697). Globular cluster X-ray sources were then identified from these catalogues by matching to optical counterparts in aligned HST optical images (see Peacock et al., 2014; Luo et al., 2013, for details). The resulting catalogue of high probability GC LMXB candidates is used to select ULX sources.

Sivakoff et al. (2007) predict that the X-ray luminosity of bright GC sources is dominated by a single high luminosity object and not from multiple fainter sources with a combined high luminosity. Many of the sources in our sample are also highly variable in X-ray, which also implies that most or all of the luminosity comes from a single source (see Maccarone et al. 2007 and Section 3.2.3 for further discussion of source variability). See Table 3.1 for source coordinates and optical cluster properties. We present new data and analysis of three of the previously studied sources (Irwin et al. 2010; Maccarone et al. 2011; Roberts et al. 2012), and new analysis of five GC ULXs which have not yet been previously studied in depth.

3.2.2 Spectral Fitting

We use archival *Chandra* data of NGC 1399, NGC 4472 and NGC 4649 (See Tables 3.2. For these observations, we use CIAO-4.9[1]'s (Fruscione et al., 2006) `specextract` function to extract the spectra, with approximately $2.5''$ circular regions on the sources, and set a series of 5-10 similarly shaped regions in source-less areas around the sources to select the background regions. We follow Dage et al. (2018) for all fitting of *Chandra* spectra. Observations with counts greater than 100 were binned by 20, those with less were binned by 1. We fit the spectra with with XSPEC[2] (Arnaud, 1996), using χ^2 statistics for the more detailed spectra and C-statistics[3] (Cash, 1979) for the spectra which were binned in counts of 1. We set the abundance of elements to Wilms (Wilms et al., 2000), and freeze the value of the equivalent hydrogen column absorption (nH) to the value for that galaxy[4]. We use the "ignore bad" command to remove bad channels.

All of the data were fit with two separate single component models. The first is a multi-temperature blackbody disk (`tbabs*diskbb`) (Mitsuda et al., 1984). The second is a pegged power law model (`tbabs*pegpwrlw`) with the normalisation pegged from 0.5-8.0 keV. We also

---

[1] `http://cxc.harvard.edu/ciao/`

[2] `https://heasarc.gsfc.nasa.gov/xanadu/xspec/`

[3] `https://heasarc.gsfc.nasa.gov/xanadu/xspec/manual/XSappendixStatistics.html`

[4] `http://cxc.harvard.edu/toolkit/colden.jsp`

Table 3.1: Coordinates and optical properties of the GC ULX sample. Optical properties from (Zepf et al., 2007, RZ2109) , (Maccarone et al., 2003, GCU1), Peacock et al. (2014, GCU2, GCU3, GCU4), (Strader et al., 2012b, GCU5, GCU6) and (Paolillo et al., 2011, GCU7, GCU8) All magnitudes are in z-band unless otherwise noted. Distances from Macri et al. 1999; Blakeslee et al. 2009, 2001. RZ2109 and GCU1's V magnitudes were converted to z by using the relation V = g - 0.39($g - z$) + 0.07 (Peacock et al., 2010), and metallicities converted to $g - z$ from B-R with the following relationship: $g - z$ = 1.305(B-R) - 0.543 (Peacock et al., 2010)..

Object	RA	Dec	z	$g - z$	Host Galaxy (Distance)
RZ2109	12:29:39.9	+07:53:33.3	20.4	0.84	NGC 4472 (16.8 Mpc)
GCU1	12:29:41.0	+07:57:44.2	20.8	NGC 4472 (16.8 Mpc)	
GCU2	12:29:34.5	+08:00:32.1	22.1	0.92	NGC 4472 (16.8 Mpc)
GCU3	12:29:42.3	+08:00:08.1	19.5	1.42	NGC 4472 (16.8 Mpc)
GCU4	12:29:34.5	+07:58:51.6	20.1	1.11	NGC 4472 (16.8 Mpc)
GCU5	12:43:46.9	+11:32:34	20.3	1.55	NGC 4649 (16.5 Mpc)
GCU6	12:43:44.5	+11:31:50	22.2	1.60	NGC 4649 (16.5 Mpc)
GCU7	03:38:31.8	-35:26:04	20.7	1.98	NGC 1399 (20.0 Mpc)
GCU8	03:38:32.6	-35:27:05.7	19.9	2.24	NGC 1399 (20.0 Mpc)

fit the high count (100 counts) data with a two component model `tbabs*(diskbb+pegpwrlw)`, and used F-test to determine if any improvement was statistically significant. Lastly, we determine to what extent (if any) there is intrinsic absorption in these systems by fitting a second absorbing column to the high count data (`tbabs*tbabs*pegpwrlw` and `tbabs*tbabs*diskbb`.)

The `pegpwrlw` model is normalised such that the best fit to the power law norm is the unabsorbed flux from 0.5-8.0 keV. To determine the unabsorbed flux in the models fit by `diskbb`,we multiply the models by `cflux`, with the energy range between 0.5 and 8 keV and fit. To calculate the luminosities, we use the distances of 20.0 Mpc for NGC 1399 (Blakeslee et al., 2001), 16.8 Mpc for NGC 4472 (Macri et al., 1999) and 16.5 Mpc for NGC 4649 (Blakeslee et al., 2009).

Table 3.2: Observations of NGC 4472, with raw source counts (0.5-8.0 keV) for GCU1, GCU2, GCU3 and GCU4. Observations marked with * were too off axis to measure counts from. Observations marked with - had the source off the chip.

ObsID	Date	ObsLen (ks)	GCU1 Cts	GCU2 Cts	GCU3 Cts	GCU4 Cts
322	2000-03-19	10.36	42	34	15	41
321	2000-06-12	39.59	134	142	178	196
8095	2008-02-23	5.09	31	11	11	21
11274	2010-02-27	39.67	458	115	196	180
12978	2010-11-20	19.78	12	-	2	*
12889	2011-02-14	135.59	1067	492	491	488
12888	2011-02-21	159.31	1559	506	644	641
16260	2014-08-04	24.74	6	*	*	50
16261	2015-02-24	22.76	58	42	*	*
16262	2016-04-30	24.73	136	50	89	52

3.2.2.1 NGC 4472 GC ULXs

There are five globular cluster ULX sources in NGC 4472 with $L_X > 10^{39}$ erg s^{-1}. The brightest of these, RZ2109 has been previously well studied in both X-ray and optical (Maccarone et al. 2007, Zepf et al. 2008, Shih et al. 2008, Steele et al. 2011, Dage et al. 2018). A second globular cluster ULX, CXOU 1229410+0757442, hereafter GCU1, has also been studied in some detail by Maccarone et al. (2011). There are three other GC ULXs, CXOU 1229345+08003209, (hereafter GCU2), CXOU 1229423+08000808 (hereafter GCU3), CXOU1229345+07585155 (hereafter GCU4), which have not yet been studied in depth (see Figure 3.1 for a *Chandra* image of the source locations.). At least 10 different *Chandra* observations exist for these sources spanning from the year 2000 to 2016 (see Table 3.2), enabling a study of their spectral properties and behaviour on the scale of years to decades. Below, we discuss the spectral fitting results for all sources.

CXOU 1229410+0757442 (GCU1)

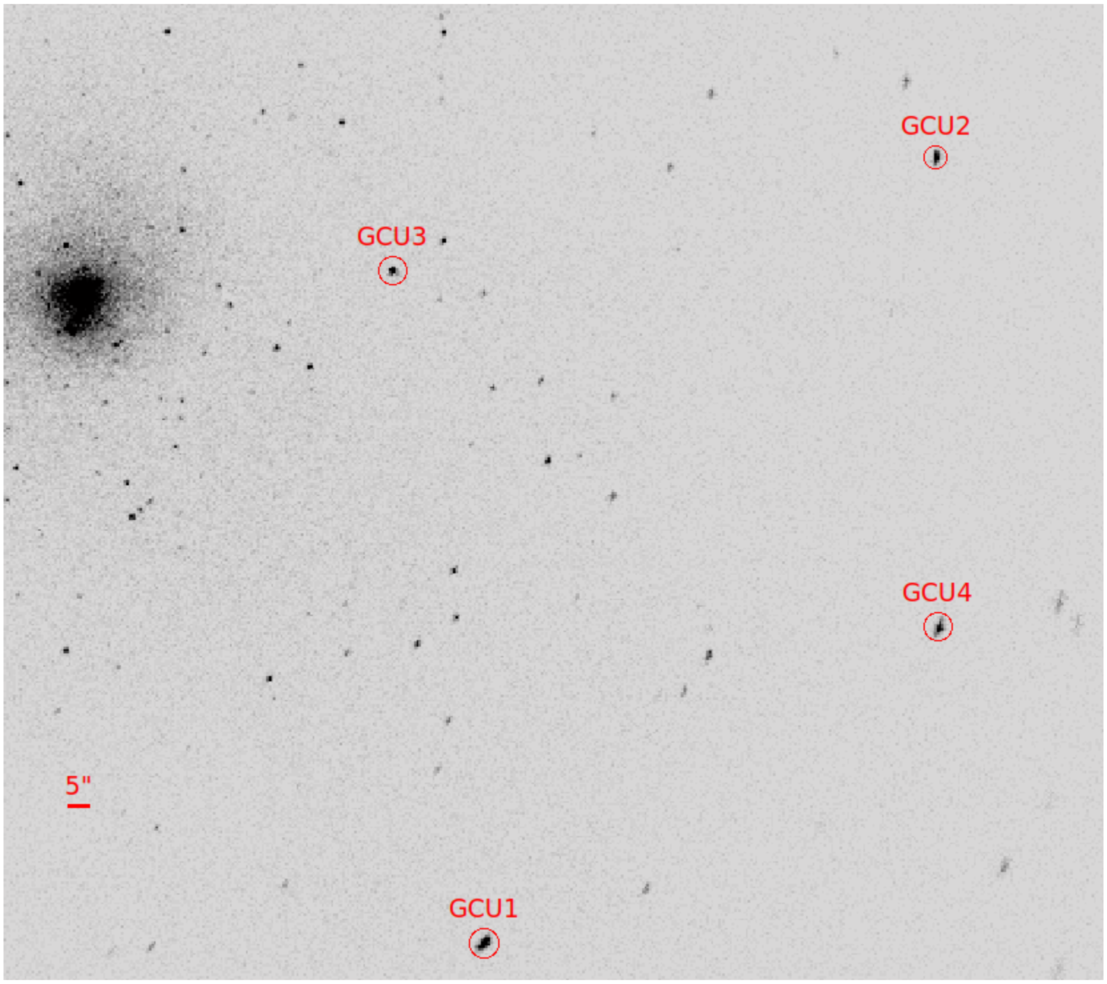

Figure 3.1: X-ray image of NGC 4472 (ObsID 12888, filtered to 0.5-8.0 keV) with regions for GCU1-GCU4 overlaid.

For GCU1, Maccarone et al. (2011) have previously examined earlier data through ObsID 11274, and could not find a statistical difference between an absorbed power law model versus an absorbed disk model, preferring the disk model for physical reasons. While the lower count spectra were ambiguous as to whether a single disk model is a better fit than a single power law model, χ^2 statistics for the deep observations (ObsIDs 12888 & 12889) indicate that the disk model alone is a much better fit than a single power law. Values for both models are presented in Tables 3.3, 3.5.

We fit a power law with a second absorbing column (`tbabs*tbabs*pegpwrlw`) to observations with greater than 100 source counts. We find that the nH is not inconsistent with zero in three of these observations. By comparison, fitting `tbabs*tbabs*diskbb` resulted in the second absorbing column consistent with zero that had significantly better χ^2 values in all cases.

We also find that adding a power law component to the single component disk is not a statistically significant improvement to the fit of GCU1. Specifically, we used XSPEC's F-test tool [5] which found no statistically significant improvement in the fit from adding the second component. We compare the statistics of the two component model to both single component models; these values are presented in Table 3.7. We note that while ObsID 11274 seems to favor a two component model, the best fit two-component power law photon index is 6.8, which is not typical for X-ray binaries. We do not report the best fit values for the two-component models as they are not physically realistic or statistically significant.

CXOU 1229345+08003209 (GCU2)

GCU2 had consistently better fit statistics for a single component disk model (Tables 3.3, 3.5). The F-test values (Table 3.7) again indicate that a single component disk model is the

---

[5] https://heasarc.gsfc.nasa.gov/xanadu/xspec/manual/node83.html

best fit for this source.

We rule out the necessity of a second absorbing column for GCU2 by again fitting `tbabs*tbabs*pegpwrlw` and `tbabs*tbabs*diskbb` to the source. Only ObsIDs 11274 and 12888 have a second absorption component for the power law model that is non-zero, however, the disk model,which has the best fit second absorbing column consistent with zero, has significantly better fit statistics than the intrinsically absorbed power law.

CXOU 1229423+08000808 (GCU3)

We fit a power law model to longer observations of GCU3 with a second absorbing column, but found the best fit absorption to be consistent with zero in all cases. We fit GCU3 with both single component models (as reported in Tables 3.3, 3.5), as well as a two component model. The statistics generally favour a single component disk fit, or are inconclusive. The two component model only showed a significant statistical improvement in one observation (Table 3.7), however, the best fit two-component power law for that had a very high index of 5.7, which again is unphysical and much steeper than the typical value for X-ray binaries.

CXOU1229345+07585155 (GCU4)

We found that the best fit value for the second absorbing column of this source was consistent with zero across all of the longer observations. GCU4 was statistically better fit by `tbabs*pegpwrlw` (Tables 3.3, 3.5). The F-test values generally do not favour a two component model (Table 3.7), except for ObsID 12889. However, it again has an unphysical power law of 5.0.

3.2.2.2 NGC 4649 GC ULXs

NGC 4649 hosts two GC ULXs, CXOUJ1243469+113234 (hereafter GCU5) (Roberts et al., 2012) and CXOU1243445+113150 (hereafter GCU6) (see Figure 3.2 for a *Chandra* image of

Table 3.3: *Chandra* Fit Parameters and Fluxes (0.5-8 keV) for spectral best fit single-component model `tbabs*diskbb` for GCU1 and GCU2 in NGC 4472. Hydrogen column density (N_H) frozen to 1.6 $\times 10^{20}$ cm^{-2}). Fit parameters marked with ** either encountered an XSPEC error when computing a lower bound, or had a lower bound consistent with zero, and are presented as an upper limit. Lower count observations fit with C-stat have their statistics presented in parentheses. All fluxes shown are unabsorbed.

	GCU1			
ObsID/Date	T_{in} keV	Disk Norm (10^{-4})	χ^2_ν/d.o.f. **or** (C-stat)	Disk Flux (10^{-14} erg cm^{-2} s^{-1})
322 (2000-03-19)	0.75 ($^{+0.33}_{-0.25}$)	$\leq$ 136.13**	(26.83/36)	2.9 ($^{+1.1}_{-0.8}$)
321 (2000-06-12)	0.98 ($^{+0.24}_{-0.20}$)	12.9 ($^{+15.9}_{-7.2}$)	1.51/5	2.3 ($\pm$0.5)
11274 (2010-02-27)	1.7 ($^{+0.33}_{-0.25}$)	7.7 ($^{+5.5}_{-3.4}$)	1.74/22	11.1 ($\pm$1.5)
12889 (2011-02-14)	1.13 ($\pm$0.10)	18.5 ($^{+6.5}_{-4.8}$)	1.25/49	5.8($\pm$0.5)
12888 (2011-02-21)	1.29 ($\pm$0.1)	14.1 ($^{+4.1}_{-3.2}$)	1.10/69	7.6($\pm$0.5)
16261 (2015-02-24)	0.87 ($^{+0.29}_{-0.19}$)	$\leq$ 64.01**	(41.04/51)	2.7($^{+0.7}_{-0.6}$)
16262 (2016-04-30)	0.98 ($^{+0.29}_{-0.22}$)	26.9($^{+34.0}_{-15.2}$)	0.55/5	4.9($\pm$0.9)
	GCU2			
ObsID/Date	T_{in} keV	Disk Norm (10^{-4})	χ^2_ν/d.o.f. **or** (C-stat)	Disk Flux (10^{-14} erg cm^{-2} s^{-1})
322 (2000-03-19)	1.29 ($^{+1.01}_{-0.42}$)	$\leq$ 24.2 **	(31.83/32)	3.2 ($^{+1.6}_{-1.1}$)
321 (2000-06-12)	1.36 ($^{+0.39}_{-0.29}$)	3.8 ($^{+4.4}_{-2.1}$)	0.70/6	2.5 ($\pm$0.6)
11274 (2010-02-27)	1.45 ($^{+0.56}_{-0.37}$)	$\leq$ 7.89**	1.35/5	2.5 ($\pm$0.7)
12889 (2011-02-14)	1.37 ($\pm$0.20)	4.5($^{+2.7}_{-1.7}$)	1.11/24	3.0($\pm$0.4)
12888 (2011-02-21)	1.16 ($\pm$0.17)	7.3 ($^{+4.7}_{-2.9}$)	1.36/24	2.6($\pm$0.3)
16261 (2015-02-24)	1.25 ($^{+0.78}_{-0.36}$)	$\leq$ 5.67**	(36.00/37)	2.1($^{+0.8}_{-0.6}$)
16262 (2016-04-30)	1.10 ($^{+0.63}_{-0.32}$)	$\leq$ 32.0**	(37.53/49)	2.40 ($^{+0.87}_{-0.63}$)

Table 3.4: *Chandra* Fit Parameters and Fluxes (0.5-8 keV) for spectral best fit single-component model `tbabs*diskbb` for GCU3 and GCU4 in NGC 4472. Hydrogen column density (N_H) frozen to 1.6 $\times 10^{20}$ cm^{-2}). Fit parameters marked with ** either encountered an XSPEC error when computing a lower bound, or had a lower bound consistent with zero, and are presented as an upper limit. Lower count observations fit with C-stat have their statistics presented in parentheses. All fluxes shown are unabsorbed.

	GCU3			
ObsID/Date	T_{in} (keV)	Disk Norm (10^{-4})	χ^2_ν/d.o.f. **or** (C-stat)	Disk Flux (10^{-14} erg cm^{-2} s $^{-1}$)
321 (2000-06-12)	1.41 ($^{+0.40}_{-0.30}$)	4.1 ($^{+4.7}_{-2.3}$)	0.43/8	3.2 ($\pm$0.7)
11274(2010-02-27)	1.19 ($^{+0.26}_{-0.20}$)	9.5($^{+8.3}_{-4.7}$)	1.36/8	3.6($\pm$0.6)
12889 (2011-02-14)	1.39 ($^{+0.25}_{-0.20}$)	3.9 ($^{+2.8}_{-1.7}$)	0.95/23	2.9 ($\pm$0.4)
12888 (2011-02-21)	1.31 ($\pm$0.15)	5.4($^{+2.6}_{-1.8}$)	0.92/30	3.1($\pm$0.3)
16262 (2016-04-30)	1.27 ($^{+0.62}_{-0.32}$)	$\leq$ 20.9**	(78.08/77)	3.6($^{+1.1}_{-0.8}$)

	GCU4			
ObsID/Date	T_{in} (keV)	Disk Norm (10^{-4})	χ^2_ν/d.o.f. **or** (C-stat)	Disk Flux (10^{-14} erg cm^{-2} s $^{-1}$)
322 (2000-03-19)	1.20 ($^{+0.90}_{-0.42}$)	10.6 ($^{+21.8}_{-10.6}$)	(30.64/38)	4.2 ($^{+2.0}_{-1.3}$)
321 (2000-06-12)	0.98 ($^{+0.38}_{-0.24}$)	20.9 ($^{+35.9}_{-14.0}$)	1.32/7	3.7 ($^{+1.0}_{-0.8}$)
8095 (2008-02-23)	1.2 ($^{+1.9}_{-0.5}$)	$\leq$ 10.6**	(24.54/22)	3.0 ($^{+2.4}_{-1.3}$)
11274 (2010-02-27)	1.52 ($^{+0.63}_{-0.39}$)	3.7 ($^{+0.6}_{-0.3}$)	1.69/7	3.8 ($\pm$ 0.9)
12889 (2011-02-14)	1.28 ($^{+0.22}_{-0.18}$)	5.9 ($^{+4.0}_{-2.5}$)	1.48/25	3.0 ($\pm$ 0.4)
12888 (2011-02-21)	1.39 ($^{+0.25}_{-0.19}$)	4.7 ($^{+3.3}_{-2.0}$)	1.82/33	3.3 ($\pm$ 0.4)
16260 (2014-08-04)	1.4 ($^{+1.2}_{-0.5}$)	2.7 ($^{+7.9}_{-2.7}$)	(43.73/48)	2.2 ($^{+1.0}_{-0.6}$)
16261 (2015-02-24)	1.46($^{+0.88}_{-0.42}$)	$\leq$ 13.8**	(44.97/58)	3.6 ($^{+1.2}_{-0.9}$)
16262 (2016-04-30)	1.5 ($^{+1.2}_{-0.5}$)	$\leq$ 15.5**	(48.94/50)	3.0 ($^{+1.3}_{-0.9}$)

Table 3.5: *Chandra* Fit Parameters and Fluxes (0.5-8 keV) for spectral best fit single-component model `tbabs*pegpwrlw` for GCU1 and GCU2 in NGC 4472. Hydrogen column density (N_H) frozen to 1.6 $\times 10^{20}$ cm^{-2}). Fit parameters marked with ** either encountered an XSPEC error when computing a lower bound, or had a lower bound consistent with zero, and are presented as an upper limit. Lower count observations fit with C-stat have their statistics presented in parentheses. All fluxes shown are unabsorbed.

	GCU1		
ObsID/Date	Γ	χ^2_ν/d.o.f. **or** (C-stat)	PL Flux (10^{-14} erg cm^{-2} s $^{-1}$)
322 (2000-03-19)	1.7 (± 0.5)	(22.74/36)	4.5 ($^{+2.5}_{-1.5}$)
321 (2000-06-12)	1.7 (± 0.2)	3.41/5	2.6 (± 0.6)
11274 (2010-02-27)	1.3 (± 0.1)	1.77/22	12.8 (± 1.4)
12889 (2011-02-14)	1.6 (± 0.10)	2.25/49	6.8 (± 0.5)
12888 (2011-02-21)	1.5 (± 0.1)	1.71/69	8.8 (± 0.5)
16261 (2015-02-24)	2.0 (± 0.4)	(47.61/51)	3.3 ($^{+0.9}_{-0.7}$)
16262 (2016-04-30)	1.8 (±0.3)	0.73/5	5.9 (± 1.0)
	GCU2		
ObsID/Date	Γ	χ^2_ν/d.o.f. **or** (C-stat)	PL Flux (10^{-14} erg cm^{-2} s $^{-1}$)
322 (2000-03-19)	1.4 (±0.5)	(35.31/32)	3.9 ($^{+1.9}_{-1.3}$)
321 (2000-06-12)	1.3 (± 0.2)	3.11/6	3.0 (± 0.7)
11274 (2010-02-27)	1.4 (± 0.3)	3.27/5	2.9 (± 0.7)
12889 (2011-02-14)	1.4 (± 0.1)	9.29/24	3.5 (± 0.4)
12888 (2011-02-21)	1.6 (± 0.1)	965459.3/24	3.2 (± 0.3)
16261 (2015-02-24)	1.6 (± 0.5)	(38.69/37)	2.5 ($^{+0.9}_{-0.7}$)
16262 (2016-04-30)	1.9 (± 0.5)	(36.02/49)	2.91 ($^{+0.91}_{-0.72}$)

Table 3.6: *Chandra* Fit Parameters and Fluxes (0.5-8 keV) for spectral best fit single-component model `tbabs*pegpwrlw` for GCU3 and GCU4 in NGC 4472. Hydrogen column density (N_H) frozen to 1.6 $\times 10^{20}$ cm^{-2}). Fit parameters marked with ** either encountered an XSPEC error when computing a lower bound, or had a lower bound consistent with zero, and are presented as an upper limit. Lower count observations fit with C-stat have their statistics presented in parentheses. All fluxes shown are unabsorbed.

	GCU3		
ObsID/Date	Γ	χ^2_ν/d.o.f. **or** (C-stat)	PL Flux (10^{-14} erg cm^{-2} s $^{-1}$)
321 (2000-06-12)	1.3 ($\pm$0.2)	0.75/8	3.7 ($\pm$ 0.7)
11274(2010-02-27)	1.4 ($\pm$ 0.2)	2.56/8	4.5 ($^{+0.8}_{-0.7}$)
12889 (2011-02-14)	1.4 ($\pm$0.1)	0.90/23	3.3 ($\pm$ 0.4)
12888 (2011-02-21)	1.5 ($\pm$1.0)	1.64/30	3.6 ($\pm$ 0.3)
16262 (2016-04-30)	1.5 ($\pm$ 0.4)	(81.63/77)	4.4 ($^{+1.3}_{-1.0}$)

	GCU4		
ObsID/Date	Γ	χ^2_ν/d.o.f. **or** (C-stat)	PL Flux (10^{-14} erg cm^{-2} s $^{-1}$)
322 (2000-03-19)	1.9($\pm$0.5)	(220.21/38)	4.3 ($^{+1.7}_{-1.2}$)
321 (2000-06-12)	1.6 ($\pm$0.2)	0.64/7	5.3 ($\pm$0.9)
8095 (2008-02-23)	1.4 ($\pm$0.6)	(25.54/22)	3.8 ($^{+2.6}_{-1.6}$)
11274 (2010-02-27)	1.5 ($\pm$0.2)	0.82/7	4.4($\pm$0.9)
12889 (2011-02-14)	1.5 ($\pm$0.1)	1.42/25	3.63$\pm$0.4)
12888 (2011-02-21)	1.5 ($\pm$0.1)	1.20/33	4.0 ($\pm$0.4)
16260 (2014-08-04)	1.5 ($\pm$0.4)	(41.84/48)	2.5($^{+0.9}_{-0.69}$)
16261 (2015-02-24)	1.5 ($\pm$0.5)	(43.75/58)	4.1($^{+1.2}_{-0.9}$)
16262 (2016-04-30)	1.5 ($\pm$0.4)	(48.88/50)	3.5($^{+1.2}_{-0.9}$)

Table 3.7: F-test probability values for single component versus two component models for GC ULXs in NGC 4472 with over 100 source counts. We compare statistics between `tbabs*(diskbb+pegpwrlw)` and `tbabs*diskbb` only in columns titled "Disk", and `tbabs*(diskbb+pegpwrlw)` with `tbabs*pegpwrlw` only in columns titled "PL". Blank table entries are where the source had fewer than 100 counts in a given observation.

	GCU1		GCU2		GCU3		GCU4	
ObsID	Disk	PL	Disk	PL	Disk	PL	Disk	PL
321	1	0.31	1	0.06	0.01	0.99	0.15	0.99
11274	0.07	0.06						
12889	0.18	5.65e-8	0.10	0.17	2.31e-3	4.07e-3	0.06	0.01
12888	0.14	1.37e-7	0.36	5.83e-4	0.10	6.01e-6	1.35e-3	1

Table 3.8: Chandra Observations of NGC 4649, with raw source counts (0.5-8.0 keV) for GCU5 and GCU6.

ObsID	Date	ObsLen (ks)	GCU5 Cts	GCU6 Cts
785	2000-04-20	38.11	65	135
8182	2007-01-30	52.37	468	196
8507	2007-02-01	17.52	111	45
12976	2011-02-24	101.04	773	265
12975	2011-08-08	84.93	505	260
14328	2011-08-12	13.97	84	39

the source locations.). **CXOUJ1243469+113234 (GCU5)**

As noted in Roberts et al. (2012), GCU5 shows better fit statistics for the single power law component. ObsID 12975 is an exception here; the single disk component had much better fit statistics than the single power law. However, Roberts et al. (2012) found that this observation had a second intrinsic absorbing column that was significant. We do not account for such a component here, but it could explain why in this particular instance, a disk was a better fit than a single power law, when a power law has typically a better fit than a disk in previous observations. The F-test values for comparison between a single component model and a two component model are listed in Tables 3.9, 3.10 and the best fit values for either single component models are listed in Tables 3.12,3.13.

CXOU1243445+113150 (GCU6)

GCU6 is ambiguous as to whether a single disk model or a single power law model is a better fit. See Tables 3.9, 3.10 for a comparison of the single disk versus power law model.The F-test values for GCU6 (Table 3.11) indicate that the two component model is not a better fit to the data. We find that this source has a significant (non-zero) second absorbing column for ObsIDs 8182 and 12975. When comparing these observations to a disk model with a

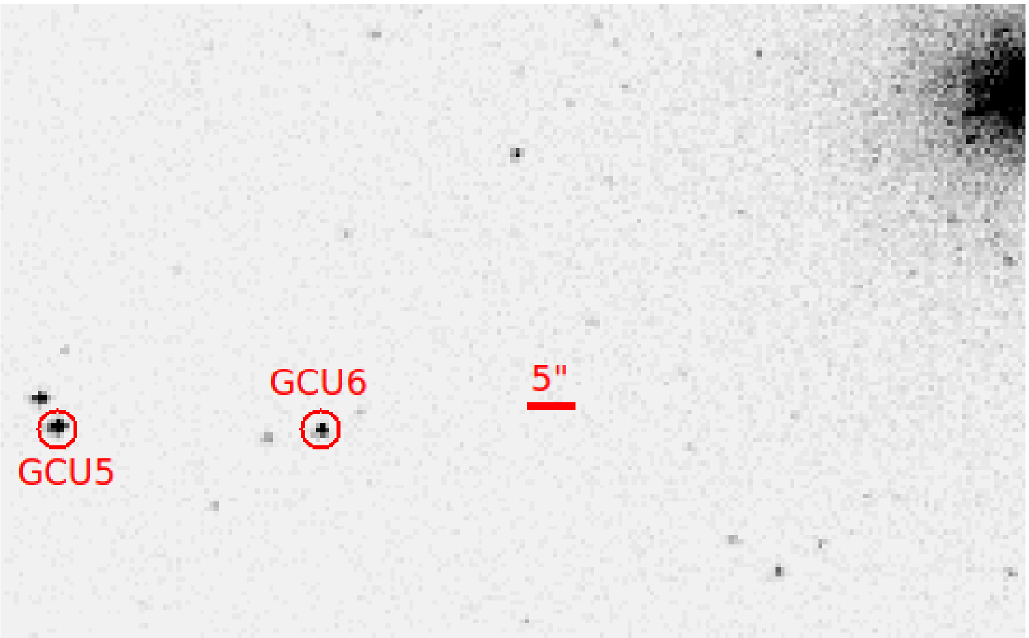

Figure 3.2: X-ray image of NGC 4649 (ObsID 12976, filtered to 0.5-8.0 keV) with regions for GCU5 & GCU6 overlaid.

best fit second absorbing column that is consistent with zero, we find that it is statistically ambiguous as to which model is a better fit. We present these fits in Table 3.12.

3.2.2.3 NGC 1399 GC ULXs

NGC 1399 hosts three GC ULXs. One, CXOKMZJ033831.7−353058 (Shih et al., 2010) has faded beyond detection by 2005, and we do not study it here. CXOJ0338318-352604, (hereafter GCU7) has been previously studied by Irwin et al. (2010), while the third, CXOU0338326-35270567 (hereafter GCU8) is bright but has not been previously extensively studied in X-ray. We present new analysis on both old and new data (Table 3.14). see Figure 3.3 for a *Chandra* image of the source locations and any nearby sources.

CXOJ0338318-352604 (GCU7)

GCU7 shows better fit statistics for the single component disk model (Table 3.16). The F-test values indicate that the two component model is not necessary, except perhaps for ObsID

Table 3.9: *Chandra* Fit Parameters and Fluxes (0.5-8 keV) for spectral best fit single-component model `tbabs*diskbb` of of GC ULXs in NGC 4649. (Hydrogen column density (N_H) frozen to 2.0 $\times 10^{20}$ cm^{-2}). Fit parameters marked with ** either encountered an XSPEC error when computing a lower bound, or had a lower bound consistent with zero, and are presented as an upper limit. Lower count observations fit with C-stat have their statistics presented in parentheses. All fluxes shown are unabsorbed.

	GCU5			
ObsID/Date	T_{in} (keV)	Disk Norm (10^{-4})	χ^2_ν/d.o.f. **or** (C-stat)	Disk Flux (10^{-14} erg cm^{-2} s $^{-1}$)
785 (2000-04-20)	1.08 ($^{+0.60}_{-0.30}$)	$\leq$ 12.5**	(65.99/59)	1.1 ($^{+0.5}_{-0.3}$)
8182 (2007-01-30)	2.02($^{+0.50}_{-0.36}$)	2.9($^{2.5}_{-1.5}$)	1.68/21	8.6 ($\pm$1.2)
8507 (2007-02-01)	1.27 ($^{+0.45}_{-0.31}$)	9.2($^{+14.4}_{-5.9}$)	2.00/4	4.6($\pm$1.1)
12976 (2011-02-24)	1.09 ($\pm$0.13)	19.4($^{+9.9}_{-6.6}$)	1.93/36	5.3 ($\pm$0.5)
12975 (2011-08-08)	2.18 ($^{+0.54}_{-0.37}$)	1.6 ($^{+1.3}_{-0.8}$)	0.74/23	6.2($\pm$0.8)
14328 (2011-08-12)	2.1 ($^{+2.1}_{-0.7}$)	$\leq$ 7.20**	(49.51/76)	6.4($^{+2.3}_{-1.7}$)

	GCU6			
ObsID/Date	T_{in} (keV)	Disk Norm (10^{-4})	χ^2_ν/d.o.f. **or** (C-stat)	Disk Flux (10^{-14} erg cm^{-2} s $^{-1}$)
785 (2000-04-20)	1.32 ($^{+0.94}_{-0.43}$)	$\leq$ 10.3**	1.71/5	2.3 ($^{+1.1}_{-0.7}$)
8182 (2007-01-30)	1.28($^{+0.34}_{-0.25}$)	5.5 ($^{6.2}_{-3.1}$)	0.95/8	2.9 ($\pm$0.6)
8507 (2007-02-01)	1.5	1.27 ($^{+0.92}_{-0.41}$)	$\leq$ 13.6**	(43.23/44)
2.0 ($^{+0.9}_{-0.6}$)				
12976 (2011-02-24)	1.12 ($^{+0.31}_{-0.23}$)	5.7 ($^{+7.2}_{-3.3}$)	2.04/12	5.3($\pm$0.3)
12975 (2011-08-08)	2.15 ($^{+0.90}_{-0.51}$)	0.9 ($^{+1.2}_{-0.6}$)	1.67/12	3.2($\pm$0.6)
14328 (2011-08-12)	0.65 ($^{+0.32}_{-0.15}$)	$\leq$ 64.5**	(31.03/37)	1.6 ($^{+0.6}_{-0.4}$)

Table 3.10: *Chandra* Fit Parameters and Fluxes (0.5-8 keV) for spectral best fit single-component model `tbabs*pegpwrlw` of of GC ULXs in NGC 4649. (Hydrogen column density (N_H) frozen to 2.0 $\times 10^{20}$ cm^{-2}). Fit parameters marked with ** either encountered an XSPEC error when computing a lower bound, or had a lower bound consistent with zero, and are presented as an upper limit. Lower count observations fit with C-stat have their statistics presented in parentheses. All fluxes shown are unabsorbed.

		GCU5	
ObsID/Date	Γ	χ^2_ν/d.o.f. **or** (C-stat)	PL Flux (10^{-14} erg cm^{-2} s $^{-1}$)
785 (2000-04-20)	1.6 ($\pm$0.3)	(61.54/59)	1.3 ($^{+0.5}_{-0.4}$)
8182 (2007-01-30)	1.2 ($\pm$ 0.1)	1.47/21	9.3 ($\pm$ 1.1)
8507 (2007-02-01)	1.5 ($\pm$ 0.3)	2.52/4	5.3 ($^{+1.3}_{-1.2}$)
12976 (2011-02-24)	1.6 ($\pm$ 0.1)	1.50/36	6.2 ($\pm$ 0.6)
12975 (2011-08-08)	1.1 ($\pm$ 0.1)	1.20/23	7.0 ($\pm$ 0.7)
14328 (2011-08-12)	1.2 ($\pm$ 0.3)	(48.53/77)	7.02($^{+2.05}_{-1.60}$)
		GCU6	
ObsID/Date	Γ	χ^2_ν/d.o.f. **or** (C-stat)	PL Flux (10^{-14} erg cm^{-2} s $^{-1}$)
785 (2000-04-20)	1.3 ($\pm$0.2)	0.95/5	3.2 ($^{+0.9}_{-0.8}$)
8182 (2007-01-30)	1.3 ($\pm$ 0.2)	1.41/8	3.7 ($\pm$ 0.6)
8507 (2007-02-01)	1.5 ($\pm$ 0.4)	(35.81/43)	2.4($^{+1.1}_{-0.7}$)
12976 (2011-02-24)	1.6 ($\pm$ 0.2)	1.34/12	2.2 ($\pm$ 0.3)
12975 (2011-08-08)	1.1 ($\pm$ 0.2)	1.96/12	3.6 ($\pm$0.5)
14328 (2011-08-12)	2.0 ($\pm$ 0.5)	(27.63/37)	2.1 ($\pm$ 0.2)

Table 3.11: F-test probability values for single component versus two component models for GC ULXs in NGC 4649 with over 100 source counts. We compare statistics between `tbabs*(diskbb+pegpwrlw)` and `tbabs*diskbb` only in columns titled "Disk", and `tbabs*(diskbb+pegpwrlw)` with `tbabs*pegpwrlw` only in columns titled "PL".

	GCU5		GCU6	
ObsID	Disk	PL	Disk	PL
785	-	-	0.33	0.80
8182	0.09	0.31	0.65	0.20
12976	2.72 $\times 10^{-3}$	0.19	0.12	1
12975	0.99	6.41 $\times 10^{-3}$	1	0.47

Table 3.12: *Chandra* Fit Parameters and Fluxes (0.5-8.0 keV) for spectral best fit values of GCU6 in NGC 4649 for `tbabs*tbabs*pegpwrlw` where N_H was not consistent with zero. All fluxes shown are unabsorbed.

ObsID/Date	N_H (10^{20} cm^{-2})	Γ	PL χ^2_ν/d.o.f.	PL Flux (10^{-14} erg cm^{-2} s $^{-1}$)
8182 (2007-01-30)	$0.17\ ^{+0.17}_{-0.13}$	1.8 (± 0.4)	0.84/7	3.7 (± 0.6)
12975 (2011-08-08)	$0.25^{+0.25}_{-0.23}$	1.5 (± 0.4)	1.85/11	3.7 (±0.5)

Table 3.13: χ^2/d.o.f. for `tbabs*tbabs*diskbb`,where the best fit N_H was consistent with zero. (Hydrogen column density (N_H) frozen to 2.2 $\times 10^{20}$ cm^{-2}.

ObsID/Date	Disk χ^2_ν/d.o.f.
8182 (2007-01-30)	1.1/7
12975 (2011-08-08)	1.82/11

Table 3.14: Chandra Observations of NGC 1399, with raw source counts (0.5-8.0 keV) for GCU7 and GCU8.

ObsID	Date	ObsLen (ks)	GCU7 Cts	GCU8 Cts
320	1999-10-18	3.38	12	23
319	2000-01-18	56.04	448	629
239	2000-01-19	3.60	14	22
240	2000-06-16	43.53	12	44
2389	2001-05-08	14.67	13	10
4172	2003-05-26	44.50	114	294
9530	2008-06-08	59.35	248	366
14527	2013-07-01	27.79	136	230
16639	2014-10-12	29.67	171	162
14529	2015-11-06	31.62	132	226

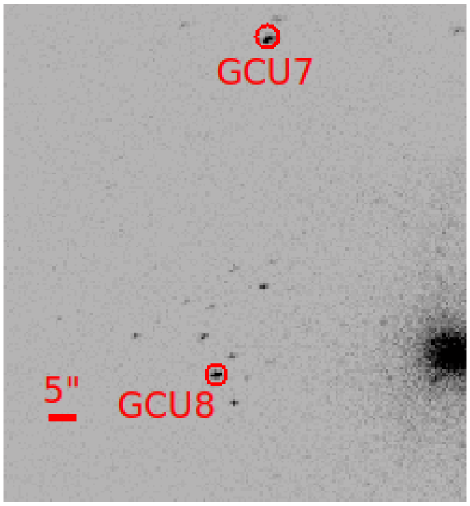

Figure 3.3: X-ray image of NGC 1399 (ObsID 319, filtered to 0.5-8.0 keV) with regions for GCU7 & GCU8 overlaid.

319 (Table 3.17). However, the two component model has a best fit power law index of 5.7. Fitting this source with a second absorption component plus power law gives an absorption that is consistent with zero in almost all cases, and for all fits of `tbabs*tbabs*pegpwrlw`, the power law index is between 3-4, which implies that the spectrum is very soft and unlikely to be fit by a power law model of any sort.

Clausen et al. (2012a) model this system as the tidal disruption of a horizontal giant branch star by an intermediate mass black hole, while Maccarone & Warner (2011) model this as a R Corona Borealis star illuminated by a bright X-ray source. Neither scenario is ruled out by the observed shallow decline of the L_X. Other binary system models might also be consistent with these data.

CXOU0338326-35270567 (GCU8)

We find that there is no evidence for a second absorbing column of any sort for this source.The F-test values for GCU8 rule out a two component model (Table 3.17), and the statistics indicate that a single power law component is the best fit model for this source. (Tables 3.15, 3.16). Note that the best fit values of the disk norms for GCU8 are upper limits, even in the higher count observations binned by 20 and fit with χ^2 statistics, most likely because the single disk fit for this source was not a good fit to the point where XSPEC had difficulty fitting the normalisations to these spectra.

GCU8 was marginally detected in ObsID 2389. We used the WebPIMMS tool to estimate an upper limit on the unabsorbed flux using a count rate of 6.8×10^{-4} ct/s, and a fixed powerlaw index of 1.7, with the N_H fixed to frozen to $1.34\ \times10^{20}$ cm^{-2} .

3.2.3 Long and Short-term X-ray Variability

RZ2109 has been shown to vary both long and short term (see Maccarone et al. 2007; Shih et al. 2010; Dage et al. 2018, for example), which is leading evidence for its compact object being a black hole accretor. Other GC ULXs show some significant long-term variability, and quantifying the variability of these sources on either long or short timescales can shed light on the nature of the objects that make up these ULX systems.

3.2.3.1 Long-Term Variability

We found the average luminosity comparing the data to a range of 5000 luminosities drawn from the lowest L_X to the highest for the source and computing the reduced χ^2 in each case. We plot the luminosity with the χ^2 closest to 1.0 as the mean luminosity. This is plotted for all the sources in Figure 3.4.

To quantify the variability of these sources, we do a χ^2 minimisation fit of the data using SCIPY[8] with a model of constant luminosity, using the best fit luminosity from above as the mean value. We find that GCU2, GCU3, GCU4 and GCU6 have χ^2 values less than 1 (e.g., no evidence for long-term variability), while GCU1, GCU5, GCU6 and GCU7 have very

---

[8] https://docs.scipy.org/doc/scipy/reference/generated/scipy.stats.chisquare.html

Table 3.15: *Chandra* Fit Parameters and Fluxes (0.5-8 keV) for spectral best fit single-component model `tbabs*diskbb` of GC ULXs in NGC 1399. Hydrogen column density (N_H) frozen to 1.34 $\times 10^{20}$ cm^{-2}). Fit parameters marked with ** either encountered an XSPEC error when computing a lower bound, or had a lower bound consistent with zero, and are presented as an upper limit. Lower count observations fit with C-stat have their statistics presented in parentheses. All fluxes shown are unabsorbed.

	GCU7			
ObsID/Date	T_{in} (keV)	Disk Norm (10^{-4})	χ^2_ν/d.o.f. **or** (C-stat)	Disk Flux (10^{-14} erg cm^{-2} s $^{-1}$)
320 (1999-10-18)	$0.28\ (^{+0.19}_{-0.09})$	$\leq 46.8^{**}$	(8.50/12)	$4.8\ (^{+4.0}_{-3.2})$
319 (2000-01-18)	$0.39\ (\pm 0.04)$	$7.3\ (^{+3.5}_{-2.4})$	1.70/24	$2.5(^{+0.2}_{-0.3})$
239 (2000-01-19)	$0.27\ (^{+0.18}_{-0.10})$	$\leq 288.4^{**}$	(12.36/13)	$2.3\ (^{+1.3}_{-1.0})$
240 (2000-06-16)	$0.52\ (^{+0.29}_{-0.18})$	$1.3\ (^{+1.6}_{-0.7})$	(22.28/17)	$1.5(^{+0.8}_{-6.2})$
2389 (2001-05-08)	$0.21\ (^{+0.07}_{-0.11})$	$\leq 1272^{**}$	(8.94/12)	$4.3(^{+2.5}_{-1.8})$
4172 (2003-05-26)	$0.36\ (^{+0.08}_{-0.06})$	$7.7(^{+11.9}_{-4.7})$	0.96/5	$1.7(\pm 0.3)$
9530 (2008-06-08)	$0.34\ (\pm 0.04)$	$11.9(^{+8.2}_{-5.0})$	1.25/12	$2.0(\pm 0.2)$
14527 (2013-07-01)	$0.39\ (^{+0.08}_{-0.06})$	$7.9(^{+9.2}_{-4.4})$	0.98/6	$2.7(\pm 0.4)$
16639 (2014-10-12)	$0.43\ (\pm 0.07)$	$6.6(^{+7.1}_{-3.3})$	0.94/7	$3.4(\pm 0.5)$
14529 (2015-11-06)	$0.35\ (\pm 0.07)$	$14.2(^{+21.3}_{-8.5})$	1.65/5	$2.7(\pm 0.4)$

	GCU8			
ObsID/Date	T_{in} (keV)	Disk Norm (10^{-4})	χ^2_ν/d.o.f. **or** (C-stat)	Disk Flux (10^{-14} erg cm^{-2} s $^{-1}$)
320 (1999-10-18)	≤ 1.8	$\leq 4.09^{**}$	(19.54/18)	$7.8\ (^{+9.2}_{-3.9})$
319 (2000-01-18)	$1.27(^{+0.21}_{-0.17})$	$13.5\ (^{+5.2}_{-8.2})$	1.84/31	$6.7\ (\pm 0.9)$
240 (2000-06-16)	$1.8\ (^{+1.3}_{-0.5})$	$\leq 3.14^{**}$	(53.01/48)	$5.5(^{+1.7}_{-1.3})$
2389 (2001-05-08)	-	-	-	≤ 0.5 [6]
4172 (2003-05-26)	$2.6\ (^{+2.0}_{-0.8})$	$\leq 3.78^{**}$	1.74/12	$8.7\ (^{+1.8}_{-1.5})$
9530 (2008-06-08)	$1.28\ (\pm 0.30)$	$8.7\ (^{+8.3}_{-4.4})$	1.25/16	$4.5\ (\pm 0.8)$
14527 (2013-07-01)	$1.36(^{+0.47}_{-0.29})$	$11.0\ (^{+14.1}_{-6.9})$	0.28/9	$7.2\ (^{+1.6}_{-1.3})$
16639 (2014-10-12)	$2.0(^{+2.9}_{-0.7})$	$\leq 9.09^{**}$	0.96/6	$6.3\ (^{+2.7}_{-1.7})$
14529 (2015-11-06)	$2.0(^{+1.2}_{-0.5})$	$\leq 9.46^{**}$	0.67/9	$8.4\ (^{+2.2}_{-1.8})$

Table 3.16: *Chandra* Fit Parameters and Fluxes (0.5-8 keV) for spectral best fit single-component model `tbabs*pegpwrlw` of GC ULXs in NGC 1399. Hydrogen column density (N_H) frozen to 1.34 $\times 10^{20}$ cm^{-2}). Fit parameters marked with ** either encountered an XSPEC error when computing a lower bound, or had a lower bound consistent with zero, and are presented as an upper limit. Lower count observations fit with C-stat have their statistics presented in parentheses. All fluxes shown are unabsorbed.

	GCU7		
ObsID/Date	Γ	χ^2_ν/d.o.f. **or** (C-stat)	PL Flux (10^{-14} erg cm^{-2} s $^{-1}$)
320 (1999-10-18)	3.1 ($^{+1.0}_{-0.9}$)	(10.91/12)	2.1 ($^{+1.5}_{-1.0}$)
319 (2000-01-18)	2.4 (± 0.1)	8.32/24	2.9 (± 0.3)
239 (2000-01-19)	3.1 ($^{+1.1}_{-0.9}$)	(14.53/13)	2.5 ($^{+1.7}_{-1.1}$)
240 (2000-06-16)	2.7 ($^{+0.8}_{-0.7}$)	(24.99/17)	1.6($^{+0.9}_{-0.7}$)
2389 (2001-05-08)	3.8 ($^{+1.1}_{-1.0}$)	(10.30/12)	4.1 ($^{+2.4}_{-1.8}$)
4172 (2003-05-26)	2.9 (±0.3)	0.76/5	2.1 (± 0.3)
9530 (2008-06-08)	2.6 (± 0.2)	2.64/12	2.4 (± 0.3)
14527 (2013-07-01)	2.7 (± 0.3)	3.71/6	3.2 (±0.5)
16639 (2014-10-12)	2.7 (±0.2)	1.99/7	4.0 (± 0.6)
14529 (2015-11-06)	3.0 (±0.3)	3.23/5	3.2 (±0.5)

	GCU8		
ObsID/Date	Γ	χ^2_ν/d.o.f. **or** (C-stat)	PL Flux (10^{-14} erg cm^{-2} s $^{-1}$)
320 (1999-10-18)	1.3 (±0.7)	(18.87/20)	8.8 ($^{+1.7}_{-3.9}$)
319 (2000-01-18)	1.4 (±0.1)	1.37/31	8.3 (±0.9)
240 (2000-06-16)	1.5 (±0.5)	(51.46/48)	5.9 (± 1.7)
2389 (2001-05-08)	-	-	$\leq$ 0.5 [7]
4172 (2003-05-26)	1.1 (±0.2)	1.24/12	9.5(±1.4)
9530 (2008-06-08)	1.5 (±0.2)	0.66/16	5.6(±0.7)
14527 (2013-07-01)	1.3 (±0.2)	0.42/9	9.7(±1.7)
16639 (2014-10-12)	1.1 (±0.3)	0.78/6	8.0$^{+1.9}_{-1.7}$)
14529 (2015-11-06)	1.2 (±0.2)	0.52/9	10.2($^{+1.9}_{-1.7}$)

Table 3.17: F-test probability values for single component versus two component models for GC ULXs in NGC 1399 with over 100 source counts. We compare statistics between `tbabs*(diskbb+pegpwrlw)` and `tbabs*diskbb` only in columns titled “Disk”, and `tbabs*(diskbb+pegpwrlw)` with `tbabs*pegpwrlw` only in columns titled “PL”.

	GCU7		GCU8	
ObsID	Disk	PL	Disk	PL
319	0.08	7.63×10^{-4}	6.14×10^{-3}	0.44
4172	0.22	0.46	0.19	1
9530	0.56	0.04	0.01	1
14527	0.54	0.11	0.51	0.12
16639	0.11	0.03	0.65	1
14529	0.54	0.37	0.42	0.99

Table 3.18: χ^2 values comparing a model of constant luminosity to the luminosity of the GC ULXs in this sample over time.

Source	GCU1	GCU2	GCU3	GCU4	GCU5	GCU6	GCU7	GCU8
χ^2	26.33	0.22	0.17	0.55	3.00	0.30	5.22	4.12

large χ^2 values, indicating that they are much more variable. These values are presented in Table 3.18.

3.2.3.2 Short-term (inter-observational) variability

Two GC ULXs (Maccarone et al., 2007; Shih et al., 2010) show variability on short time scales. We extracted light curves of GC ULXs from our sample in any observations that had 500 source counts or greater (see Tables 3.2, 3.8, and 3.14). The source GCU1 shows interesting behaviour in ObsIDs 12888 and 12889. These observations were taken a week apart, and were each near 150ks in length. The fluxes in each observation were significantly different (see Tables 3.3, 3.5), and yet within the observation, no clear variability was observed.

We also search for inter-observational variability or periodicities in any *Chandra* light curves with greater than 500 source counts (See Tables 3.2, 3.8, 3.14). We implement a generalized Lomb-Scargle periodogram algorithm [9] (Lomb, 1976; Scargle, 1982) on combined

---

[9] `http://www.astroml.org/modules/generated/astroML.time_series.lomb_scargle.html`

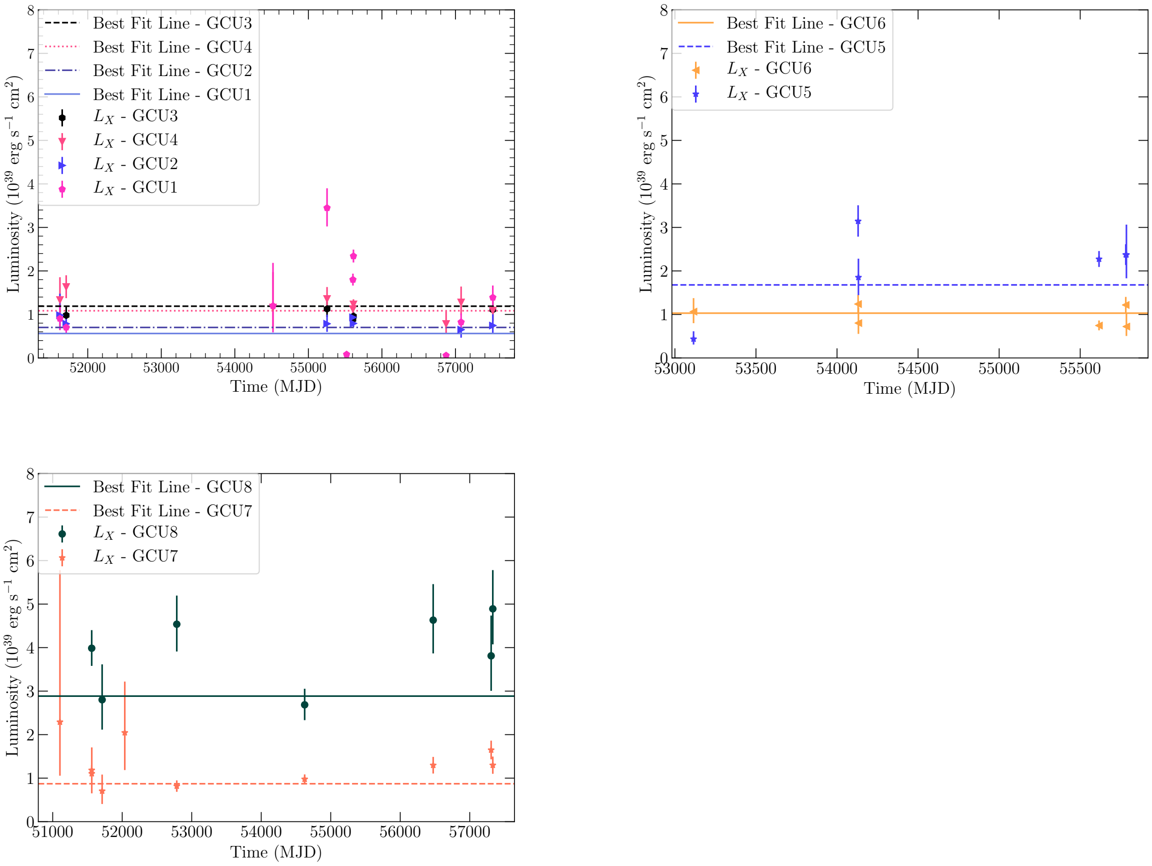

Figure 3.4: Upper: L_X vs. time for NGC 4472 GC ULXs with mean luminosity (data from Tables 3.3, 3.4,3.5, 3.6). Middle: L_X vs. time for NGC 4649 GC ULXs with mean luminosity (data from Tables 3.9,3.10). Lower: L_X vs. time for NGC 1399 GC ULXs with mean luminosity (data from Tables 3.15,3.16).

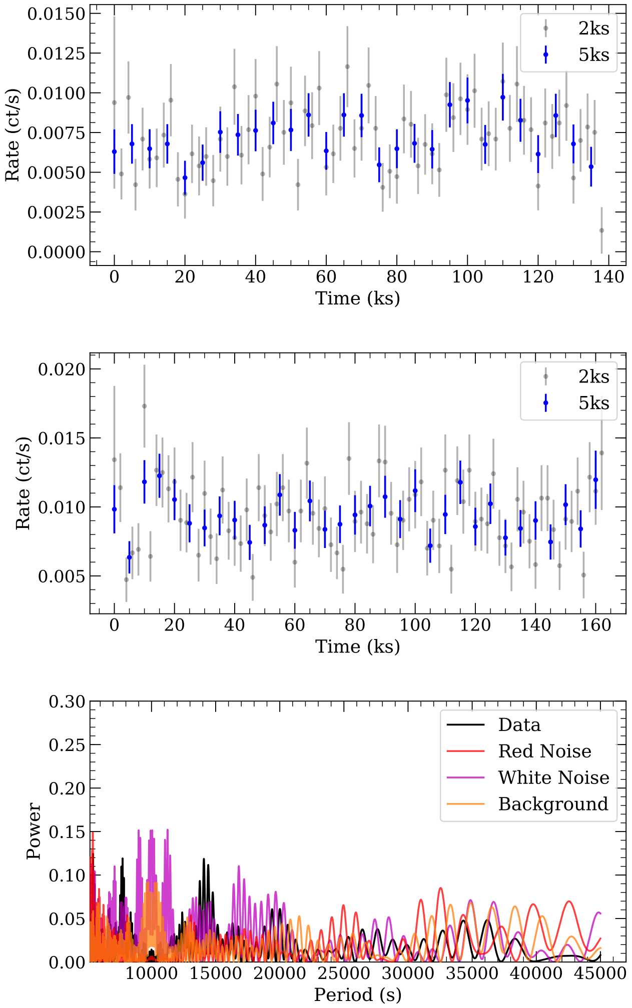

Figure 3.5: Upper: Light curve for GCU1 from ObsID 12889. Middle: Light curve for GCU1 from ObsID 12888. Both are binned by 5 ksec and 2 ksec. Lower: Lomb-Scargle periodogram of ObsIDs 12888 &12889 of GCU1 binned by 5 ksec compared to the Lomb-Scargle periodograms of the background, as well as red noise and white noise.

long observations of the four sources in NGC 4472 and two in NGC 4649 to search for any trends within the observation. The background subtracted light curves as well as the background were extracted from event files filtered to 0.5-8.0 keV using CIAO's `dmextract` tool, and binned by 2 ksec and 5 ksec.

To determine how significant (if at all) any periods identified in the periodogram are, we computed the periodograms of red noise, white noise and the background and compare them to the periodogram of the data for bins of 2 ksec and 5 ksec. We use the DELCGEN package (Connolly, 2016) to generate red noise simulations of the *Chandra* light curves (Timmer & Koenig, 1995). We also extract background light curves and compute the Lomb-Scargle periodogram in the same manner. For white noise, we shuffle[10] our original light curves and re-compute the periodogram.

We find that there are no clear significant periods in this data and that white noise is the main cause of spurious signals in the Lomb-Scargle periodogram (see Figure 3.5, (lower panel) for the various contributions of noise to the detected signals in the data).

3.3 Results

We fit a sample of eight GC ULXs located in NGC 1399, NGC 4472 and NGC 4649 (see Table 3.1) with two different single component models, an absorbed disk or an absorbed power law, and take data from the literature for a ninth (Dage et al., 2018). We also consider a power law with intrinsic absorption, but find that for almost all the sources, the intrinsic absorption component was either consistent with zero, or not a statistical improvement over a disk model.

---

[10] `https://docs.scipy.org/doc/numpy-1.15.0/reference/generated/numpy.random.shuffle.html`

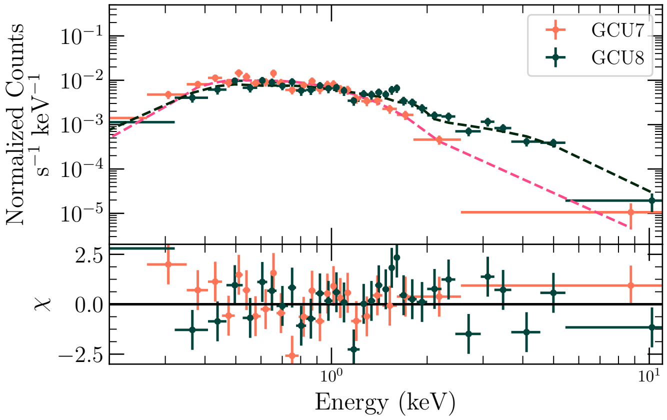

Figure 3.6: Spectra and fitted models (fit residuals on lower panel) of GCU7 and GCU8. GCU7 is best fit by a disk model, while GCU8 is much harder and better fit by a power law model.

We also consider a two component model, however, it was not enough of a statistical improvement over the single component model. In the few cases where the two component model was a statistical improvement, the power law index was always unphysical. The χ^2 statistics for the single component models either indicated that one model was a better fit than the other, or the statistics were comparable, except in the case of GCU6, which was ambiguous.

Figure 3.6 shows the best fit models and residuals for spectra from GCU7 and GCU8. GCU8 was consistently brighter than GCU7 (see Table 3.14), and the best fit model was a power law with no intrinsic absorption. The lower luminosity source, GCU7, was best fit by a `diskbb` model. In this case specifically, the system producing the emission in GCU8 is physically different than that of GCU7.

The data never require that the sources change between a disk to a power law between observations, although it is difficult to [strongly] rule out the possibility. The ninth GC ULX source, RZ2109 is the only source that is clearly a two component model (Shih et al., 2008); however its power law indices were not well constrained (Dage et al., 2018). Like these other

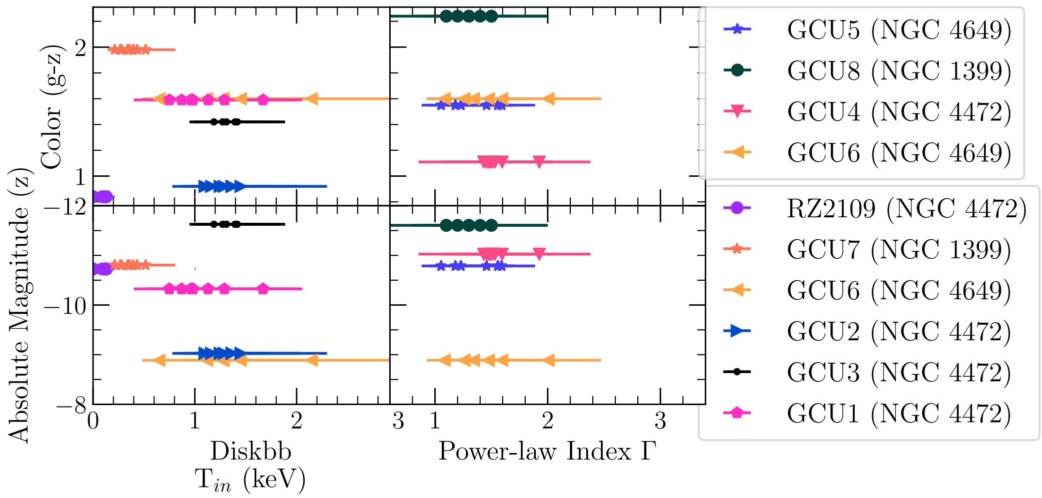

Figure 3.7: Upper: Plot of optical cluster colour $(g - z)$ versus best fit spectral parameter for GC ULXs. Lower: Plot of absolute z-band magnitude versus best fit spectral parameter for GC ULXs. Neither absolute magnitude nor colour appear to be correlated with best fit spectral parameter in this sample. However, it is worth noting how red in colour GCU8 is. (Optical cluster values from Table 3.1)

GC ULX sources, RZ2109 also shows no strong evidence for changes in spectral state.

We also compare optical cluster colour (g-z) and magnitude (z) to the best fit spectral index in Figure 3.7. There does not appear to be clear correlation between optical colour and X-ray behaviour of the sources.

The ultimate aim of this paper is to study the behaviour of the brightest ($L_X > 10^{39}$ erg s^{-1}) GC ULXs. To quantify how the spectral parameters of these sources change with their luminosity, we plot the values of the spectral component versus luminosity in Figures 3.9 and 3.10. Any GC ULX with largely better statistics for a power law was plotted in Figure 3.9; any source with consistently better statistics for a disk is plotted in Figure 3.10. GCU6 was ambiguous as to whether a disk or a power law was a better fit, so we therefore present it on both plots.

The power law sources show little variability in either Γ or luminosity. Within uncertainties, both GCU8 and GCU4 have similar luminosity and power law index values across all of their own observations, with GCU4 at a lower luminosity than GCU8. GCU6 also does not vary significantly in either parameter. GCU5 seems to follow the same behaviour, except for ObsID 785 (2000-04-20), the first observation taken of this source. It seems as though it begins with a low luminosity, then brightens and stays fairly consistent at that luminosity/Γ.

The disk sources appear to be bimodal: they are either sources with T_{in} greater than 0.5 keV, or much less than that temperature. Of the sources with $T_{in} > 0.5$ keV, GCU1 shows the most variability. GCU6 shows some variability in T_{in} and L_X. GCU2 and GCU3 do not show significant variability in either luminosity or disk temperature.

Finally, the two sources with nearly steady disk temperatures below 0.5 keV, RZ2109 at $\simeq 0.15$ keV and GCU7 at $\simeq 0.4$ keV do show significant variability in luminosity while having no large change in T_{in}. It is of note that the only sources that vary significantly with L_X but not visibly with the spectral parameter are RZ2109 and GCU7. Interestingly, both RZ2109 and GCU7 show optical emission lines (Zepf et al., 2008; Irwin et al., 2010).

To determine the extent to which variations in luminosity and variations in spectral fit parameter (either kT or Γ) are correlated and estimate the correlation slope, we determine the best fit line to the data for each individual source. To carry out this fit, we use LINMIX[11] (Kelly, 2007) which uses Bayesian inferences, and develops MCMC sampling to allow linear fits while accounting for uncertainties in both variables. However, this implementation does not allow asymmetric parameter uncertainties which typically rise in X-ray spectral fits. Thus, we conservatively chose the larger uncertainty value on each parameter for both lower and upper values. We fit the correlation with T_{in} as a function of L_X, which allows a simple test for lack of correlation for systems which luminosity seems to vary independent of disk

---

[11] Python port by J. Meyers: `https://github.com/jmeyers314/linmix`

Table 3.19: Best fit slopes and uncertainties of sources that varied in kT or L_X.

Object	Slope
RZ2109	0.0 ± 0.02
GCU1	0.29 ± 0.16
GCU7	0.08 ± 0.2

temperature (RZ2109 and GCU7).

We used this method to fit the slopes of RZ2109, GCU1, and GCU7. The best fit slopes and uncertainties are reported in Table 3.19. We did not fit slopes for GCU2, GCU3, or GCU6 as they do not appear to vary significantly in either kT or L_X. The difference in slopes between the sources below 0.5 keV (RZ2109 and GCU7) and the sources above 0.5 keV (GCU1) is suggestive of a dichotomy between low kT and high kT sources, with the low kT sources having a slope that is likely consistent with zero, and some high kT sources having a non-zero slope. See Figure 3.8 for the best fit slopes and errors of RZ2109, GCU1 and GCU7.

3.4 Conclusions

We consider a total sample of nine ultraluminous X-ray sources ($L_X \geq 10^{39}$ erg s^{-1}) physically associated with globular clusters for which we do new data analysis for eight and rely on our previous study of RZ2109 for the ninth. We find that the sources are best fit by a single component - either an absorbed disk or an absorbed power law. Two component absorbed disk plus power law model is not statistically required for any of these sources. The two component fits also give unphysical power law indices.

When we compare the luminosity to the spectral parameters of the sources, we find that sources best fit as power laws have either no clear variability in either power law index or

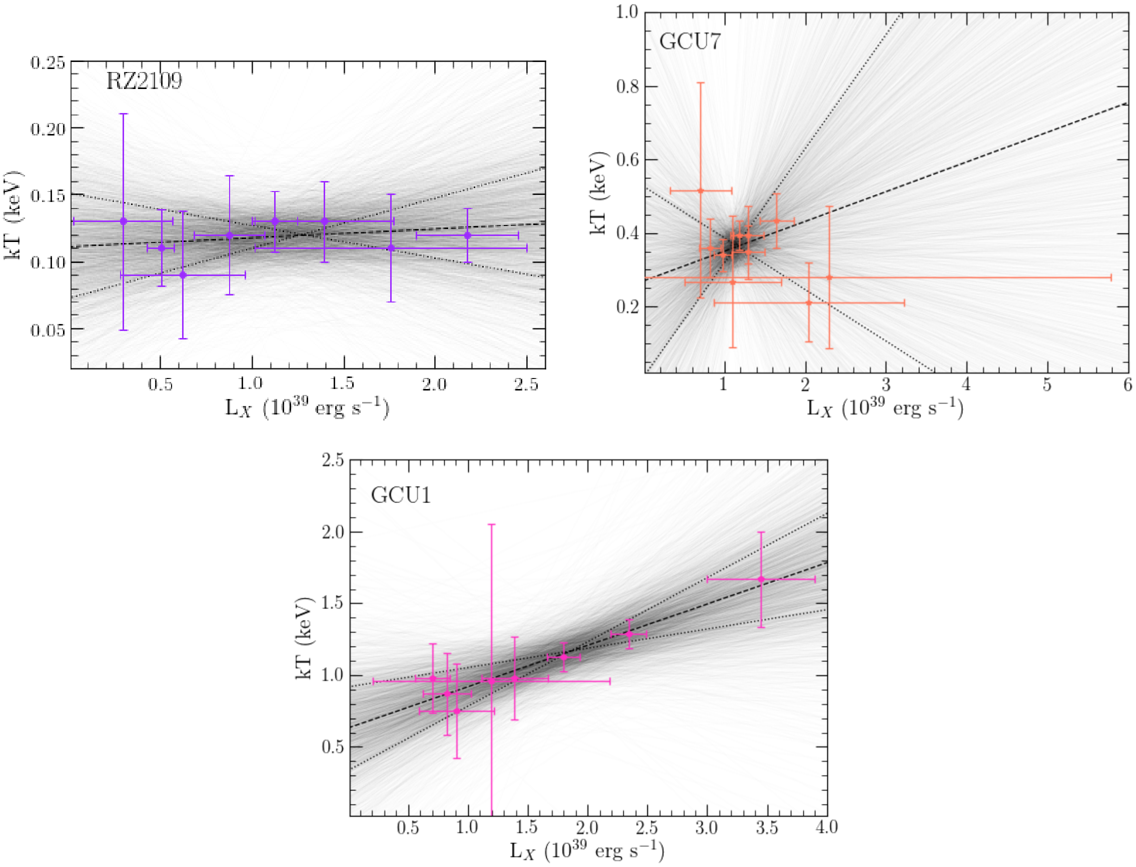

Figure 3.8: LINMIX best fits of L_X vs kT for RZ2109, GCU7 (Slopes consistent with zero) and GCU1 (slope inconsistent with zero).

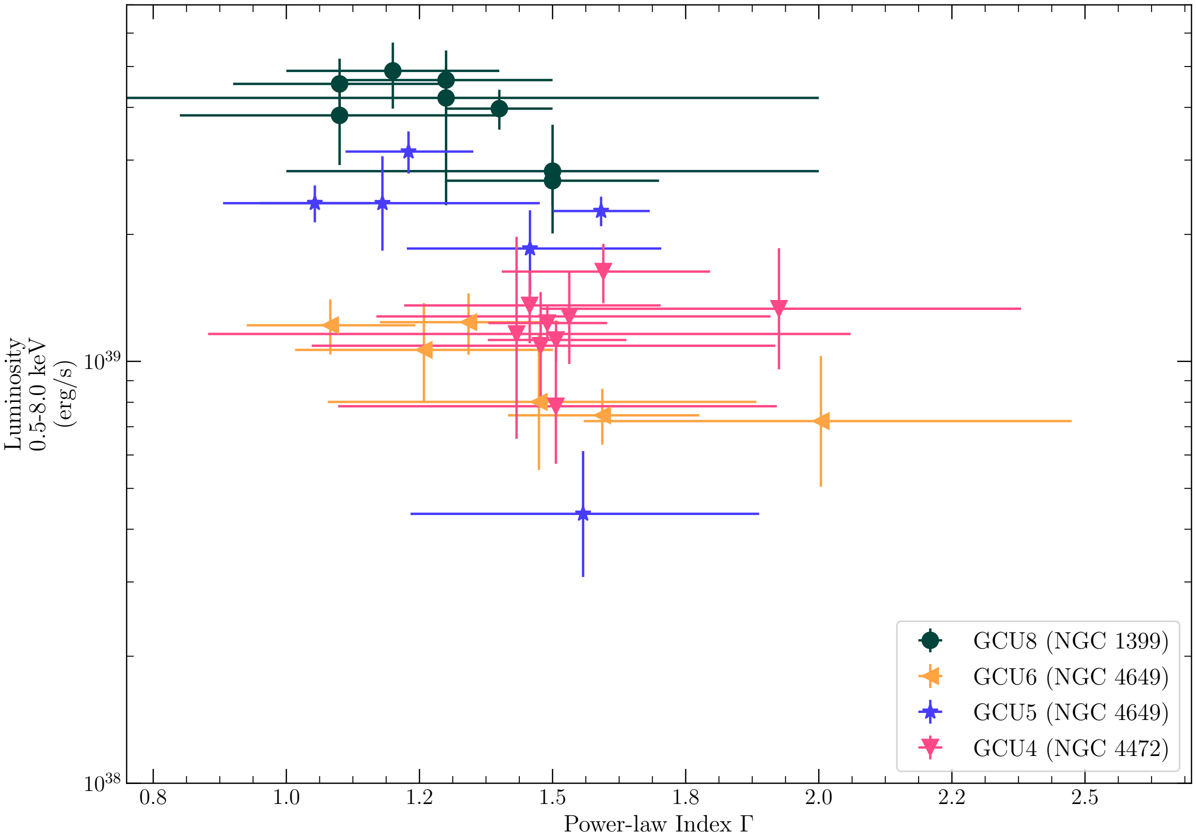

Figure 3.9: Γ vs. Luminosity (0.5-8.0 keV) for GC ULXs best fit by `tbabs*pegpwrlw`.

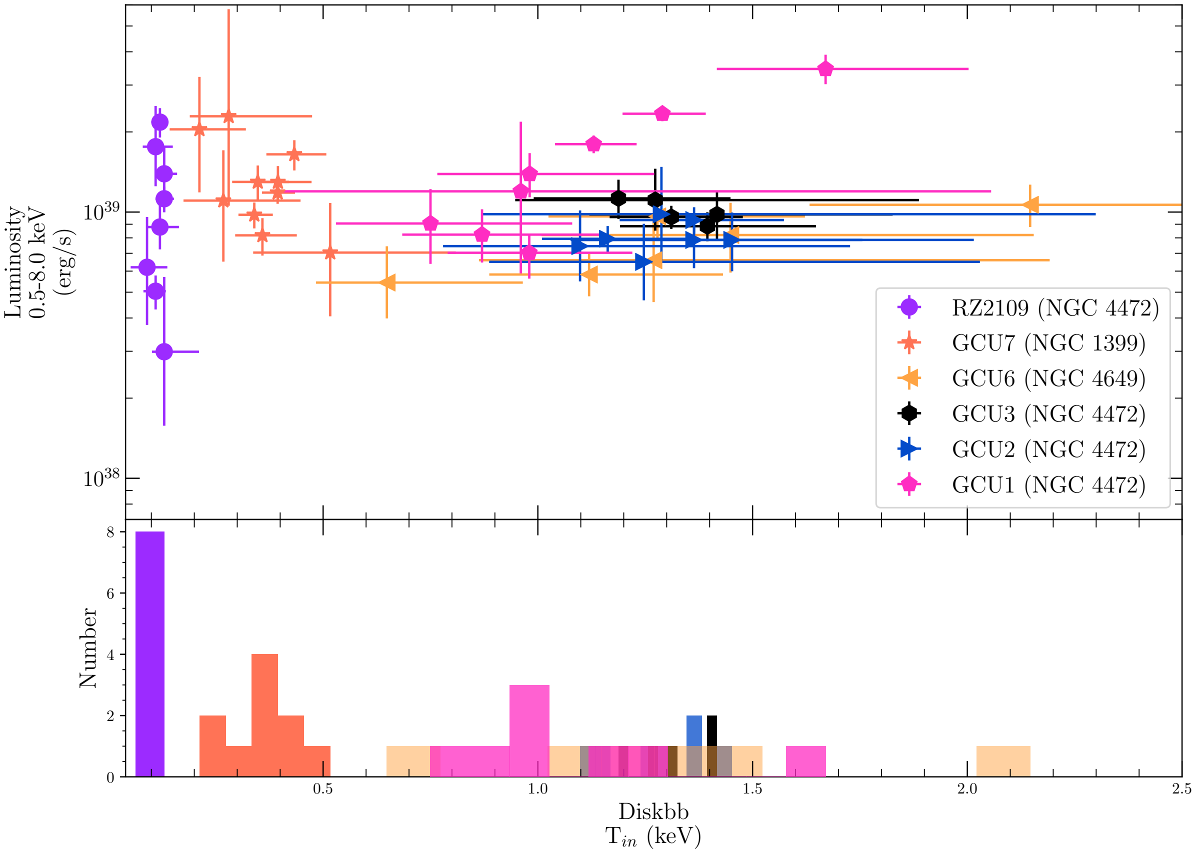

Figure 3.10: Upper:T_{in} vs. Luminosity (0.5-8.0 keV)for GC ULXs best fit by `tbabs*diskbb`. Data for RZ2109 is taken from Dage et al. (2018). Lower: Histogram of best fit kT for all sources.

luminosity, or only show mild variability in each parameter. When comparing luminosity to inner disk temperature, the sources split into two temperature ranges, one group with temperatures above 0.5 keV, and the other with low T_{in}. The part of the sample best fit by disks with temperatures below 0.5 keV and show strong variability in luminosity with no clear variability in disk temperature. The disk sources with temperatures below 0.5 keV are the only ones to show variability only in luminosity, without significant corresponding spectral changes.

Prior work (Angelini et al., 2001; Kundu et al., 2002; Sarazin et al., 2003; Jordán et al., 2004) has shown that more luminous (and presumably more massive) globular clusters are more likely to contain low mass X-ray binaries. Beyond that, our GC ULX sample does not show any clear correspondence of X-ray behaviour or luminosity to the optical photometric properties of the cluster. However, some aspects of the X-ray behaviour appear to correlate with the presence of optical emission lines. RZ2109, GCU7 and GCU5 all have published optical spectra. RZ2109 shows bright and broad [OIII] emission lines beyond the globular cluster continuum, with no hydrogen emission detected (Zepf et al., 2008). GCU7 has narrow [OIII] and [NII] emission lines beyond the cluster continuum, also with no hydrogen emission (Irwin et al., 2010). RZ2109 and GCU7 both have similar behaviours in X-ray, with consistent, low disk temperatures and luminosity variability.

GCU5 shows no optical emission lines at all, including no hydrogen emission lines. GCU5 has very different X-ray behaviour, as it has a better fit as a single power law model that does not show the same kind of luminosity variability seen in the other two sources. Additionally, when it is fit as a single disk component, it has temperatures greater than 1 keV (Roberts et al., 2012). We note that none of the three sources has hydrogen emission present.

We postulate that X-ray behaviour may be linked with optical emission, as the sources with low disk temperatures both have optical emission, but the source with no optical emission has a vastly different behaviour in X-ray. However, optical follow-up on other sources in our sample is necessary to confirm such a claim.

Acknowledgments

KCD, SEZ, and MBP acknowledge support from Chandra grant GO4-15089A and NASA grant number HST-AR-13923.001-A from the Space Telescope Science Institute, which is operated by AURA, Inc., under NASA contract NAS 5-26555. SEZ and MBP also acknowledge support from the NASA ADAP grant NNX15AI71G. This research has made use of data obtained from the Chandra Data Archive and the Chandra Source Catalog. We also acknowledge use of NASA's Astrophysics Data System and Arxiv. The authors thank Jay Strader and Ryan Urquhart for helpful discussion. We also thank the anonymous referee for their suggestions to improve the paper.

The following softwares and packages were used for analysis: CIAO, software provided by the Chandra X-ray Center (CXC), HEASOFT obtained from the High Energy Astrophysics Science Archive Research Center (HEASARC), a service of the Astrophysics Science Division at NASA/GSFC and of the Smithsonian Astrophysical Observatory's High Energy Astrophysics Division, SAOImage DS9, developed by Smithsonian Astrophysical Observatory, ASTROML, LINMIX (Kelly, 2007), NUMPY (Van Der Walt et al., 2011), DELCGEN (Connolly, 2016), MATPLOTLIB (Hunter, 2007), Palettable[12], SCIPY, and ASTROPY (Astropy Collaboration et al., 2013).

---

[12] `https://jiffyclub.github.io/palettable/`

Chapter 4

Slow Decline and Rise of the Broad [OIII] Emission Line in Globular Cluster Black Hole Candidate RZ2109

4.1 Introduction

RZ2109 is a globular cluster associated with the elliptical galaxy NGC 4472, and is host to a stellar mass black hole candidate. The X-ray source, XMMUJ122939.7+075333, associated with RZ2109 is ultraluminous ($\sim 10^{39}$ erg s^{-1}) and highly variable, with the count rate dropping by a factor of seven in only a few hours (Maccarone et al., 2007). Optical spectroscopy obtained by Zepf et al. (2007) revealed a very broad and luminous [OIII]$\lambda\lambda$4959,5007 emission lines, with a velocity width of around 2000 km s^{-1} (Zepf et al., 2008). The oxygen emission is also variable (Steele et al., 2011). RZ2109 is the only globular cluster associated with NGC 4472 to show [OIII]5007 emission, which places constraints on geometric beaming of the system. If the large X-ray luminosity were produced by strong beaming effects, it would be likely that there would be several sources with strong [O III] whose X-ray emission was beamed away from our line of sight (see Peacock et al., 2012a, for more detail).

Not only is the [OIII] emission in RZ2109 broad, but Peacock et al. (2012b) found that the oxygen emission line is spatially resolved by HST, which implies that there is an oxygen nebula within the cluster with a size scale of ∼5±2 pc. Such a large size for the nebula negates a previous hypothesis that this oxygen emission is due to ionised nova ejecta that is serendipitous in a globular cluster with a bright X-ray source as suggested by Ripamonti & Mapelli (2012), as the nova ejecta shell required to produce only [OIII] emission must be at least an order of magnitude smaller. All evidence points to the [OIII] emission being associated with an outflow powered by the ultraluminous X-ray source.

Steele et al. (2014) modelled the emission line nebula and found that the material is hydrogen-depleted, and that the emission from the material is consistent with accretion-powered outflow driven by a white dwarf donor being accreted onto a black hole, making XMMUJ122939.7+075333 (hereafter RZ2109) one of the very few candidate ultracompact X-ray binary (UCXB) systems in a globular cluster. UCXBs are hydrogen deficient systems with a white dwarf donor and either neutron star or black hole accretor, and typically have very short orbital periods of 80 minutes or less (see Van Haaften et al., 2012; Heinke et al., 2013).

In addition to being a strong black hole UCXB candidate, the RZ2109 source is also one of the few known stellar mass black hole candidates in a globular cluster (Peacock et al., 2012b; Dage et al., 2018), and possibly the brightest one. Recent theoretical work has shown that GCs are likely to host BHs, and even suggests that black holes drive the whole dynamical evolution of clusters, (e.g. Kremer et al., 2019), so it is not surprising studies are starting to find them, even if their signatures are challenging to observe. Currently there are a handful of accreting black hole candidates in Milky Way globular clusters (Strader et al., 2012a; Chomiuk et al., 2013; Miller-Jones et al., 2015; Shishkovsky et al., 2018), and there is one dynamically-confirmed black hole candidate in which there is no evidence for accretion

(Giesers et al., 2018). There are a handful of other black hole candidates in extragalactic globular clusters, including globular clusters in NGC 1399, NGC 4472 and NGC 4649 (Shih et al., 2010; Irwin et al., 2010; Maccarone et al., 2011; Roberts et al., 2012; Dage et al., 2019). Unlike the Milky Way sources, this extragalactic population of globular cluster black hole candidates are all ultraluminous X-ray sources (ULXs), and are likely exhibiting a very different accretion regime than their very much closer analogues. Some ULXs were found to exhibit coherent pulsations (e.g. Brightman et al., 2018), implying that the compact objects in the binary are neutron stars. Many models for neutron star ULXs also involve extremely high magnetic fields (Brightman et al., 2018). These may be plausible for recently formed neutron stars in star forming regions in the field, but implausible for the old stellar populations of globular clusters. The best physical explanations for these systems requires significant beaming (King et al., 2017), which has been ruled out for RZ2109 (Peacock et al., 2012a), see also Dage et al. (2019).

Of the extragalactic systems, RZ2109 is the best studied, having been monitored long-term in both X-ray and optical. Studying this system can address questions about the evolution of black holes in globular clusters, and shed light on the nature of black holes in globular clusters, as simulations predict their presence (e.g. Morscher et al., 2013, 2015; Rodriguez et al., 2016). The nature of black holes in globular clusters has become increasingly relevant in light of the LIGO discoveries, as globular clusters are one possible source for the progenitors of the merging black hole binaries detected by LIGO (Abbott et al., 2016b). In fact, recent simulations suggest that multiple generations of black hole binaries can form in globular clusters (Rodriguez et al., 2019).

In this work, we present new optical spectroscopy of RZ2109 from 2011 to 2018 and add to the Steele et al. (2011) study of the optical variability beginning in 2007. RZ2109 is also highly variable in X-ray (Maccarone et al., 2007; Shih et al., 2008). The X-ray source, which is likely to drive the ionisation of the oxygen nebula (Peacock et al., 2012b) has been monitored long-term in X-ray, from 2000-2016 (Dage et al., 2018). We compare the variability of the flux of the oxygen line to the X-ray variability from Dage et al. (2018) to search for a link between the variability in both wavelengths. Section 4.2 describes the data and analysis. The implications of these measurements on the size scale of the system in Section 4.4, and Section 4.6 discusses the impact of these results.

4.2 Optical Data and Analysis

Optical spectra have been obtained for RZ2109 since 2007. Previous observations have been reduced and presented in Steele et al. (2011): it was observed with Keck in 2007 (Zepf et al., 2008), on the William Herschel Telescope (WHT) in 2008, on the Southern Astrophysical Research Telescope (SOAR) early in 2009, and on the Gemini South Telescope later in 2009. In this paper we analyse new data starting from 2011 until 2019 to compare to previous observations and measurements. The newest observations were taken with Gemini South/Gemini Multi-Object Spectrograph (GMOS) and SOAR/Goodman High Throughput Spectrograph(GHTS), and are described in more detail below. The data were reduced using IRAF (Tody, 1986, 1993).

4.2.1 Gemini

Data were taken using GMOS on Gemini South (Hook et al., 2004) under observing program GS-2011A-Q-41. Data from both programs span a wavelength range of 4134Å to 5765Å, with a B1200 grating, resolution R=3744[1], and a 1.0” slit. Data for GS-2011A-Q-41 were taken on UT 2011-05-01, 2011-05-02, 2011-05-04, and 2011-05-05. RZ2109 was observed on Gemini South in 2015 (GS-2015A-Q-1), however, the 2015 data suffered significantly from defects on the detector which severely impacted the utility of these observations.

4.2.2 SOAR

RZ2109 was observed on the 4.1 m Southern Astrophysical Research Telescope (SOAR) using the GHTS (Clemens et al., 2004) on UT 2012-03-14, 2016-03-14, 2018-03-14, 2018-03-15, 2019-04-06 and 2019-04-07. The observations were taken using the 0.95” longslit (0.95” in 2018 and 2019), with the SYZY 930 grating. The resolution is R $\sim$ 1500. It was also observed on 28-04-2019 and 02-05-2019 with a higher resolution (1200 l/mm) grating and 0.95” longslit.

4.2.3 Equivalent Width Measurement

We develop a method in python to measure the equivalent width of the [OIII] emission of the un-normalised spectra in the following manner: we select spectral bandpasses with wavelengths longer and shorter than that of the [OIII] emission and which are relatively featureless and hence good indicators of the cluster continuum. An average value is drawn from two regions, a lower region of 4800-4875Å , and an upper region of 5100-5175Å [2]. Out of these two regions, we randomly select 25 Å wide regions over which to average. Similar to Steele et al. (2011), we measure the [OIII] emission between 4964Å and 5058Å (due to the breadth of the emission lines - $\sim$1475 km s^{-1}, Zepf et al. 2008).

---

[1] `https://www.gemini.edu/sciops/instruments/gmos/spectroscopy-overview/gratings`

[2] `https://github.com/kcdage/equivalent_width`

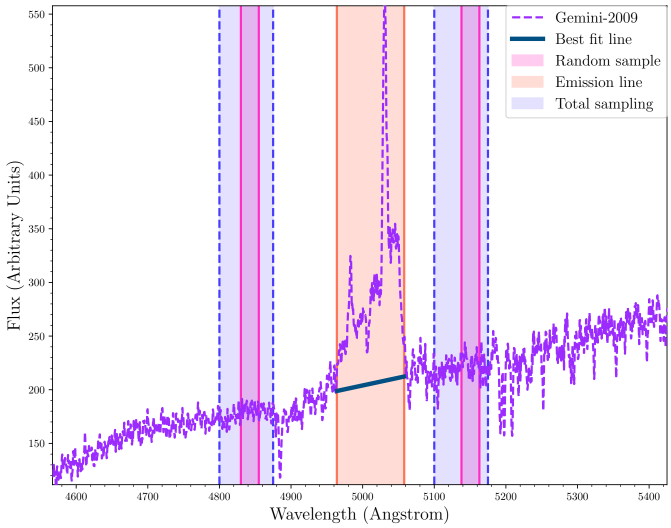

Figure 4.1: Un-normalised Gemini spectrum from 2009. The purple shaded regions show one example of the 25Å wide regions sampled out of larger regions (blue) that are averaged to approximate the continuum values at the start and end of the emission region. The orange shaded area shows the emission region we are measuring over from 4964Å to 5058Å. The blue line is the continuum fit in the region of interest.

We adopt the average value in the bluer range as the continuum value at 4964Å, and the average value in the redder range as the continuum value at 5058Å, and fit a straight line across the broad emission region. The very much lower S/N 2009 and 2012 SOAR spectra were smoothed with a 1D box filter[3]. Figure 4.1 shows one example for the 2009 Gemini spectrum. We calculate the equivalent width, and to estimate uncertainties, repeat this process 100 times, randomly drawing different regions to calculate the continuum values from. The final reported equivalent width is the average of all these trials, and the error comes from the standard deviation.

The equivalent width of RZ2109 has been measured in Steele et al. (2011) from observations spanning from 2007-2012, taken with Keck, WHT, SOAR, and Gemini. We also confirm our measurements by remeasuring a subsample of the spectra from Steele et al. (2011). The data are presented in Table 4.1.

---

[3] `http://docs.astropy.org/en/stable/api/astropy.convolution.Box1DKernel.html`

Table 4.1: [OIII] Equivalent Width (Angstrom).

Date	Instrument	Equivalent Width	Error
2007-12	Keck	31.6	1.6
2008-01	WHT	29.3	3.2
2009-02	SOAR	25.3	7.3
2009-03	Gemini	32.7	0.7
2011-05	Gemini	26.0	0.6
2012-03	SOAR	24.4	3.7
2016-03-14	SOAR	18.9	0.9
2018-03-14, 2018-03-15	SOAR	12.9	0.9
2019-04-06,2019-04-07	SOAR	16.5	1.1

4.2.4 Normalisation of the Spectra

All further analysis in this paper is based off of the higher resolution Keck, SOAR and Gemini observations. The spectral resolution of the 2009, 2011 Gemini spectra are within about 20% of the 2016, 2018 and 2019 SOAR spectra. We normalise these spectra with respect to the Keck spectrum (which has been flux calibrated) using the following procedure (in python)[4]: we calculate a moving average across 4500Å to 5500Å , but ignores 4940Å -5100Å in order to mask the [OIII] emission[5]. Then we fit a 5th order polynomial to the smoothed continuum. We divide the fitted Keck slope by the SOAR or Gemini slope to find the relative normalisation as a function of wavelength and apply it to each spectrum. The normalised spectra are presented in Figure 4.2.

4.3 X-Ray Data and Analysis

RZ2109 was observed by *Chandra* for 30 ks on 2019-04-17 (ObsID 21647), and was followed up by a series of shorter *Swift-XRT* observations triggered after the observed rise of the

---

[4] `https://github.com/kcdage/spec_slope_fit/`

[5] For the lower wavelength range,we use a lower cutoff of 4646Å instead of 4500Å in the case of the SOAR 2016 data, which had a narrower wavelength range.

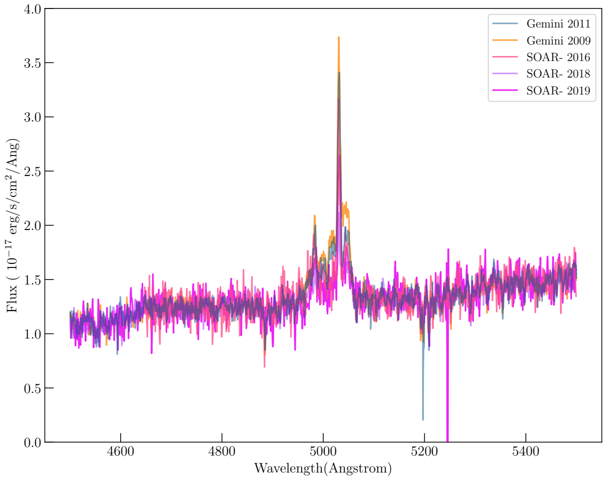

Figure 4.2: Normalised spectra from observations spanning 2007-2018. Observations are from the W.M. Keck Observatory (December 2007, [dark blue]) Gemini South (March 2009, [yellow], May 2011, [light blue]), and SOAR (March 2016, [light pink], March 2018, [light purple], April 2019 [dark purple]).

optical luminosity.

4.3.1 Chandra

RZ2109 was detected in the latest *Chandra* observation, with 7 source counts against a background of 2 counts detected in a 3.5" radius region in the 0.3-10keV energy range, making this a 3 σ detection (Gehrels, 1986). Similar to Dage et al. (2018), the source was extracted with CIAO version 4.10 using the DMEXTRACT tool (Fruscione et al., 2006) and binned by counts of 1. We fit the resultant spectrum with XSPEC (Arnaud, 1996), using Cash statistics (Cash, 1979) to fit, and Pearson Chi-Squared as the test statistic, with solar abundances from Wilms et al. (2000).

While RZ2109 is typically best-fit by an absorbed two component disk plus power-law model (Dage et al., 2018), given the poor statistics and low number of counts, an absorbed

Table 4.2: X-ray luminosities from 0.2-10 keV measured by Swift/XRT.

Date	Exposure Length seconds	L_X (0.2-10 keV) $\times 10^{39}$ erg s^{-1}
2007: 11-13, 12-(25, 27)	8327.0	$1.79\ ^{+1.16}_{-0.98}$
2010: 3-(22, 26, 30)	6061.0	≤ 2.45
2019: 4-15, 5-(13, 17, 27, 31)	5800.0	≤ 1.26

power-law model (`tbabs*pegpwrlw`, with the hydrogen absorption column fixed to 1.60[6] $\times 10^{20}$cm^{-1}) was the more appropriate choice. We caution that it is not justifiable to interpret any best fit spectral parameters physically, due to low count numbers, and we fit solely to estimate the X-ray luminosity. The best fit flux was $2.2\ ^{+6}_{-0.8} \times 10^{-15}$erg cm^{-2} s^{-1} in the 0.5-8 keV energy range. The best fit power-law index is 3.0^{+5}_{-1}. The X-ray luminosity[7] of this observation in 0.2-10 keV extended energy range calculated using PIMMS[8] and a power-law index of 3.0 is $2.0\ ^{+5.3}_{-0.7} \times 10^{38}$ erg s^{-1}.

4.3.2 Swift/X-Ray Telescope

Swift/XRT data on RZ2109 were taken in three epochs in November and December 2007, March 2010, April and May 2019. We reprocessed all Swift/XRT data using xrtpipeline (HEASoft 6.25). The source was not detected in any individual observations, thus we merged observations in each epoch (using Xselect) and investigated source brightness. The source was detected at ∼2-sigma significance in 2007, but was not detected in 2010 or 2019. The X-ray luminosities from 0.2-10 keV are presented in Table 4.2.

---

[6] `http://cxc.harvard.edu/toolkit/colden.jsp`

[7] Assuming a distance of 16.8 Mpc (Macri et al., 1999).

[8] http://cxc.harvard.edu/toolkit/pimms.jsp

4.4 Results: Time Behaviour of [OIII] Emission

Based on the observed changes in the [OIII] emission, we can consider possible implications these changes over time would have for the size scales of the oxygen nebula. In this section, we specifically address what could be causing the changes to the relative strengths of components of the [OIII]λ5007 emission line, and if we see any link between the change over time in X-ray flux and [OIII]λ5007 emission flux.

4.4.1 Time Evolution of the [OIII] emission

We have been monitoring the [OIII]$\lambda\lambda$4959,5007 emission of RZ2109 since 2007 to examine how the emission has changed over time, and how changes in the optical emission compare to any changes in the X-ray luminosity. Figure 4.3 plots the full [OIII]λ5007 equivalent widths from Steele et al. (2011) and Table 4.1 to the X-ray luminosities of RZ2109 taken from Maccarone et al. (2010b), Dage et al. (2018), and Table 4.2.

One of the goals of this work is to use these data to constrain the size of the [OIII] emitting nebula. From Figure 4.3 it is clear that the [OIII]λ5007 luminosity decreases by about a factor of two over a timescale of about 3,000 days. Because the light crossing time of the emitting region provides a rough lower limit to the timescale on which the emission can be seen to vary, the data shown in Figure 4.3 place an upper limit on the size of the emitting region to be about four light years across.

This approach gives an upper limit to the size of the emitting region, but does not provide further information about its size. An alternative approach is to assume the observed decline in the emission line is due to the oxygen nebula expanding and lowering the overall density of material by a factor of two while the central source remains constant. Given this assumption

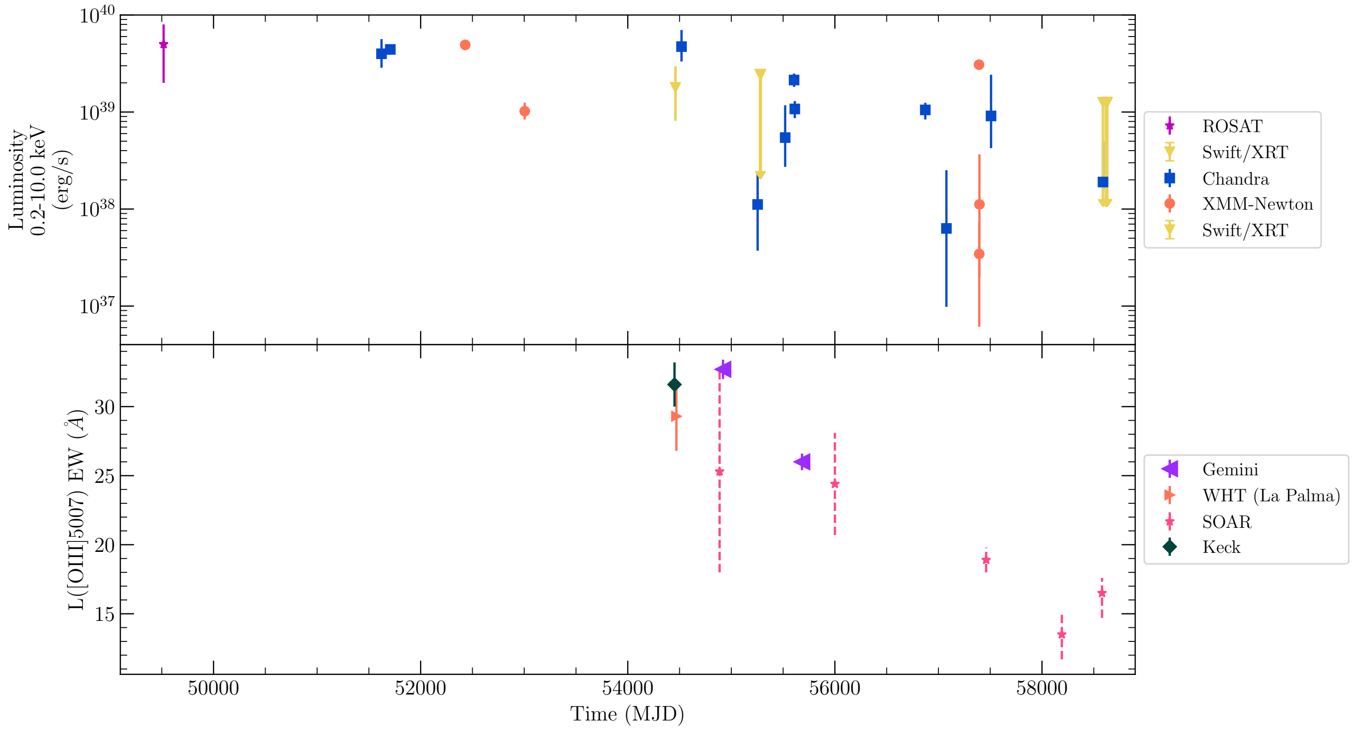

Figure 4.3: Upper panel: Change in X-ray luminosity over time. Purple star is *ROSAT*, Blue squares are *Chandra* observations, orange circles are taken from *XMM-Newton* observations, yellow triangles are upper limits from *Swift/XRT*. See Maccarone et al. (2010b), Dage et al. (2018), and Section 4.3 of this paper for X-ray analysis. Lower panel: Change in L(5007) over time, L(5007) equivalent widths are presented in Table 4.1.

the size scale can be estimated based on the following equations:

$$r_{\text{final}} = r_{\text{initial}} + (V_{\text{expansion}}) \times t_{\text{decline}} \tag{4.1}$$

$$r_{\text{final}}^{3} = 2 \times r_{\text{initial}}^{3}. \tag{4.2}$$

Adopting eight years as the time over which the emission is seen to decline and an expansion rate for the emitting region of 1000 km/s (approximately one half the line width), we find that under these assumptions, the current size scale would be roughly 0.04 pc. We can also compare this to the absolute lower limit for the size of the emitting region set by the volume required at the critical density of the [OIII]λ λ4959,5007 emission line required to produce the observed line luminosity. As also shown in (Steele et al., 2011), this minimum size is a few 10^{-3}pc. The half-light radius of the emitting region could be limited to greater than $\sim 10^{-3}$ pc at the low end and $\sim$2 pc at the high end.

4.4.2 Time Evolution of the Core and Red and Blue Wings of the Emission Line

Differential behaviour between the red and blue wings of the observed [OIII] emission can also provide a constraint on the size scale of the nebula. We will observe changes in the red wing which should lag changes in the blue wing due to the difference in light travel time between the material moving toward us and material moving away. Any such change is convolved with possible changes in the structure of the emitting region, but such a comparison may still provide a useful test of the consistency of models of the spatial scale of the nebulae.

To estimate this possible lag, we utilise the work of Steele et al. (2014) who modelled the structure of the λ5007 emission region and found that it is best described by a Gaussian core with red and blue shifted wings. We compute the equivalent widths in the wings and the core of the emission line in the normalised spectra by defining three regions: 5006-5026Å as the blue wing, 5026-5037Å as the core, and 5037-5057Å as the red wing (see Figure 4.4). We calculate the errors by extending the regions by 2Å on either side, recomputing the equivalent width and taking the difference. The λ4959 core emission was measured across 4978-4989Å , the same width of region as the λ5007 emission core, but centered around the λ4959 core. The uncertainty was propagated by recomputing the equivalent width for a range of continuum values.

As can be seen in Figure 4.5 while all three structures appear to decay with time, they do not appear to do so in concert. At most epochs, the red emission wing is brighter than the blue wing, but fainter than the core. However, in the past two years, the core continued dropping, then rose, while the red wing seems to have possibly flattened and the blue wing appears to continue to fade. The changes in the core are highly significant compared to the measurement uncertainties, but this is not the case for the wings. Both the λ4959 and λ5007 core emission follow the same trend (Figure 4.6).

As noted above, if the decline of the observed [OIII] flux is due to the central ionising source declining, and the timescale over which it declines is indicative of the size scale of the emitting region, then the red wing of the emission line should lag the behaviour of the blue wing of the emission line, and the time lag should be similar to the overall spatial scale of the emitting region.

Based on the data presented in Figure 4.4, the red wing may lag the blue wing by around 2500 days ($\sim$ 7 years). This is similar to the size scale derived from the time it takes the

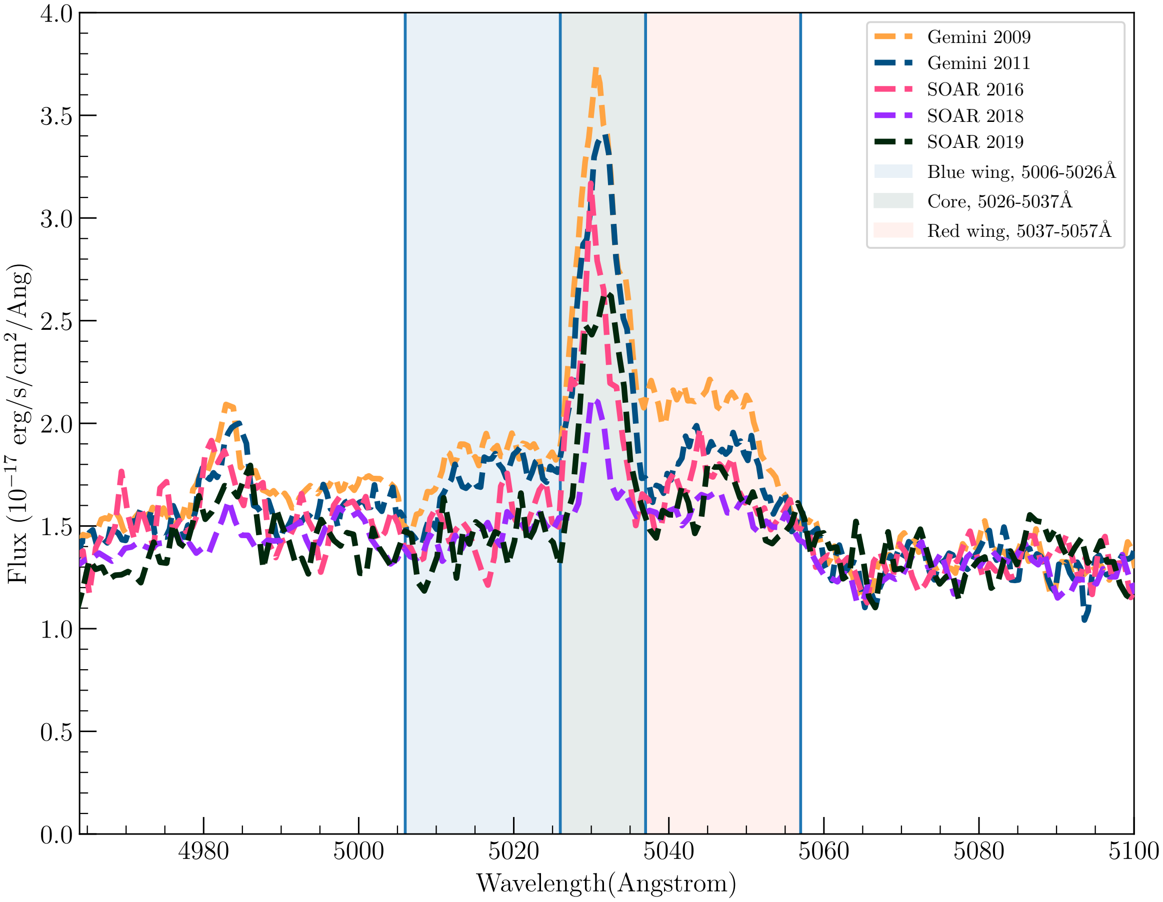

Figure 4.4: Intervals of the [OIII]λ5007 emission line components, 5006-5026Å for the [OIII] blue wing, 5026-5037Å for the [OIII] core, and 5037-5057Å for the [OIII] red wing.

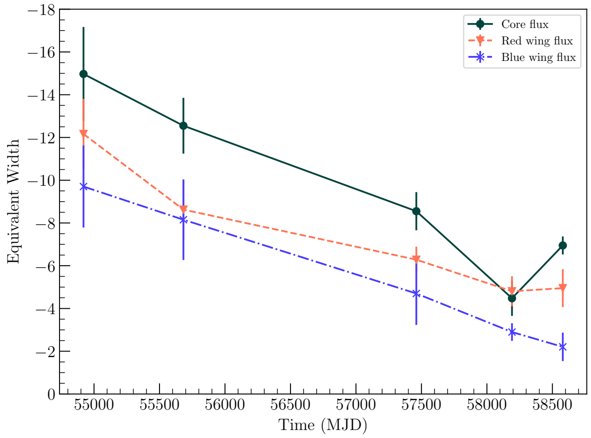

Figure 4.5: Flux in each regime of the emission line over the course of the observations.

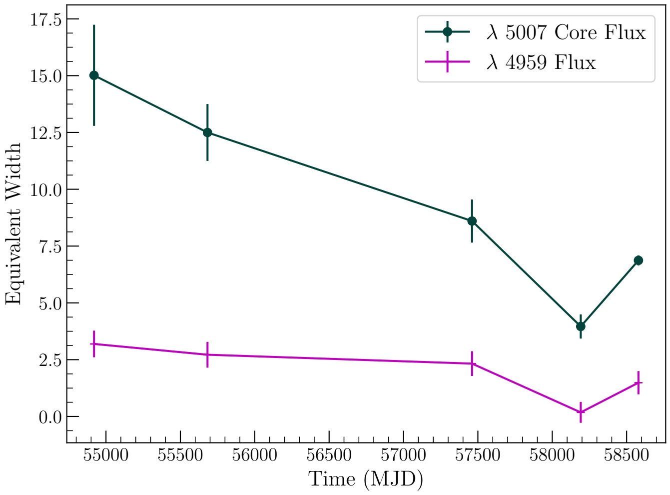

Figure 4.6: Flux in each regime of the λ4959, λ5007 emission cores.

overall luminosity to decline by a factor of two. We note that these two measurements are independent - the overall luminosity could decline without any difference in the red and blue wings, or without the red wing being consistent with lagging the blue wing. However, it remains the case that one can construct smaller size scale models where the changes are due to the structure of emitting regions and not due to light travel times.

These implications are a contrast to the spatially resolved HST-STIS spectroscopy analysed by Peacock et al. 2012b. In this work, the HST-STIS spectroscopy appeared to be spatially resolved, with the emitting region having an extent of 5 ± 2 pc. The variability results appear to suggest a spatial scale on the low end of this very difficult measurement.

4.4.3 X-ray Behaviour Versus [OIII]

Any relation between changes in the X-ray and [OIII] λ5007 luminosities can be tested by monitoring RZ2109 in both X-rays and [OIII]$\lambda\lambda$4959,5007 emission. RZ2109 has been observed in both of these wavelengths for more than a decade. In particular, if the optical emitting region is of order a parsec in size, any change observed in the ten or so years we have been observing it must be due to changes in the central X-ray source illuminating the region, as such a large region can not change its structure so quickly. In this case there should be a correlation between the X-ray flux averaged over the light travel time of the system and the [OIII] λ5007 flux.

Figure 4.3 compares the full equivalent widths from Steele et al. (2011) and Table 4.1 to the X-ray luminosities of RZ2109 taken from Maccarone et al. (2010b), Dage et al. (2018), and new data presented in this paper (Table 4.2).

Ideally, we would compare the time changes in the X-ray luminosity to those of the [OIII] λ5007 luminosity to help distinguish between these possibilities for the size of the [OIII] λ5007 emitting nebula. Fundamentally, because the X-ray emitting region is orders of magnitudes smaller than the [OIII] λ 5007 nebular emitting region for any physically plausible model, the [OIII] λ 5007 emission should lag changes in the X-ray emission by a time comparable to the light crossing time of the [OIII] λ 5007 emitting nebula. In order to carry out this test, we need to establish the effective L_X seen by the [OIII] λ 5007 emitting region on the relevant timescales of months to years. However, determining the effective L_X over longer time periods is made difficult by the widespread short-term variability of

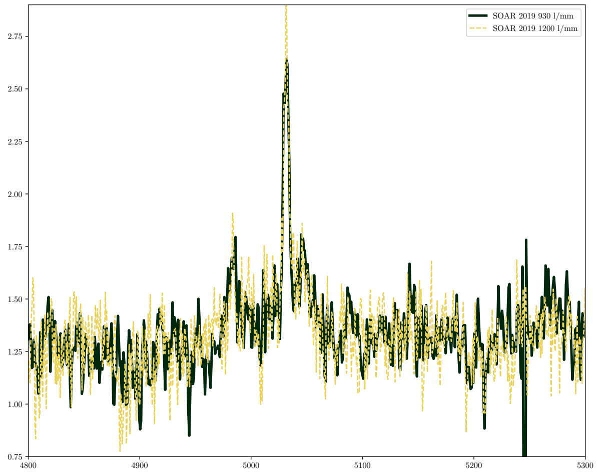

Figure 4.7: Measurements from early April 2019, and late April 2019 verifying the increase in the [OIII] emission on two different gratings.

RZ2109, so that any X-ray observation may not give a representative value for the L_X at that time. Given this caution it is still notable that the observed L_X in the top panel of Figure 4.3 suggest an overall decline of the L_X of RZ2109.

4.4.4 Rise in [OIII] Emission

While the [OIII] emission has been observed in a long-term decline since 2010, in April 2019 the flux in the core was observed to be increasing. Subsequent measurements approximately a month later with a higher resolution grating verify the observed increase (See Figure 4.7). A close up of the spectrum from 2016-2019 is shown in Figure 4.8 to highlight the decline and rise of the emission line.

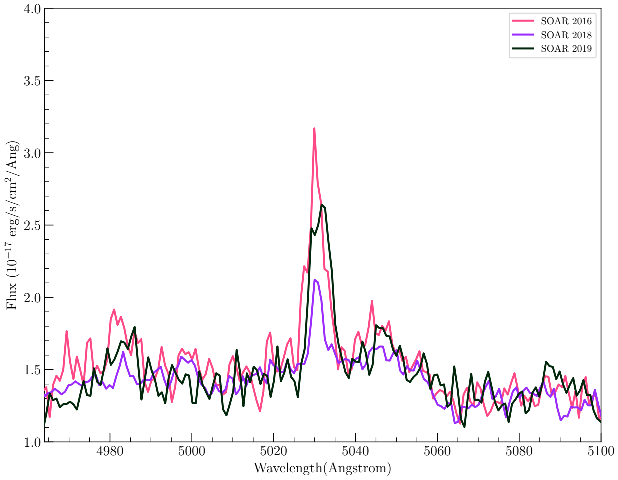

Figure 4.8: Spectra from 2016-2019 showing decline and subsequent increase.

4.5 Comparison to Milky Way GC Sources

There is one candidate globular cluster BH UCXB candidate among Galactic globular clusters, 47 Tuc X9. This source has $L_X \sim$ a few $\times 10^{33}$ erg s^{-1}, but unlike typical compact binaries in of this luminosity, also shows bright radio continuum emission (Miller-Jones et al., 2015). X-ray timing suggests an orbital period about 28 min, and the X-ray spectrum shows emission lines consistent with Oxygen VII and VIII and indicates overabundance of oxygen (and possibly carbon) in the system. (Bahramian et al., 2017), but no evidence for optical hydrogen or helium emission/absorption (Tudor et al., 2018), suggesting a CO white dwarf donor, as inferred for RZ2109. Carbon emission lines were also detected in the FUV spectrum (Knigge et al., 2008). Hence, 47 Tuc X9 appears as reasonable analogue for RZ2109 excepting its lower X-ray luminosity. This can be understood in the context of the evolutionary timescales of UCXBs: RZ2109 is expected to be in a relatively brief period ($\sim 10^5$ yr) of high mass transfer but will evolve to a fainter, more extended ($\sim 10^7$–10^8 yr), longer period system akin to 47 Tuc X9 (Van Haaften et al., 2012; Church et al., 2017).

We can also consider whether the size scale of the RZ2109 nebula and its implications for the age of the system are consistent with such a scenario. If the size of the RZ2109 nebula is on the order of a parsec, then the system has to be old enough so that the outflowing material can reach this radius. At the observed outflow velocity of about 10^3 km/s, this corresponds to an estimated age of about 10^3 years. Alternatively, if the system is much smaller with a size of $10^{-1} - 10^{-2}$pc, then the age can be correspondingly younger. These are formally lower limits to the age of the system, as the system could have been expanding for longer, and the size scale of the emitting nebula could not be the fullest extent of the ejected material but rather where the density and ionisation parameter are such that it where most of the [OIII] is produced. Therefore, age constraints from the size estimates for the nebula are readily consistent with an age much less than the 10^5 years duration of this evolutionary stage, although they do not absolutely require it.

There is also good reason to believe that the early evolution of the system leads to strong mass ejection. A CO WD donor, as implied by the optical and X-ray data, must have had an initial mass of at least 0.4 $M_\odot$ (Prada Moroni & Straniero, 2009), and white dwarfs at or about this mass will require non-conservative mass transfer with strong wind emission to remain in stable mass transfer(Van Haaften et al., 2012). Thus there is both a mechanism to drive oxygen into a nebula and sufficient time for it to reach the size scales we estimate.

4.6 Conclusions

RZ2109 shows very broad [OIII]$\lambda\lambda$4959,5007 emission, which is also variable. We have been monitoring it with multiple telescopes since 2007 and find that the emission has declined over the last nine years of monitoring.

Clausen & Eracleous (2011); Clausen et al. (2012b) model the X-ray and optical behaviour of an intermediate mass black hole tidally disrupting a white dwarf. The decline of the [OIII] luminosity predicted in the model in Clausen & Eracleous (2011) happens much more quickly than what we observe here. Similarly, RZ2109 is declining on a much slower timescale than predicted by the model from Ripamonti & Mapelli (2012) of a serendipitous bright X-ray source and nova shell ejection. It is also unlikely that these two unique phenomena are serendipitous in the same cluster.

The oxygen emission is likely caused by X-ray ionisation of the oxygen nebula in the cluster, therefore we expect a link between the X-ray variability and oxygen emission. However, due to the large size of the nebula, it is unclear over what timescales a potential link between the X-ray and optical variability would be observed. The similarity of the declines between both the [OIII] core and the red and blue high velocity wings are an interesting challenge to models of the physical origin.

While there may be a hint of a correlation between X-ray luminosity and optical flux, future monitoring in X-ray and optical of RZ2109 could help determine if this really is the case. Future optical monitoring of RZ2109's [OIII] emission line can help address whether the oxygen emission will continue to decline, and how the broad and narrow components of the [OIII] emission vary.

Acknowledgements

KCD, SEZ, and MBP acknowledge support from Chandra grant GO4-15089A. SEZ and MBP also acknowledge support from the NASA ADAP grant NNX15AI71G. This research is based on observations obtained at the Southern Astrophysical Research (SOAR) telescope, which is a joint project of the Ministério da Ciência, Tecnologia, e Inovação (MCTI) da República Federativa do Brasil, the U.S. National Optical Astronomy Observatory (NOAO), the University of North Carolina at Chapel Hill (UNC), and Michigan State University (MSU). This research has made use of the XRT Data Analysis Software (XRTDAS) developed under the responsibility of the ASI Science Data Center (ASDC), Italy. We also acknowledge use of NASA's Astrophysics Data System and Arxiv. KCD acknowledges Jamie Kennea and the Swift ToO Team, and thanks James Miller-Jones and ICRAR/Curtin University. JS acknowledges support from the Packard Foundation. The authors thank the referee for thoughtful and insightful comments.

The following software and packages were used for analysis: IRAF, distributed by the National Optical Astronomy Observatories, which are operated by the Association of Universities for Research in Astronomy, Inc., under cooperative agreement with the National Science Foundation, SAOImage DS9, developed by Smithsonian Astrophysical Observatory, numpy (Van Der Walt et al., 2011), Palettable[9], and matplotlib (Hunter, 2007).

---

[9] `https://jiffyclub.github.io/palettable/`

Chapter 5

Conclusions

5.1 Summary and Perspectives

This work is aimed at probing the multiwavelength nature of black hole candidates in extragalactic globular clusters by studying ULXs physically associated with globular clusters. Not only have we identified a number of black hole candidates in extragalactic globular clusters, but we have observationally probed their fascinating and strange accretion signatures.

Long-Term X-ray Monitoring of RZ2109: Chapter Two details the results of data spanning 16 years of X-ray monitoring of the source RZ2109. The combination of the high X-ray luminosity, short term X-ray variability, X-ray spectrum, and optical emission suggest that this system is likely an accreting black hole in a globular cluster. A total of 15 spectra from *Chandra* and *XMM-Newton*, were analysed and fit with XSPEC models. The spectra are all dominated by a soft component, which is very soft with typical fit temperatures of T $\simeq$ 0.15 keV for a multicolor blackbody disk. The resulting X-ray fluxes show strong variability on short and long timescales, while the X-ray spectrum often shows no significant change even with luminosity changes as large as a factor of five. The persistence of spectral parameters, along with the rapid variability, make RZ2109 stand out from the rest of the ULX population. While the underlying physical nature cannot be completely discerned without a thorough study of the lower energy X-ray emission of the source, the steadfastness of the best-fit spectral parameters indicates that the shape of the emission, and therefore the configuration of the central engine and the overall accretion process do not vary over the wavelengths probed.

X-ray Analysis of the Larger Globular Cluster ULX Sample: Chapter Three contains the analysis for a further eight globular cluster ULX sources in NGC 4472, NGC 4649 and NGC 1399. Their behavior in both X-ray and optical were compared to RZ2109. The eight GC ULXs were fit with either a single power law and single disk models, where the data never requires that any of the sources change between a disk and a power law across successive observations.

In the case of the softer (disk) models, the fits were bimodal: either the sources were better fit by a higher disk temperature (T $>$ 0.5 keV) or (like RZ2109) had a lower disk temperature (T $<$ 0.5 keV) with the spectral parameter constant while varying in luminosity. The GC ULXs best fit by a single disk show a bimodal distribution: they either have temperatures well below 0.5 keV, or variable temperatures ranging above 0.5 keV up to 2 keV. The GC ULXs with low kT have significant changes in luminosity but show little or no change in kT. By contrast, the sources with higher kT either change in both kT and L_X together, or show no significant change in either parameter. There is a likely correlation between the disk temperature and whether or not the source has optical emission, as the optical spectra of the low kT sources show optical emission, and a number of the higher kT sources have no emission beyond the cluster continuum. This study indicates that the sources fall into three different "classes" (i.e. three different types of physical accretion processes), and most importantly no evidence of state changes between the different accretion processes. The low kT sources clearly have a unique and steady accretion mechanism, while the higher kT sources appear to act like very luminous Galactic BH sources, and the harder power-law sources have a strong non-thermal component.

Slow Decline and Rise of [OIII] Emission in RZ2109: Chapter Four describes 10 years of long-term optical spectroscopic monitoring of RZ2109. RZ2109 is particularly notable because optical spectroscopy shows it has broad, luminous [OIII]$\lambda\lambda$4959,5007 emission, while also having no detectable hydrogen emission. The flux of the emission line is significantly lower in recent observations from 2016-2018 than it was in earlier observations in 2007-2011, and the emission line changes shape over time. Both the core and the wings of the emission line decline over time, with some evidence that the core declines more rapidly than the wings. However, the most recent observations (in 2019) unexpectedly show the emission line core re-brightening. This has implications that the size scale of the emission nebula may be smaller than previously thought.

RZ2109 and other globular cluster ULXs comprise a very unique population sitting at the cornerstone of two major fields: globular cluster dynamics, and extreme accretion physics. Their number and characteristics can inform on the nature of black holes in globular clusters, and therefore the progenitors to the sources detected by LIGO. The field of ULXs as a whole can also benefit from multiwavelength studies of these sources, as it is quite exciting that the old and dynamic globular cluster environment can host such high luminosity sources.

5.2 Future Directions

This work is at the crossroads of two major fields of study: extreme accretion physics and globular cluster dynamics. Globular cluster ULXs represent a new class of objects accreting at super-Eddington rates, as well as a probe of the brightest globular cluster black hole candidate population. The existence of these sources present a number of questions, such as:

How do ULXs in globular clusters compare to ULXs in star-forming regions of galaxies? The components of star-forming ULXs are likely to be neutron stars with massive, hydrogen rich donor stars. By contrast, ULXs in globular clusters are likely to be stellar mass BHs with low mass, metal poor donors. However, little work to date has been done to extensively compare the X-ray observations of the two types of sources, which is something that will be able to be accomplished once more GC ULXs have been identified and studied.

How do ULXs in globular clusters associated with spiral galaxies compare to those associated with elliptical galaxies? Currently, all known globular cluster ULX sources are found near elliptical galaxies. Searching for ULXs in globular clusters associated with spiral galaxies could have exciting implications for the link between ULXs associated with star-forming regions of galaxies and ULXs in globular clusters associated with elliptical galaxies.

Do GCs that host ULXs have different structures than those which do not? This question is fueled by the physical effects that hosting a black hole is theoretically expected to have on the structure of the host cluster. Identifying more GC ULXs will enable a study and comparison of the optical properties of the clusters which host ULXs compared to those which do not.

All of these questions have long-lasting implications for understanding a new class of ULXs (and understanding ULXs as a whole), for understanding the dynamics and formation of BHs in GCs, and for understanding the sources which lead to the BH-BH merger events detected by LIGO. The key to beginning to answer these questions is to discover new populations of ULXs in globular clusters in both spiral and elliptical galaxies and to carry out detailed multiwavelength analysis of the sources to probe their high-energy nature and search for outflows.

BIBLIOGRAPHY

BIBLIOGRAPHY

Abadie J., et al., 2010, Classical and Quantum Gravity, 27, 173001

Abbott B. P., et al., 2016a, Physical Review Letters, 116, 061102

Abbott B. P., et al., 2016b, , 818, L22

Angelini L., Loewenstein M., Mushotzky R. F., 2001, , 557, L35

Arnaud K. A., 1996, in Jacoby G. H., Barnes J., eds, Astronomical Society of the Pacific Conference Series Vol. 101, Astronomical Data Analysis Software and Systems V. p. 17

Astropy Collaboration et al., 2013, , 558, A33

Bachetti M., et al., 2013, , 778, 163

Bachetti M., et al., 2014, , 514, 202

Bahramian A., et al., 2017, , 467, 2199

Balbus S. A., Hawley J. F., 1998, Reviews of Modern Physics, 70, 1

Binder B. A., Levesque E. M., Dorn-Wallenstein T., 2018, preprint, p. arXiv:1807.05309 (`arXiv:1807.05309`)

Blakeslee J. P., Lucey J. R., Barris B. J., Hudson M. J., Tonry J. L., 2001, , 327, 1004

Blakeslee J. P., et al., 2009, , 694, 556

Brassington N. J., et al., 2008, The Astrophysical Journal Supplement Series, 179, 142

Brassington N. J., et al., 2009, The Astrophysical Journal Supplement Series, 181, 605

Brassington N. J., et al., 2010, , 725, 1805

Brightman M., et al., 2018, Nature Astronomy, 2, 312

Broos P., Townsley L., Getman K., Bauer F., 2012, AE: ACIS Extract, Astrophysics Source Code Library (ascl:1203.001)

Cash W., 1979, , 228, 939

Chatterjee S., Rodriguez C. L., Kalogera V., Rasio F. A., 2017, , 836, L26

Chomiuk L., Strader J., Maccarone T. J., Miller-Jones J. C. A., Heinke C., Noyola E., Seth A. C., Ransom S., 2013, , 777, 69

Church R. P., Strader J., Davies M. B., Bobrick A., 2017, , 851, L4

Clark G. W., 1975, , 199, L143

Clausen D., Eracleous M., 2011, , 726, 34

Clausen D., Eracleous M., Sigurdsson S., Irwin J. A., 2012a, in European Physical Journal Web of Conferences. p. 01005, doi:10.1051/epjconf/20123901005

Clausen D., Sigurdsson S., Eracleous M., Irwin J. A., 2012b, , 424, 1268

Clemens J. C., Crain J. A., Anderson R., 2004, in Moorwood A. F. M., Iye M., eds, Vol. 5492, Ground-based Instrumentation for Astronomy. pp 331–340, doi:10.1117/12.550069

Connolly S. D., 2016, DELightcurveSimulation: Light curve simulation code (ascl:1602.012)

Dage K. C., Zepf S. E., Bahramian A., Kundu A., Maccarone T. J., Peacock M. B., 2018, preprint, p. arXiv:1806.01848 (`arXiv:1806.01848`)

Dage K. C., Zepf S. E., Peacock M. B., Bahramian A., Noroozi O., Kundu A., Maccarone T. J., 2019, , 485, 1694

Davis J. E., et al., 2012, in Space Telescopes and Instrumentation 2012: Ultraviolet to Gamma Ray. p. 84431A, doi:10.1117/12.926937

Earnshaw H. M., Roberts T. P., 2017, , 467, 2690

Fabrika S., Ueda Y., Vinokurov A., Sholukhova O., Shidatsu M., 2015, Nature Physics, 11, 551

Feng H., Tao L., Kaaret P., Grisé F., 2016, , 831, 117

Fruscione A., et al., 2006, in Society of Photo-Optical Instrumentation Engineers (SPIE) Conference Series. p. 62701V, doi:10.1117/12.671760

Fürst F., et al., 2016, , 831, L14

Gallo E., Fender R. P., Pooley G. G., 2003, , 344, 60

Gehrels N., 1986, , 303, 336

Giersz M., Askar A., Wang L., Hypki A., Leveque A., Spurzem R., 2019, , 487, 2412

Giesers B., et al., 2018, , 475, L15

Giesers B., et al., 2019, , 632, A3

Gladstone J. C., Roberts T. P., Done C., 2009, , 397, 1836

Greene J. E., Strader J., Ho L. C., 2019, arXiv e-prints, p. arXiv:1911.09678

Hameury J. M., King A. R., Lasota J. P., 1986, , 162, 71

Hanawa T., 1989, , 341, 948

Heggie D. C., 1975, , 173, 729

Heggie D. C., Giersz M., 2014, , 439, 2459

Heinke C. O., Ivanova N., Engel M. C., Pavlovskii K., Sivakoff G. R., Cartwright T. F., Gladstone J. C., 2013, , 768, 184

Hook I. M., Jørgensen I., Allington-Smith J. R., Davies R. L., Metcalfe N., Murowinski R. G., Crampton D., 2004, Publications of the Astronomical Society of the Pacific, 116, 425

Hunter J. D., 2007, Computing in Science and Engineering, 9, 90

Hut P., Bahcall J. N., 1983, , 268, 319

Hut P., Paczynski B., 1984, , 284, 675

Hut P., McMillan S., Romani R. W., 1992, , 389, 527

Irwin J. A., Brink T. G., Bregman J. N., Roberts T. P., 2010, , 712, L1

Israel G. L., et al., 2017a, Science, 355, 817

Israel G. L., et al., 2017b, , 466, L48

Ivanova N., Chaichenets S., Fregeau J., Heinke C. O., Lombardi J. C. J., Woods T. E., 2010, , 717, 948

Jordán A., et al., 2004, , 613, 279

Joseph T., 2013, PhD thesis, University of Southampton, `https://eprints.soton.ac.uk/354111/`

Kaaret P., Feng H., Roberts T. P., 2017, Annual Review of Astronomy and Astrophysics, 55, 303

Kalogera V., King A. R., Rasio F. A., 2004, , 601, L171

Kelly B. C., 2007, , 665, 1489

King A. R., Davies M. B., Ward M. J., Fabbiano G., Elvis M., 2001, , 552, L109

King A., Lasota J.-P., Kluźniak W., 2017, , 468, L59

Knigge C., Dieball A., Maíz Apellániz J., Long K. S., Zurek D. R., Shara M. M., 2008, , 683, 1006

Kozai Y., 1962, , 67, 591

Kremer K., Chatterjee S., Ye C. S., Rodriguez C. L., Rasio F. A., 2019, , 871, 38

Kulkarni S. R., Hut P., McMillan S., 1993, , 364, 421

Kundu A., Maccarone T. J., Zepf S. E., 2002, , 574, L5

Li Z., et al., 2010, , 721, 1368

Lomb N. R., 1976, , 39, 447

Luo B., et al., 2013, The Astrophysical Journal Supplement Series, 204, 14

Maccarone T. J., Warner B., 2011, , 410, L32

Maccarone T. J., Kundu A., Zepf S. E., 2003, , 586, 814

Maccarone T. J., Kundu A., Zepf S. E., Rhode K. L., 2007, , 445, 183

Maccarone T. J., Long K. S., Knigge C., Dieball A., Zurek D. R., 2010a, , 406, 2087

Maccarone T. J., Kundu A., Zepf S. E., Rhode K. L., 2010b, , 409, L84

Maccarone T. J., Kundu A., Zepf S. E., Rhode K. L., 2011, , 410, 1655

Macri L. M., et al., 1999, , 521, 155

Middleton M. J., King A., 2017, , 470, L69

Middleton M. J., Walton D. J., Fabian A., Roberts T. P., Heil L., Pinto C., Anderson G., Sutton A., 2015, , 454, 3134

Miller-Jones J. C. A., et al., 2015, , 453, 3918

Mitsuda K., et al., 1984, , 36, 741

Morscher M., Umbreit S., Farr W. M., Rasio F. A., 2013, , 763, L15

Morscher M., Pattabiraman B., Rodriguez C., Rasio F. A., Umbreit S., 2015, , 800, 9

Osaki Y., 1995, , 47, L11

Pakull M. W., Mirioni L., 2002, arXiv e-prints, pp astro–ph/0202488

Paolillo M., Puzia T. H., Goudfrooij P., Zepf S. E., Maccarone T. J., Kundu A., Fabbiano G., Angelini L., 2011, , 736, 90

Park D., Kim C., Lee H. M., Bae Y.-B., Belczynski K., 2017, , 469, 4665

Peacock M. B., Maccarone T. J., Kundu A., Zepf S. E., 2010, , 407, 2611

Peacock M. B., Zepf S. E., Maccarone T. J., 2012a, , 752, 90

Peacock M. B., et al., 2012b, , 759, 126

Peacock M. B., Zepf S. E., Maccarone T. J., Kundu A., Gonzalez A. H., Lehmer B. D., Maraston C., 2014, , 784, 162

Pintore F., et al., 2018, , 477, L90

Plotkin R. M., Markoff S., Kelly B. C., Körding E., Anderson S. F., 2012, , 419, 267

Pooley D., et al., 2003, , 591, L131

Poutanen J., Lipunova G., Fabrika S., Butkevich A. G., Abolmasov P., 2007, , 377, 1187

Prada Moroni P. G., Straniero O., 2009, , 507, 1575

Rabolli M., 1990, , 244, 322

Ripamonti E., Mapelli M., 2012, , 423, 1144

Roberts T. P., et al., 2012, , 760, 135

Rodriguez C. L., Chatterjee S., Rasio F. A., 2016, , 93, 084029

Rodriguez C. L., Zevin M., Amaro-Seoane P., Chatterjee S., Kremer K., Rasio F. A., Ye C. S., 2019, , 100, 043027

Sarazin C. L., Kundu A., Irwin J. A., Sivakoff G. R., Blanton E. L., Randall S. W., 2003, , 595, 743

Scargle J. D., 1982, , 263, 835

Shakura N. I., Sunyaev R. A., 1973, , 500, 33

Shih I. C., Maccarone T. J., Kundu A., Zepf S. E., 2008, , 386, 2075

Shih I. C., Kundu A., Maccarone T. J., Zepf S. E., Joseph T. D., 2010, , 721, 323

Shishkovsky L., et al., 2018, , 855, 55

Sigurdsson S., Hernquist L., 1993, , 364, 423

Sippel A. C., Hurley J. R., 2013, , 430, L30

Sivakoff G. R., et al., 2007, , 660, 1246

Sivakoff G. R., Jordán A., Juett A. M., Sarazin C. L., Irwin J. A., 2008, preprint, p. arXiv:0806.0626 (`arXiv:0806.0626`)

Spitzer Jr. L., 1969, , 158, L139

Steele M. M., Zepf S. E., Kundu A., Maccarone T. J., Rhode K. L., Salzer J. J., 2011, , 739, 95

Steele M. M., Zepf S. E., Maccarone T. J., Kundu A., Rhode K. L., Salzer J. J., 2014, , 785, 147

Strader J., Chomiuk L., Maccarone T. J., Miller-Jones J. C. A., Seth A. C., 2012a, , 490, 71

Strader J., et al., 2012b, , 760, 87

Sutton A. D., Roberts T. P., Middleton M. J., 2013, , 435, 1758

Timmer J., Koenig M., 1995, , 300, 707

Titarchuk L., 1994, , 434, 570

Tody D., 1986, in Crawford D. L., ed., Vol. 627, Instrumentation in astronomy VI. p. 733, doi:10.1117/12.968154

Tody D., 1993, in Hanisch R. J., Brissenden R. J. V., Barnes J., eds, Vol. 52, Astronomical Data Analysis Software and Systems II. p. 173

Tudor V., et al., 2018, , 476, 1889

Urquhart R., Soria R., 2016, , 456, 1859

Van Der Walt S., Colbert S. C., Varoquaux G., 2011, preprint, (`arXiv:1102.1523`)

Van Haaften L. M., Nelemans G., Voss R., Wood M. A., Kuijpers J., 2012, , 537, A104

Walton D. J., et al., 2013, , 779, 148

Whitehurst R., 1988, , 232, 35

Wilms J., Allen A., McCray R., 2000, , 542, 914

Zepf S. E., Maccarone T. J., Bergond G., Kundu A., Rhode K. L., Salzer J. J., 2007, , 669, L69

Zepf S. E., et al., 2008, , 683, L139